UNIVERSITÉ CATHOLIQUE DE LOUVAIN
Ecole Polytechnique de Louvain
ICTEAM

Fabrication and characterization of rare-earth silicide thin films

Dissertation présentée en vue de l'obtention du grade de
Docteur en Sciences de l'Ingénieur
par

Nicolas Reckinger

Promoteurs:

Prof. Vincent Bayot
Prof. Jean-Pierre Raskin

Février 2011

UNIVERSITÉ CATHOLIQUE DE LOUVAIN
Ecole Polytechnique de Louvain
ICTEAM

Fabrication and characterization of rare-earth silicide thin films

Dissertation présentée en vue de l'obtention du grade de
Docteur en Sciences de l'Ingénieur
par

Nicolas Reckinger

Membres du jury:

Prof. Vincent Bayot, promoteur
Prof. Jean-Pierre Raskin, promoteur
Prof. Emmanuel Dubois
Prof. Denis Flandre
Dr. Thierry Baron
Prof. Siegfried Mantl
Dr. Xiaohui Tang
Prof. Danielle Vanhoenacker-Janvier, président

Février 2011

Abstract

With the continuous reduction of the dimensions of metal-oxide-semiconductor field-effect transistors (MOSFET), issues related to the formation of source and drain contacts by ion implantation appear. A new source and drain architecture based on metallic contacts over silicon was proposed to replace conventional highly doped extensions. To realize such a device, the so-called Schottky barrier (SB) MOSFET, requires working with materials presenting low Schottky barrier heights (SBH) to silicon. For n-type MOSFETs, rare-earth silicides, alloys between silicon and a rare-earth metal, are the best candidates. For Schottky barrier MOSFETs to compete with conventional ones in terms of on- and off-currents, the SBH of rare-earth silicides is intrinsically still too high and must accordingly be further reduced. Such a barrier decrease can be achieved with the dopant segregation technique, where a thin dopant layer is interposed between the silicide and silicon.

In the first two chapters of this thesis, we expose the theoretical aspects of metal-semiconductor (MS) contacts. Chapter 1 starts with a recall of the main steps of the long history of MS contacts. Next, the simplified energy band structure of metals and semiconductors is briefly described and applied to establish the energy band diagram of MS contacts. Then, the principal models of SBH formation are developed. Finally, ohmic contacts and the notion of specific contact resistance are tackled. The purpose of chapter 2 is to present the electrical extraction techniques of SBHs and the methods of material characterization that are used extensively in the two following chapters.

Chapter 3, devoted to the growth and the characterization of erbium (Er) silicide contacts on n-type silicon, is the central part of this work. Different techniques of metal deposition and thermal treatment are successively considered. Evaporation and growth in ultrahigh vacuum conditions leads to reference Er silicide thin films with excellent morphological and electrical characteristics. *Ex situ* growth with a protective titanium capping layer produces Er silicide with a state-of-the-art SBH of 0.28 eV at the optimal annealing temperature. It is also inferred

that the observed SBH drop with increasing annealing temperature can be associated to the progressive transformation of amorphous Er silicide into crystalline Er silicide. However, these films are plagued by superficial oxidation due to oxygen penetration through the titanium cap. By optimizing the process conditions (annealing atmosphere and cap thickness), oxygen-free Er silicide films can be fabricated. Finally, the last chapter of this text deals with the SBH modulation of Er silicide contacts on n-type silicon by dopant segregation. The extraction of an effective SBH of about 0.1 eV and the dopant redistribution in the silicide both testify to efficient segregation. The SBH reduction turns out to be all the more efficient that the dopant concentration at the interface is elevated. In the end, through quantum simulations, low temperature deviations of the current-voltage characteristics of silicide/silicon contacts are attributed to the nanoscale modulation of the SB profile by the applied voltage.

Remerciements

Tout le processus de la thèse (et de la vie en général d'ailleurs) consiste, au fur et à mesure du temps, à prendre confiance en soi et en ses capacités, sans pour autant tomber dans les pièges faciles de l'arrogance, de la suffisance et l'autosatisfaction, scléroses de l'esprit. Comme me le répète le paternel depuis ma plus tendre enfance: « Il ne faut jamais se reposer sur ses lauriers »! Avec un peu de recul, je me rends mieux compte combien on peut évoluer en l'espace de seulement quelques années (et encore heureux qu'il en soit ainsi!), tout en restant foncièrement la même personne. Ce processus progressif de construction et de découverte de soi ne peut se faire sans un environnement humain valorisant et formateur. Dans le cadre plus particulier de la recherche scientifique, on peut disposer du meilleur équipement du monde, sans le facteur humain, on ne peut aller bien loin! C'est pourquoi l'expression des remerciements revêt à mes yeux une importance toute spéciale. J'espère sincèrement n'oublier personne, je ne voudrais attirer sur moi les foudres de quiconque :-).

Tout d'abord, je tiens à exprimer ma reconnaissance à mes deux promoteurs, qui se sont successivement préoccupés de ma petite personne. En premier, Vincent, qui m'a permis de m'introduire au monde de la recherche à l'UCL et m'a encadré pendant mes premières années et qui, à sa façon, m'a appris à travailler de façon autonome et indépendante. Sa perspicacité et son sens critique aigu m'ont amenés à acquérir ou affûter le jugement que je porte sur mon propre travail. Ensuite Jean-Pierre, qui a repris le flambeau, pendant mes presque trois années de thèse. Je tiens vraiment à le remercier pour sa disponibilité presque permanente (combien de fois n'ai-je pas pu constater qu'il répondait à mes courriels à des heures indues, où la plupart des gens dorment ou en tous cas ne travaillent plus), son ouverture d'esprit, sa bonhomie, son optimisme, son enthousiasme communicatif parfois déconcertant ;-), son sens de l'empathie, j'en passe et des meilleures.

Ensuite, s'il y a bien quelqu'un qui mérite ma reconnaissance éternelle, c'est Xiaohui. Elle m'a tout d'abord encadré pendant mon mémoire

de fin d'études, avec Vincent, et m'a tout appris des arcanes des chambres propres. Au début, la communication « franglais-anglinoise » (« pimimi » et autres florilèges) n'a pas été des plus simple, mais après une période d'adaptation, nous avons vite fini par nous comprendre, ne dit-on pas que les grands esprits se rencontrent ;-). En outre, il a fallu un peu de temps pour installer la confiance du fait de cette réserve toute asiatique, mais une fois établie, elle est et demeure solide. L'apprentissage du chinois m'a également permis de mieux comprendre aussi bien la langue que la culture chinoises. Xiaohui a aussi parfois dû supporter mon impulsivité à l'énervement (qui l'eût cru!), genre soupe au lait, et mon penchant pour la taquinerie, j'espère ne pas l'avoir trop traumatisée :-).

Je ne peux pas non plus oublier mon deuxième collègue de bureau qui vient compléter la fine équipe, Alex, la grande brute[1] moldave, à la curiosité insatiable. Derrière ses dehors un peu bourrus et laconiques se cache en réalité un coeur en or (il ne va pas aimer lire cela mais c'est fait exprès :-)). Il a égayé l'ambiance du bureau de ses blagues et commentaires scatologiques, et autres borborygmes et météores. Plus sérieusement, sa persévérance et son intelligence pourraient servir d'exemple à plus d'un. Je dois aussi y associer Dana avec laquelle j'ai pu discuter de tout et de rien à de nombreuses reprises. Avec Xiaohui, elle a apporté une touche féminine indispensable dans ce monde très (trop) masculin de la recherche en sciences appliquées.

Au cours des projets européens auxquels j'ai pu participer, j'ai eu la chance d'entrer en contact et de travailler avec des collègues d'autres pays. Notamment, je voudrais remercier Emmanuel, Dmitri, Sylvie et Guilhem pour l'aide substantielle qu'ils m'ont apportée au cours de mes séjours à l'IEMN. Sans leur coopération, je peux vraiment affirmer que cette thèse n'aurait pas pu s'accomplir. Plus particulièrement Emmanuel, dont les commentaires toujours très avisés et constructifs et le perfectionnisme m'ont beaucoup aidé au cours de mon travail. Je pense aussi aux collègues polonais, Jacek et Adam, qui m'ont préparé de nombreux échantillons TEM.

Maintenant, parmi mes collègues proches à l'UCL, chacun avec ses particularités appréciables, je voudrais faire une mention spéciale à:

- Benoît H, qui sans peut-être s'en rendre compte, m'a gratifié à plusieurs reprises de conseils vraiment judicieux, et dont j'envie le calme et le sens de la diplomatie,
- Pierre-Olivier, le bricoleur inventif, dans lequel j'ai trouvé mon maître du point de vue de la distraction, et ce n'est pas peu dire, aussi cueilleur

[1] Prononcer brrrroute.

de champignons à ses heures,
- Augustin, tout en discrétion, efficacité et pragmatisme,
- Nicolas, qui comprend à merveille le second degré, grand amateur de blagues de m... et féru de digressions métaphysiques,
- Romain, avec qui j'ai apprécié les discussions ouvertes sur tout sujet imaginable,
- Sébastien F, au sens pratique inégalable, toujours prompt à la taquinerie envers Alex (qui, soit dit en passant, le mérite bien),
- Aryan et son imperturbable « zénitude »,

sans oublier mes autres collègues des défunts DICE et EMIC, Fred, Loïk, Cédric, Benoît O, Umesh, Vikram, Khairuddin, Khaled, Valeria, Cesar, Mohamed, Rémi, Luis, Gilles, Ester, Bertrand, David B, David L, Gaël, Arnaud, Catherine, Olivier, Joaquin, El Hafed, Guillaume, Geffroy, Sylvain etc. auxquels s'ajoutent aussi les professeurs du labo et d'ailleurs, Denis Flandre, Laurent Francis, Isabelle Huynen, Danielle Vanhoenacker, Michel Verleysen, Pascal Jacques et Sorin Melinte, qui ont aussi contribué de près ou de loin à l'achèvement de ma thèse.

Chose agréable avec les chambres propres, c'est qu'il est possible d'y rencontrer des personnes d'autres labos, avec lesquelles j'ai apprécié pouvoir discuter, notamment Marie-Stéphane (MS pour les intimes), Michaël, Laurianne, Zhijun, Hailu, Nasima etc. Je pense aussi à Claude, Sadia, Vlad, Jean-Michel et Joaquin, dont j'ai pu faire la connaissance dans d'autres circonstances. Je voudrais aussi mentionner les membres de l'équipe technique que j'ai eu l'occasion de côtoyer au cours de mes très nombreuses immersions en chambres propres: Mathieu, Bohdan, André, Christian, David, Nathanaël, Sébastien, Jonathan, Miloud, Manu, Pierrot et Jacques. Merci aussi à nos deux secrétaires, Anne et plus spécialement Viviane, dont j'ai beaucoup apprécié le dévouement et la gentillesse. J'y joins aussi notre gestionnaire informatique, Brigitte, et notre spécialiste en instrumentation, Pascal.

Je tiens également à remercier les membres du jury que je n'ai pas encore cités, à savoir Thierry Baron et Siegfried Mantl, d'avoir accepté de faire partie de mon jury et de m'avoir gratifié de commentaires positifs et constructifs pour l'amélioration du manuscrit de ma thèse et de l'interprétation de ses résultats.

J'adresse ma gratitude à mes amis de longue date et plus récents, Vincent, Yves, Guy, Patrice, Samuel, Biga et Olivier, pour leur soutien indéfectible depuis de nombreuses années.

Pour finir, mes plus profonds remerciements s'adressent à ma famille, les premiers à m'avoir encouragé. Papa, qui a depuis toujours attisé ma curiosité et développé mon sens critique, dont les principes et valeurs

inculqués notamment au moyen de nombreux proverbes français, latins, allemands, anglais, néerlandais etc. prennent à présent tout leur sens. J'ose espérer avoir quelque peu hérité de cette sagesse et de cette philosophie. Maman, toute en dévouement, compréhension et sensiblité. Ainsi que ceux qui ont le courage (et pas le choix non plus :-)) de me supporter depuis presque aussi longtemps héhé, mon frère Mathieu et ma soeur Céline, et Steve et leurs deux affreux marmots.

Contents

Symbols and abbreviations

$\boldsymbol{E_\delta}$	Electric field in the gap
$\boldsymbol{E}$	Electric field in the depletion region
C_D	Capacitance of the depletion zone
χ	Tilt angle
$\Delta V_\mathrm{SC/M}$	Potential drop in the gap between the semiconductor and the metal
δ	Gap width
$\Delta\Phi$	Image-force lowering
δ_GS	Decay length of the MIGS
δ_int	Thickness of the interfacial dielectric layer
ΔV_int	Potential drop through the dielectric layer
D_GS	Density of surface states
E_B	Electron binding energy
E_BB	Total band bending energy at the MS interface
E_C	Conduction band minimum
E_F	Fermi level
E_FM	Metal Fermi level
E_FSC	Semiconductor Fermi level
E_g	Energy bandgap
E_K	Electron kinetic energy
ϵ_GS	Permittivity of the interfacial semiconductor layer where MIGS penetrate
ϵ_int	Dielectric permittivity of the interfacial layer
ϵ_SC	Dielectric permittivity of the semiconductor
ϵ_0	Vacuum permittivity
η	Ideality factor
E_V	Valence band maximum
$\mathrm{E_{vac}}$	Vacuum level
$\mathrm{E_{vacM}}$	Metal vacuum level
$\mathrm{E_{vacSC}}$	Semiconductor vacuum level
I_F	Forward current
I_R	Reverse current

J_{F}	Forward current density
J_{m}	Flatband current density
J_{R}	Reverse current density
κ	Energy parameter for hopping interactions
λ	Light wavelength
L_{DS}	Length of the segregated region in Si
L_{Si}	Si gap length
L_{T}	Transfer length
N_{D}	Donor concentration
N_{D}^{+}	Concentration in ionized donor impurities
N_{DS}	Doping concentration of the segregated region in Si
ν	Light frequency
ω	Angle of incidence
Φ	Work function
$\phi(x)$	Potential
$\Phi_{\mathrm{B}}^{\mathrm{eff}}$	Effective SBH
Q_{GS}	Gap states charge density
Q_{M}	Charge density on the metal
Q_{SC}	Charge density in the depletion region
R_{C}	Contact resistance
ρ	Volumetric charge density
ρ_{c}	Specific contact resistance
R_{S}	Sheet resistance
R_{Sch}	Equivalent Schottky resistance
R_{Si}	Si series resistance
τ	Transmission probability
θ	Angle of incidence
V_{A}	Applied voltage
φ	Spin angle
V_{BI}	Built-in voltage
$\vec{p}$	Electron momentum
V_{F}	Forward bias
V_{R}	Reverse bias
A	Contact surface
a	Superlinear semiconductor resistance coefficient
A^{*}	Effective Richardson constant
C-V	Capacitance-voltage
d	Distance between two atomic planes
$d(E)$	Energy-dependent barrier width
d_{MS}	Distance between the interfacial planes
E_{Cbulk}	Value of the conduction band maximum in the semiconductor bulk

E_{I}	Implantation energy
$f_{\mathrm{FD}}(E,T)$	Fermi-dirac distribution
f_{M}	Occupation probability in the metal
f_{SC}	Occupation probability in the semiconductor
h	Planck constant
I-V	Current-voltage
$I_{m\rightarrow s}$	Current from the metal to the semiconductor
$I_{s\rightarrow m}$	Current from the semiconductor to the metal
$J(E)$	Current spectrum
k	Boltzmann constant
L	Contact length
m^*	Effective mass in the semiconductor
N	Doping concentration
n	Electron density in the conduction band
N_{B}	Density of chemical bonds at the MS interface
p	Hole density in the valence band
PE	Total potential energy of the electron
q	Electronic charge
$q\chi$	Semiconductor electron affinity
$q\Phi_{\mathrm{B}n}$	Schottky barrier height to electrons
$q\Phi_{\mathrm{B}p}$	Schottky barrier height to holes
$q\Phi_{\mathrm{CNL}}$	CNL position relatively to the valence band maximum
$q\Phi_{\mathrm{M}}$	Metal work fonction
$q\Phi_{\mathrm{SC}}$	Semiconductor work fonction
qV_{N}	Difference between E_{C} and E_{F}
T	Absolute temperature
t_{Er}	Er thickness
t_{Ti}	Ti thickness
$V_{2\mathrm{C}}$	Four-contact voltage drop
$V_{4\mathrm{C}}$	Two-contact voltage drop
W	Contact width
w	Depletion width
R_{SC}	Semiconductor series resistance
H_2SO_4	Sulfuric acid
NH_4OH	Ammonium hydroxide
ErO_x	Er suboxide
Er_2O_3	Er sesquioxide
$ErSi_{2\text{-}x}$	Er disilicide
H_2O_2	Hydrogen peroxide
SiO_2	Si dioxide
a-Er/Si	Amorphous Er silicide

a-Si	Amorphous Si
BCC	Body-centered cubic
BE	Binding energy
BHF	Buffer hydrofluoric acid
BL	Barrier lowering
CMOS	Complementary metal-oxide-semiconductor
CNL	Charge neutrality level
DI	De-ionized
DS	Dopant segregation
EDS	Energy-dispersive x-ray spectrometry
EELS	Electron energy-loss spectrometry
FE	Field emission
HF	Hydrofluoric acid
HRTEM	High-resolution transmission electron microscopy
HSQ	Hydrogen silsesquioxane
HV	High vacuum
IBS	Implant before silicidation
ITM	Implant to metal
ITS	Implant to silicide
MIGS	Metal-induced gap states
MOSFET	Metal-oxide-semiconductor field-effect transistor
MS	Metal-semiconductor
NEGF	Non-equilibrium Green's function
RE	Rare-earth
RTA	Rapid thermal annealing
S/D	Source/drain
SADS	Silicide as diffusion source
SB	Schottky barrier
SBH	Schottky barrier height
SBMOSFET	Schottky barrier metal-oxide-semiconductor field-effect transistor
SEM	Scanning electron microscopy
SIDS	Silicidation-induced dopant segregation
SIMS	Secondary ion mass spectroscopy
SOI	Silicon-on-insulator
SPM	Sulfuric peroxide mixture
ST	Sputter time
TE	Thermionic emission
TEM	Transmission electron microscopy
TFE	Thermionic-field emission
TiN_x	Ti nitride
TiO_2	Ti dioxide

UHV	Ultrahigh vacuum
VM	Valence-mending
XPS	X-ray photoelectron spectroscopy
XRD	X-ray diffraction
XTEM	Cross-sectional transmission electron microscopy

List of Figures

List of Tables

List of Publications

Journals

N. Reckinger, X. Tang, E. Dubois, D. Flandre, J.-P. Raskin, and A. Afzalian, *Low temperature tunneling current enhancement in silicide/Si Schottky contacts with nanoscale barrier width*, submitted to Appl. Phys. Lett., under review.

J. Ratajczak, A. Łaszcz, A. Czerwiński, J. Kątcki, F. Phillipp, P. A. van Aken, **N. Reckinger**, and E. Dubois, *Transmission electron microscopy study of erbium silicide formation from Ti/Er stack for Schottky contact applications*, J. Microsc. 237, 379 (2010).

A. Łaszcz, J. Ratajczak, A. Czerwiński, J. Kątcki, V. Srot, F. Phillipp, P. A. van Aken, D. Yarekha, **N. Reckinger**, G. Larrieu, and E. Dubois, *Characterization of ytterbium silicide formed in ultra high vacuum*, J. Phys.: Conf. Ser. 209, 012056 (2010).

J. Ratajczak, A. Łaszcz, A. Czerwiński, J. Kątcki, X. Tang, **N. Reckinger**, D. A. Yarekha, G. Larrieu, and E. Dubois, *TEM characterization of polysilicon and silicide fin fabrication processes of finFETs*, Acta Phys. Pol. A 116, S89 (2009).

D. A. Yarekha, G. Larrieu, N. Breil, E. Dubois, S. Godey, X. Wallart, C. Soyer, D. Remiens, **N. Reckinger**, X. Tang, A. Łaszcz, J. Ratajczak, and A. Halimaoui, *UHV fabrication of the ytterbium silicide as potential low Schottky barrier S/D contact material for n-type MOSFET*, ECS Trans. 19, 339 (2009).

G. Larrieu, D. Yarekha, E. Dubois, N. Breil, **N. Reckinger**, X. Tang, and A. Halimaoui, *Issues associated to rare earth silicide integration in ultra thin FD SOI Schottky barrier nMOSFETs*, ECS Trans. 19, 201 (2009).

C. Krzeminski, X. Tang, **N. Reckinger**, V. Bayot, and E. Dubois, *Process optimization and downscaling of an alternative single dot flash memory*, IEEE Trans. on Nanotechnol. 8, 737 (2009).

X. Tang, V. Bayot, **N. Reckinger**, D. Flandre, J.-P. Raskin, E. Dubois, and B. Nysten, *A simple method for measuring Si-fin sidewall roughness by AFM*, IEEE Trans. on Nanotechnol. 8, 611 (2009).

X. Tang, **N. Reckinger**, V. Bayot, D. Flandre, E. Dubois, D. A. Yarekha, G. Larrieu, A. Lecestre, J. Ratajczak, N. Breil, V. Passi, and J.-P. Raskin, *An electrical evaluation method for the silicidation of silicon nanowires*, Appl. Phys. Lett. 95, 023106 (2009).

N. Reckinger, X. Tang, V. Bayot, D. A. Yarekha, E. Dubois, S. Godey, X. Wallart, G. Larrieu, A. Łaszcz, J. Ratajczak, P. J. Jacques, and J.-P. Raskin, *Schottky barrier lowering with the formation of crystalline Er silicide on n-Si upon thermal annealing*, Appl. Phys. Lett. 94, 191913 (2009).

G. Larrieu, E. Dubois, D. Yarekha, N. Breil, **N. Reckinger**, X. Tang, J. Ratajczak, and A. Łaszcz, *Impact of channel doping on Schottky barrier height and investigation on p-SB MOSFETs performance*, Mater. Sci. Eng. B 154, 159 (2008).

N. Reckinger, X. Tang, V. Bayot, D. A. Yarekha, E. Dubois, S. Godey, X. Wallart, G. Larrieu, A. Łaszcz, J. Ratajczak, P. J. Jacques, and J.-P. Raskin, *Low Schottky barrier height for ersi/n-Si contacts formed with a Ti cap*, J. Appl. Phys. 104, 103522 (2008).

X. Tang, **N. Reckinger**, G. Larrieu, E. Dubois, D. Flandre, J.-P. Raskin, B. Nysten, A. M. Jonas, and V. Bayot, *Characterization of ultrathin SOI film and application to short channel MOSFETs*, Nanotechnol. 19, 165703 (2008).

A. Vlad, M. Mátéfi-Tempfli, V. Antohe, S. Faniel, **N. Reckinger**, B. Olbrechts, A. Crahay, V. Bayot, L. Piraux, S. Melinte, and S. Mátéfi-Tempfli, *Nanowire-decorated microscale metallic electrodes*, Small 4, 557 (2008).

E. Pascual, R. Rengel, **N. Reckinger**, X. Tang, V. Bayot, E. Dubois, and M. J. Martin, *A Monte Carlo investigation of carrier transport in*

fabricated back-to-back Schottky diodes: influence of direct quantum tunnelling and temperature, Phys. Status Solidi C 5, 119 (2008).

X. Tang, **N. Reckinger**, V. Bayot, C. Krzeminski, E. Dubois, A. Villaret, and D. C. Bensahel, *Room-temperature single-electron operation and fabrication reproducibility of self-aligned single-dot memory devices*, IEEE Trans. on Nanotechnol. 5, 649 (2006).

C. Krzeminski, E. Dubois, X. Tang, **N. Reckinger**, A. Crahay, and V. Bayot, *Optimisation and simulation of an alternative nano-flash memory: The SASEM device*, Mater. Res. Soc. Symp. Proc. 830, 45 (2005).

X. Tang, J. Kątcki, E. Dubois, **N. Reckinger**, J. Ratajczak, G. Larrieu, P. Loumaye, O. Nisole, and V. Bayot, *Very low Schottky barrier to n-type silicon with PtEr-stack silicide*, Solid-State Electron. 47, 2105 (2003).

X. Tang, X. Baie, J.-P. Colinge, A. Crahay, B. Katschmarskyj, V. Scheuren, D. Spôte, **N. Reckinger**, F. Van de Wiele, and V. Bayot, *Self-aligned silicon-on-insulator nano flash memory device*, Solid-State Electron. 44, 2259 (2000).

International conferences

J. Ratajczak, A. Łaszcz, A. Czerwiński, J. Kątcki, F. Phillipp, P. A. van Aken, **N. Reckinger**, and E. Dubois, *Transmission electron microscopy study of erbium silicide formation from Ti/Er stack for Schottky contact applications*, 13th Conference on Electron Microscopy of Solids, Zakopane, Poland, 2009.

A. Łaszcz, J. Ratajczak, A. Czerwiński, J. Kątcki, V. Srot, F. Phillipp, P. A. van Aken, D. Yarekha, **N. Reckinger**, G. Larrieu, and E Dubois, *Characterization of ytterbium silicide formed in ultra high vacuum*, 16th Conference on Microscopy of Semiconducting Material, Oxford, UK, 2009.

J. Ratajczak, A. Łaszcz, A. Czerwiński, J. Kątcki, X. Tang, **N. Reckinger**, D. A. Yarekha, G. Larrieu, and E. Dubois, *TEM Characterization of polysilicon and silicide fin fabrication processes of FinFETs*, 3rd National Conference on Nanotechnology, Warsaw, Poland, 2009.

A. Łaszcz, J. Ratajczak, A. Czerwiński, J. Kątcki, F. Phillipp, P. A.

van Aken, D. Yarekha, **N. Reckinger**, G. Larrieu, and E. Dubois, *HRTEM characterization of erbium silicide formed in ultra high vacuum*, Microscopy Conference 2009, Graz, Austria, 2009.

D. A. Yarekha, G. Larrieu, N. Breil, E. Dubois, S. Godey, X. Wallart, C. Soyer, D. Remiens, **N. Reckinger**, X. Tang, A. Łaszcz, J. Ratajczak, and A. Halimaoui, *UHV fabrication of the ytterbium silicide as potential low Schottky barrier S/D contact material for n-type MOSFET*, 215th Electrochemical Society Meeting , San Francisco, CA, USA, 2009.

G. Larrieu, D. Yarekha, E. Dubois, N. Breil, **N. Reckinger**, X. Tang, and A. Halimaoui, *Issues associated to rare earth silicide integration in ultra thin FD SOI Schottky barrier nMOSFETs*, 215th Electrochemical Society Meeting , San Francisco, CA, USA, 2009.

J. Kątcki, J. Ratajczak, A. Łaszcz, A. Czerwiński, **N. Reckinger**, X. Tang, G. Larrieu, N. Breil, D. Yarekha, E. Dubois, *Analysis of silicides formation for Schottky barrier contacts applications*, 7th Polish-Japanese Joint Seminar on Micro and Nano Analysis, Warsaw, Poland, 2008.

G. Larrieu, E. Dubois, D. Yarekha, N. Breil, **N. Reckinger**, X. Tang, J. Ratajczak, and A. Łaszcz, *Impact of channel doping on Schottky barrier height and investigation on p-SBMOSFETs performance*, Spring Meeting of the European Materials Research Society, Strasbourg, France, 2008.

E. Pascual, R. Rengel, **N. Reckinge**r, X. Tang, V. Bayot, E. Dubois, and M. J. Martín, *A Monte Carlo investigation of carrier transport in fabricated back-to-back Schottky diodes: influence of direct quantum tunnelling and temperature*, 15th International Conference on Nonequilibrium Carrier Dynamics in Semiconductors, Tokyo, Japan, 2007.

N. Breil, E. Dubois, **N. Reckinger**, X. Tang, G. Larrieu, A. Pouydebasque, A. Halimaoui, and T. Skotnicki, *Erbium silicide formation under ultra high vacuum*, 16th Conference on Materials for Advanced Metallization, Bruges, Belgium, 2007.

J. Knoch, E. Dubois, G. Larrieu, N. Breil, X. Tang, **N. Reckinger**, and V. Bayot, *Recent advances in metallic source-drain engineering*, SINANO-ESSDERC Workshop, Grenoble, France, 2005.

Xiaohui Tang, **N. Reckinger**, V. Bayot, E. Dubois, C. Krzeminski, *Self-aligned single-electron memories: towards single-electron operation of*

MOS compatible nano-flash memory devices, SINANO-ESSDERC Workshop, Grenoble, France, 2005.

X. Tang, **N. Reckinger**, V. Bayot, E. Dubois, C. Krzeminski, A. Villaret, and D. Bensahel, *Self-aligned single-electron memories*, 15th NID Workshop, Madrid, Spain, 2005.

C. Krzeminski, E. Dubois, X. Tang, **N. Reckinger**, A. Crahay, and V. Bayot, *Optimisation and simulation of an alternative nano-flash memory: the SASEM device*, MRS Fall meeting, Boston MA, USA, 2004.

E. Dubois, G. Larrieu, C. Krzeminski, X. Baie, Xiaohui Tang, **N. Reckinger**, V. Bayot, E. Robilliart, B. Froment, and J. Kątcki, *Integration of low Schottky barrier source/drain for advanced MOS technology*, 13th NID Workshop, Athens, Greece, 2004.

X. Tang, **N. Reckinger**, and V. Bayot, *SOI nano device fabrication*, NATO Advanced Research Workshop on Science and Technology of Semiconductor-On-Insulator Structures and Devices Operating in a Harsh Environment, Kiev, Ukraine, 2004.

Books

X. Tang, **N. Reckinger**, and V. Bayot, *Fabrication of SOI nano devices*, in *Science and Technology of Semiconductor-on-Insulator Structures and Devices Operating in a Harsh Environment*, edited by D. Flandre, A. N. Nazarov, and P. L. F. Hemment (Kluwer, Dordrecht, 2005), p. 333.

A. N. Nazarov, V. S. Lysenko, X. Tang, **N. Reckinger**, and V. Bayot, *Charge trapping phenomena in single electron NVM SOI devices fabricated by a self-aligned quantum dot technology*, in *Nanoscaled semiconductor-on-insulator structures and devices*, edited by S. Hall, A. N. Nazarov, and V. S. Lysenko (Springer, Berlin, 2007), p. 251.

Introduction

Metal-semiconductor (MS) interfaces play a fundamental role in solid-state electronics and optoelectronics because they are intensively used as a link between the solid-state device and the outside world. An ideal MS interface should not alter the current flow through the device. More precisely, this means that an ideal MS contact should be characterized by a linear relationship between the current and the resulting voltage drop i.e. obey to Ohm's law. For obvious reasons, such a contact is called an "ohmic contact".

One of the most important properties of MS interfaces is their "Schottky barrier height" (SBH), which characterizes the energy mismatch between majority carriers on each side of the interface. The SBH regulates the electronic transport across MS interfaces. If the SBH is too high, the MS contact presents asymmetric current-voltage characteristics which considerably differ from Ohm's law. These contacts belong to the category of "rectifying" or "Schottky contacts", named so in honor of Walter Schottky who was the first to explain their physical behavior. Unfortunately, most of MS contacts are of Schottky-type. In consequence, producing ohmic contacts is a permanent challenge in semiconductor technology, what is in turn a good thing since it provides a lot of work to engineers and scientists (and by the way, a subject to this thesis)!

The issue is particularly blatant in the integrated circuit technology with the continuous dimension downscaling of metal-oxide-semiconductor field-effect transistors (MOSFETs). Ohmic contacts to MOSFETs are conventionally realized by metallic contacts over heavily doped Si source/drain (S/D) implants. Usually, the metallic contacts are created by alloying highly doped Si S/D to a given metal (Ti, Co, Ni, etc.), creating a new compound called a "silicide" (see Fig. 1(a)). Silicides are preferred over pure metals because of their greater thermal and chemical stability.

But the more the dimensions of MOSFETs are reduced toward the 10 nm node, the more the constraints on the classical implanted S/D tighten [1], due to increasing process difficulties essentially related to dopant activation to achieve (i) heavily doped junctions (for low sheet

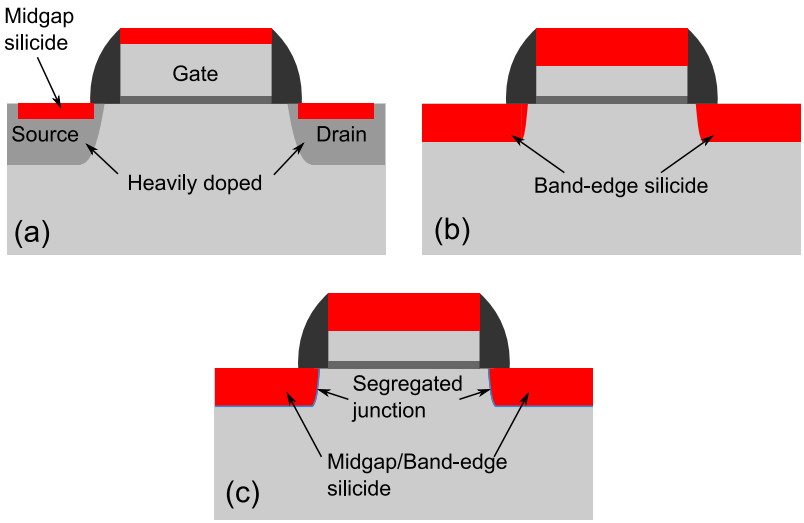

Figure 1: Different S/D architectures for MOSFETs: (a) conventional architecture with heavily doped S/D regions contacted with a midgap silicide, (b) SBMOSFET with band-edge silicide S/D, and (c) DS-SBMOSFET with either bangap or midgap silicide and dopant pile-up at the MS interface.

resistance), (ii) extremely steep lateral profiling, and (iii) low specific contact resistance. In order to overcome these problems, it was proposed to replace the strongly doped S/D by metallic Schottky S/D [2] in the so-called Schottky barrier (SB) MOSFET architecture (see Fig. 1(b)). Compared with heavily doped diffusion, metallic S/D possess the advantage of a low resistivity and, in the case of silicide, can form atomically abrupt junctions with Si. The main challenge associated to this architecture is to reach a very low specific contact resistance. This objective can in principle be achieved working with very low SBHs.

A first approach to the SBMOSFET concept is based on band-edge silicides[2] which present low SBHs[3] either to holes (like platinum silicide) or to electrons (silicides from the rare-earth (RE) family like erbium (Er), ytterbium (Yb), etc.). Metallic Schottky S/D based on platinum [3–7] or RE [3, 8–12] silicides were successfully used for the realization of p- and n-MOSFETS, respectively. However, the performance of both p- and n-SBMOSFETs are too limited to compete with conventional MOSFETs

[2]As opposed to midgap silicides like $TiSi_2$, $CoSi_2$ or NiSi successively used in conventional technology.

[3]Arbitrarily defined here as SBHs less than 0.3 eV.

because of the still too high SBHs to holes (0.15 eV) and electrons (0.28 eV) on low doping Si.

From modeling considerations, it was recently stated that the SBH should ideally be at most 0.1 eV [13, 14]. However, even though a large spectrum of metals that could lead to very low barriers to Si is available, it is very difficult in practice to modulate the SBH below 0.1 eV due to the intrinsic physico-chemical properties of MS interfaces. Since that objective cannot be reached with "simple" MS contacts, some new "tricks" must inevitably be used to get around the problem.

Techniques based on the passivation of the Si surface to facilitate SBH tuning were proposed and successively implemented in simili-SBMOSFET structures with pure metals [15, 16] but their application to self-aligned MOSFETs is not an easy task.

Another approach that is more compatible with self-aligned processes consists in introducing a high concentration of dopants in a very thin layer at the silicide/Si interface in a SBMOSFET [17] (see Fig. 1(c)). The so-called "dopant segregation" (DS) involves dopant implantation followed by a dopant pile-up at the silicide/Si after thermal budget. The dopant-segregated layer causes a drastic reduction of the effective SBH. It could be argued that this concept is paradoxical since issues related to the formation of ultra-shallow junctions were at the source of the interest in the SBMOSFET architecture. In conventional processes, efficient dopant activation requires annealing at high temperatures that provokes lateral impurity diffusion. Still, lateral diffusion can be limited with the DS scenario because it allows to achieve dopant activation at significantly lower temperatures. DS-SBMOSFETs can be realized either with midgap[4] (mostly NiSi [18–22]) or band-edge silicides [23–26], each flavor presenting its own interest. The ideal case would be to use two different low SBH silicides for complementary MOS (CMOS) technology, but at the expense of process cost and simplicity. Midgap silicides are convenient since a single silicide can be used for both n- and p-type MOSFETs, with the appropriate doping species [22]. But, compared with band-edge silicides, their relatively high SBHs limit the current drive. A third intermediate solution is to make use of a single band-edge silicide combined with the adequate dopant for each MOSFET type.

As already unveiled by its title, the objective of this thesis is to study the formation of RE silicides. Since a comprehensive study of the RE family is not possible, we have limited our investigation to Er silicide which is probably the most documented amongst the RE silicides. The

[4]Contrary to non-segregated SBMOSFET, thanks to the possible use of either donor or acceptor impurities.

present manuscript is divided into four chapters. In the first introductive chapter, the theoretical aspects of MS contacts are treated. The second chapter is dedicated to the description of the characterization techniques abundantly used in this work, both electrical and physical. The next two chapters constitute the main contributions of this thesis to the scientific knowledge. More specifically, chapter 3 deals with the formation of Er silicide under various process conditions, while chapter 4 exposes the implementation of DS to Er silicide based on the results of chapter 3. Finally, this text ends with a summary of the principal achievements and some perspectives for future work are given.

Chapter 1

Metal-semiconductor contacts

In this theory-oriented chapter, we present the important concepts thoroughly used in the abundant literature about MS contacts. First, we give an historical context regarding the evolution of the understanding of the underlying physical mechanims of MS contact formation. Then, we introduce some basic concepts that will lead to a classification of MS contacts in two types: Schottky and ohmic contacts. The third section progressively exposes the main models developed to unveil the formation mechanism of Schottky contacts. Finally, the last section of the chapter deals with ohmic contacts.

1.1 Historical milestones

The purpose of this introductive section is to provide the reader with a brief summary of the already long history of MS contacts. The author believes that before entering into details, it is important to give a context where the major advances in the field of MS interfaces can be placed in.

In 1874, Ferdinand Braun [27] first discovered that current flows freely in only one direction at the contact between a metal point and a galena crystal (which is a semiconductor). The discovery earned him the 1909 Nobel Prize in physics together with Guglielmo Marconi. That specific regulation of the electronic current is called "rectifier effect" or "rectification". The phenomenon was explained only thirty years later, in 1939, jointly by Walter Schottky [28] and Sir Nevill Mott [29]. In his paper entitled *Zur Halbleitertheorie der Sperrschicht- und Spitzengleichrichter*[1] [28], Schottky explained that the rectifying behavior of MS contacts is due to an energy mismatch between the metal and the semiconductor. The resulting energy barrier between the metal and the

[1] Semiconductor theory of the blocking layer and of the peak rectifier.

semiconductor is so high that the region of the semiconductor right at the MS interface is depleted of majority carriers at thermodynamic equilibrium. In consequence, the fixed dopant atoms in that region are ionized and form an insulating space charge zone that causes current rectification.

Mott in 1938 [30] and Schottky in 1940 [31] were the first to propose a simple rule to determine the energy barrier height. The so-called Schottky-Mott theory predicts that the energy barrier $q\Phi_{\mathrm{B}n}$ (the SBH in fact) between a semiconductor (considered n-type here) with an electron affinity $q\chi$ and a metal with a work fonction $q\Phi_{\mathrm{M}}$ should be given by:

$$q\Phi_{\mathrm{B}n} = q\Phi_{\mathrm{M}} - q\chi, \tag{1.1}$$

with q the electronic charge. This expression is the "Schottky-Mott relationship".

But the experimental results were not compatible with the strong dependence of the SBH on Φ_{M} ($\partial\Phi_{\mathrm{B}n}/\partial\Phi_{\mathrm{M}} = 1$). This insensitivity of the experimental SBH to the metal work function (i.e. $\partial\Phi_{\mathrm{B}n}/\partial\Phi_{\mathrm{M}} \ll 1$) is called "Fermi level pinning". All the scientific work that was performed after the pioneer work of Schottky and Mott to reconciliate experiment and theory consisted in fact in finding a physical explanation underlying the Fermi level pinning phenomenon.

Some years later (in 1947), to explain Fermi level pinning, Bardeen introduced the concept of "interface states"[2] that might absorb charge [32]. The resulting charge density on the metal side of the contact is then balanced by an identical charge density of opposite sign on the semiconductor side, which is shared between the space charge zone and the interface states.

In 1965, Cowley and Sze [33] quantified the concept of interface states, deriving the dependence of the SBH on the interface states and on the metal work function (the so-called "fixed separation model" for surface states). These states are an intrinsic property of the semiconductor only and no assumption was made regarding their physical nature.

At the same time, Heine [34] gave a physical origin to the surface states: they are induced by the penetration of the metallic wave functions into the semiconductor. Louie and Cohen [35] clearly confirmed the existence of these states and called them "metal-induced gap states" (MIGS).

Tejedor *et al.* [36] introduced the concept of "neutral point" or "charge neutrality level" (CNL) for MS interfaces. The CNL controls how the charge is transferred between the semiconductor and any other crystal

[2] Also equivalently designated as "surface states" or "gap states".

deposited on it. The Fermi level position relatively to the CNL of the MIGS determines their donor- or acceptor-like character. Moreover, the CNL causes strong pinning of the interface Fermi level. In 1984, Tersoff [37] proved the generality and simplicity of the Fermi level pinning close to the CNL. The previous models always assumed the MIGS properties to be intrinsic to the semiconductor.

With quite a different point of view, another interesting attempt to shed light on the physical mechanism underlying the SB formation was proposed by Spicer *et al.* in 1979 in their "unified defect model" [38], where the SBH is determined by discrete "defect-induced" gap states[3]. Instead of discrete defect levels, Hasegawa and Ohno [39] proposed in 1986 a continuum of defect levels in the band gap to explain the Fermi level pinning.

It was only in 1999, after a progressive conceptual enhancement, that Mönch verified Heine's idea of MIGS by a host of experimental data [40]. Shortly after that, in 2000, Tung [41] made the last major theoretical breakthrough regarding the physical understanding of the SB mechanism formation. His "bond-polarization" theory is based on the intuitive idea that the Fermi level pinning must be somehow related to the chemistry and the structure of the MS interface. Contrary to the MIGS model which considers the interface states as a characteristic of the semiconductor only, the bond-polarization model rests on the fact that the SB depends both on the semiconductor and metal properties. With that picture of chemical bonding, the author gave a successful prediction of the mechanism of SB formation, in good agreement with experimental data [41].

Table 1.1 gives the list of the main concepts of MS contacts theory tackled in the present historical summary, in association with the corresponding year and author name(s).

1.2 Basic concepts

Before jumping to more theoretical developments, it is good to remind the reader of some important concepts founding the theory of MS contacts. The following presentation is based on several reference books [42–47].

[3] Also called "disorder-induced" gap states.

Author(s)	Major advances
Schottky (1938) Mott (1940)	$q\Phi_{Bn} = q\Phi_M - q\chi$
Bardeen (1947)	Surface states
Cowley and Sze (1965)	Fixed separation model for surface states
Heine (1965)	Metal-induced gap states
Tejedor *et al.* (1977)	Charge neutrality level for MS interfaces
Spicer *et al.* (1979)	Defect-induced gap states
Tung (2000)	Bond polarization

Table 1.1: Main concepts in the field of MS contacts.

1.2.1 Simplified energy band structure of metals and semiconductors

In this section, we make the choice to present a simplified and intuitive approach for the energy band structure of metals and semiconductors, sufficient to tackle the energy band diagram of MS contacts, as usually proposed in common books on semiconductor device physics. For more rigorous and complete quantum treatment, we invite the reader to refer to adequate reference books like [48].

Once the band structure of a given material is known, we still need to find out which energy levels are occupied. The electrical characteristics of the considered material are determined by the degree of occupancy of specific energy bands. The energy bands can be empty, partially filled or completely filled.

Empty bands are not expected to contribute to the electrical conductivity of the material since they do not contain electrons. Partially filled bands do contain electrons as well as unoccupied energy levels at slightly higher energies. These available states enable carriers to gain energy when moving in an applied electric field. Electrons in a partially filled band therefore do contribute to the electrical conductivity of the material. Completely filled bands contain a lot of electrons but do not contribute to the conductivity of the material. This is because the electrons cannot gain energy (at least a "reasonably small" amount) since all energy levels are already filled. Only the electrons located in the highest energy bands, the "valence band" and the "conduction band", can participate to conduction. On the other side, the other electrons from the inner shells (the core electrons) are too tightly bound to the atom to

escape. In solids, the valence band is the highest range of electron energies where electrons are normally present at absolute zero temperature. The conduction band is the range of electron energies, higher than that of the valence band, sufficient to free an electron from binding with its individual atom and allow it to move freely within the atomic lattice of the material. At 0 K, the highest occupied energy level for an electron is the "Fermi level". The fundamental difference between a metal and a semiconductor resides in the characteristics of their valence and conduction bands, respectively.

The two possible scenarios for a metal (metal 1 and metal 2) are presented in Figs. 1.1(a) and 1.1(b). In the first case (all elements with an odd number of electrons), the valence band is only partially filled with electrons at 0 K. In fact, the valence and conduction band for metal 1 are the same. For the second case (pair number of electrons), the valence band is completely filled at 0 K and partially overlaps the conduction band. The common point between the two scenarios is that the electron virtually needs no extra energy to get free from its atom and to move in the crystal.

In a semiconductor, at 0 K, the valence band is completely filled and the conduction band empty (pair number of electrons), but contrary to metal 2, they do not overlap and are separated by an energy bandgap E_{g} (see Fig. 1.1(c)). For higher temperatures, some electrons have enough thermal energy to be transferred to the conduction band and circulate in the crystal. To be promoted into the conduction band, the electrons in the valence band have to "jump over" the energy bandgap. This means that an electron must be supplied with a significant amount of energy (at least E_{g}) to leave the atom to which it is bound and to be able to move freely in the crystal. Finally, the difference between a semiconductor and an insulator is arbitrary and essentially depends on the magnitude of E_{g} (see Fig. 1.1(d)).

After making the distinction between a metal and a semiconductor, we can now give a more detailed description of their band structure. Figures 1.2(a) and 1.2(b) show the energy band diagrams of a metal and a semiconductor, respectively. The vacuum level represents an energy state in which an electron is at rest (with a null kinetic energy) and far away from the influence of the potential of the solid (at an "infinite" distance). It is symbolized by $\mathrm{E_{vacSC}}$ and $\mathrm{E_{vacM}}$ for the semiconductor and the metal, respectively. To characterize the metal, we only need to know the position of its Fermi level E_{FM} relatively to the vacuum level. The semiconductor can be described by its valence band maximum E_{V} and its conduction band minimum E_{C}, with the Fermi level E_{FSC} somewhere in between, in the bandgap (for a non degenerate semiconductor). With

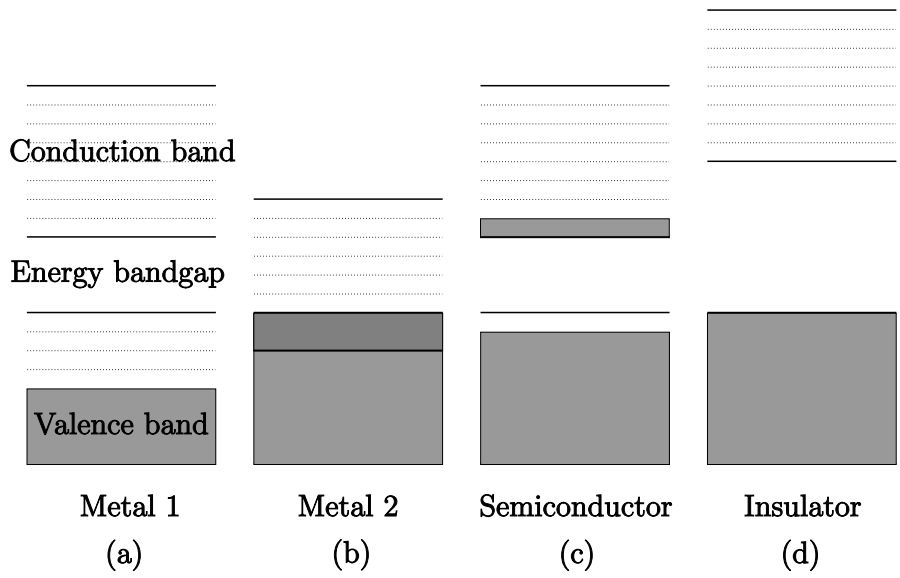

Figure 1.1: Four possible scenarios for the simplified energy band diagram of a crystal: (a) metal 1: valence band partially filled with electrons, (b) metal 2: valence band completely filled with electrons and overlap with the conduction band, (c) semiconductor: valence band completely filled with electrons without overlapping the conduction band, and (d) insulator: same as (c) with a larger bandgap.

these definitions, we see that $q\Phi_{\mathrm{M}}$, $q\Phi_{\mathrm{SC}}$ and $q\chi$ are the energies required to extract one electron with an energy E_{FM} from the metal, one electron with an energy E_{FSC} from the semiconductor, and one electron with an energy E_{C} to the vacuum, respectively.

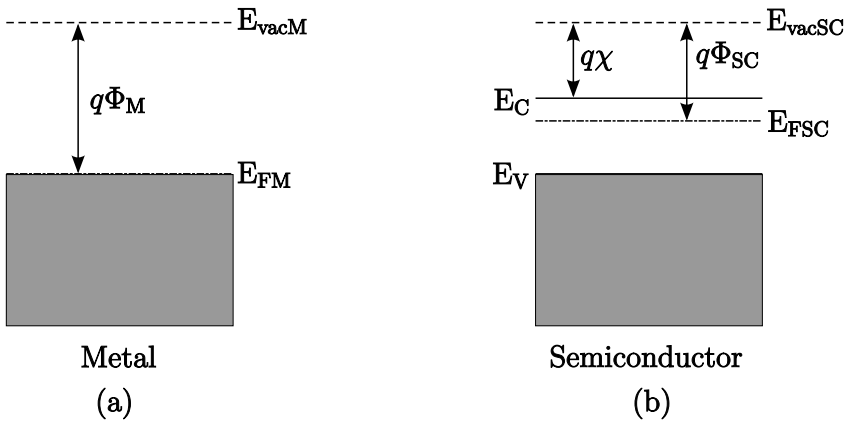

Figure 1.2: Energy band diagrams of (a) a metal and (b) a semiconductor, respectively.

1.2.2 Energy band diagram of a metal-semiconductor contact

To understand the formation of MS contacts, we can consider infinitely separated materials, beyond any mutual influence, and see what happens when they come into contact, how thermodynamic equilibrium is established. Before that, it is important to briefly discuss the problem of the energy reference.

For infinitely separated materials, the Fermi level is constant but it cannot serve as an energy reference for both materials. They are isolated from each other and their respective Fermi levels are in no way related to each other. However, since the potential energy of an electron in the vacuum is a priori the same for any material (i.e. $E_{vacSC} = E_{vacM}$), both vacuum levels can be used as a reference. When the contact is established, the Fermi level must be unique and horizontal in the structure at thermodynamic equilibrium. The vacuum level on each side is then determined by the respective work functions. It will not especially be constant throughout the structure since, in the semiconductor, the work function near the interface can be different from the bulk one, because it is affected by the electron redistribution.

On a thermodynamic point of view, two reservoirs of electrons, characterized by their respective Fermi levels, will reach (diffusive) equilibrium by a transfer of carriers, identically to two reservoirs of water reaching thermal equilibrium by heat transfer from the hottest to the coldest. The chemical potential (i.e. the Fermi level), which characterizes the

statistical distribution of electrons, plays the same role as the temperature in the establishment of the equilibrium: when the two materials are brought into contact, carriers diffuse from the material with the highest Fermi level and are redistributed in such a way that the Fermi level becomes unique throughout the structure. From the previous discussion, it follows that we can distinguish three cases for MS contacts (see Fig. 1.2): (1) $\Phi_{\mathrm{M}} = \Phi_{\mathrm{SC}}$ (or $E_{\mathrm{FM}} = E_{\mathrm{FSC}}$), (2) $\Phi_{\mathrm{M}} > \Phi_{\mathrm{SC}}$ (or $E_{\mathrm{FM}} < E_{\mathrm{FSC}}$), and (3) $\Phi_{\mathrm{M}} < \Phi_{\mathrm{SC}}$ (or $E_{\mathrm{FM}} > E_{\mathrm{FSC}}$). Considering the Schottky-Mott relationship (equation (1.1)), we can see that $\Phi_{\mathrm{B}n}$ is positive for cases 1 and 2 while it can be positive, null or negative for case 3.

Let us consider the case of a n-type semiconductor[4] with a given doping concentration. Suppose large and flat surfaces of metal and semiconductor parallel to each other. Moreover, the semiconductor is assumed not to possess surface states. In that case, when the separation is infinite, the energy bands of the semiconductor are flat up to the interface (as in Fig. 1.2).

1.2.2.1 $\Phi_{\mathrm{M}} = \Phi_{\mathrm{SC}}$

The band structure is not altered by the action of contacting the metal and the semiconductor since their Fermi and vacuum levels are already aligned before (Fig. 1.3(a)). The Fermi and vacuum levels of the unique structure are E_{F} and $\mathrm{E}_{\mathrm{vac}}$, respectively. Thermodynamic equilibrium is realized without any electron transfer through the interface. Because the bands are horizontal throughout the structure, the system is qualified “flatband” or “neutral”.

[4]The same reasoning can be easily applied to p-type semiconductors.

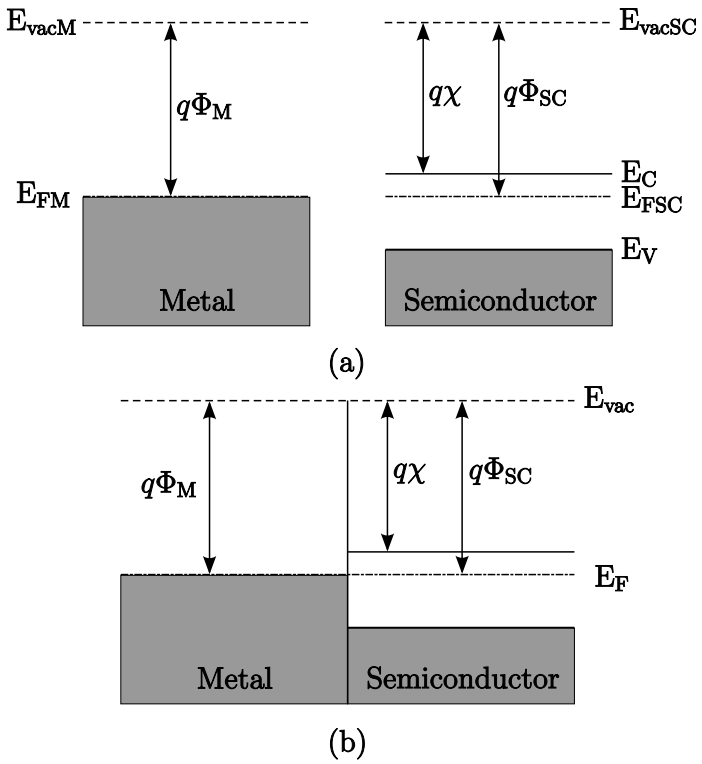

Figure 1.3: Energy band diagram of a flatband-type ($\Phi_M = \Phi_{SC}$) MS structure (a) before and after (b) contact, respectively.

1.2.2.2 $\Phi_M > \Phi_{SC}$

The energy band diagram before contact is depicted in Fig. 1.4(a). When the materials are stuck together (Fig. 1.4(b)), a transfer of electrons takes place from the conduction band of the semiconductor to the metal. During the process, each electron leaves a positively charged dopant atom behind. The ionized impurity atoms cause the establishment a built-in electric field that opposes the diffusion of electrons. Electrons flow into the metal until the balance is reached between the diffusion from the semiconductor into the metal and the drift of electrons in the semiconductor caused by the built-in electric field. The Fermi levels on both sides are then aligned.

The thin layer in the semiconductor right in contact with the metal, depleted of electrons, is called the depletion zone or the space charge region. In the energy band diagram in Fig. 1.4(b), the electron depletion is expressed by a progressive increase of the $E_C - E_F$ separation and an

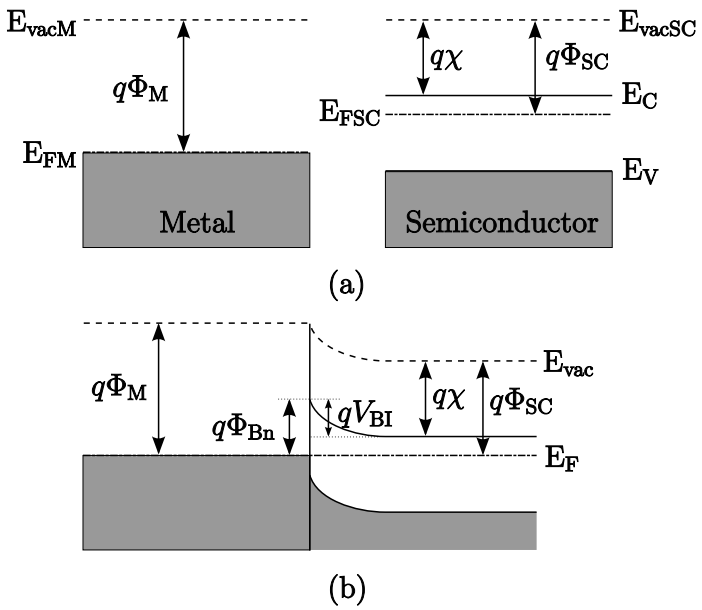

Figure 1.4: Energy band diagram of a depletion-type ($\Phi_{\mathrm{M}} > \Phi_{\mathrm{SC}}$) MS structure (a) before and after (b) contact, respectively.

upward band bending, since the Fermi level of the system is horizontal. The $E_{\mathrm{C}} - E_{\mathrm{F}}$ separation reaches a maximum at the interface, where the electron population is minimal. The accurate shape of this band bending (represented by the maximum of the potential at the MS interface, the so-called built-in voltage V_{BI}) in the depletion region will be calculated hereafter. The vacuum level in the semiconductor follows $q\chi$, since $q\chi$ is a constant and is independent of the doping concentration, contrary to $q\Phi_{\mathrm{SC}}$. The depletion charge is the only source of charges in the semiconductor since there are no surface states.

On the other hand, in the metal, which is considered as a perfect conductor, the transferred electrons accumulate in an infinitely thin layer on the metal side of the MS interface and no band bending occurs. The large size difference between space charge regions in the metal and the semiconductor is related to their respective charge concentrations. In a metal, the density of states in the conduction band is in the 10^{22} cm^{-3} range while, in the semiconductor, the density in ionized atoms depends on the doping level, typically 10^{15} to 10^{18} cm^{-3}.

These contacts can be called "depletion-type" contacts, in analogy to the MOS capacitor analysis. They are also called Schottky contacts. From Fig. 1.4(b), we can see that, for electrons coming from the metal,

the SBH $q\Phi_{Bn}$ is simply given by the difference between $q\Phi_M$ and $q\chi$, which is nothing else but the Schottky-Mott relationship (see equation (1.1)).

1.2.2.3 $\Phi_M < \Phi_{SC}$

Figure 1.5(a) shows the energy band diagram before contact. After contact, electrons migrate in the other direction, as opposed to the previous case, from the metal to the semiconductor. A positive space charge zone appears in the metal and a negative one in the semiconductor. Since the space charge zone in the semiconductor is enhanced with electrons (i.e. an accumulation layer), the band bending is downward (see 1.5(b)). Compared to the metal, the space charge in the semiconductor spreads over a much larger area. However, its size is much smaller than the depletion zone of the previous case since the effective density of states in the conduction band is approximately 10^{19} cm^{-3}. This kind of structure is called an "accumulation-type" contact.

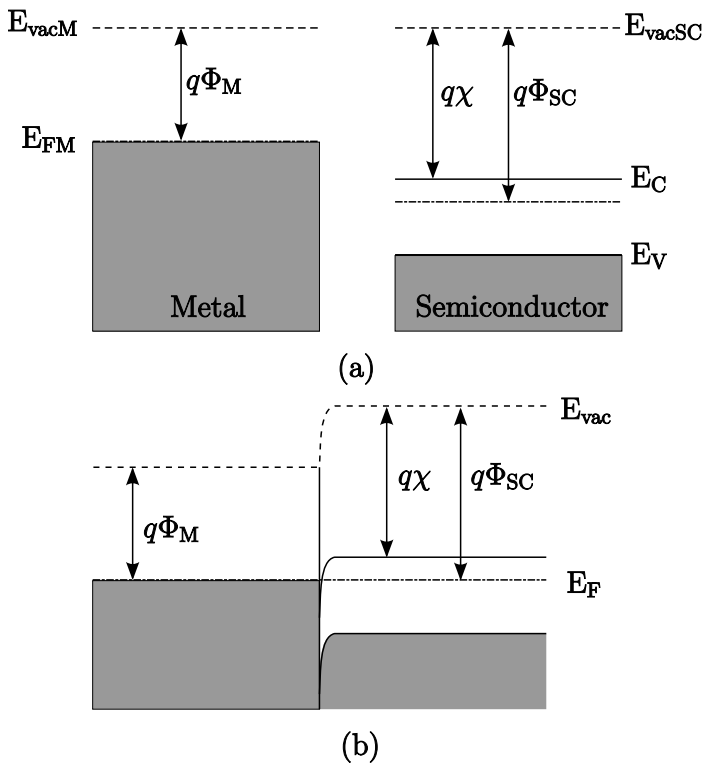

Figure 1.5: Energy band diagram of an accumulation-type ($\Phi_M < \Phi_{SC}$) MS structure (a) before and after (b) contact, respectively.

1.3 Schottky barrier height models

In practice, however, it is difficult to obtain flatband- or accumulation-type MS contact. In general, most of MS contact are of Schottky-type on both *n*- and *p*-type semiconductors. As already mentioned in section 1.1, it is hard to alter the barrier height taking advantage of the large range of avalailable work functions because of the Fermi level pinning. For about seventy years, a lot of work has been dedicated to understand the formation mechanisms of Schottky contacts and more specifically the physical origin of the Fermi level pinning.

In the present section, our intention is to detail the main concepts related to SB formation[5] without running the risk the reader to fall asleep. Many other soporific reference books could for sure better achieve the job!

[5]The same concepts having already been introduced before, in section 1.1.

First, we present the model conceived by Schottky for the depletion region. Then we give a mathematical proof of the Schottky-Mott relationship. It is next shown how the occurrence of surface states causes Fermi level pinning near their CNL. Thereafter, the CNL concept is used to develop the fixed separation model of surface states. The last part of the section is devoted to models for intimate MS contacts namely MIGS and the bond polarization theory.

1.3.1 Schottky's model of the depletion zone

Before we go deeper into details about the various models developed to describe Schottky contacts, we present the model of the depletion zone, as proposed by Schottky in 1941 [49].

Suppose an n-type semiconductor with a donor concentration N_{D}. The electrostatic potential $\phi(x)$ is defined as $\frac{1}{q}\Big[E_{\mathrm{Cbulk}} - E_{\mathrm{C}}(x)\Big]$ where E_{Cbulk} is the value of the conduction band maximum in the semiconductor bulk. It can be evaluated in the depletion zone by means of the one-dimensional Poisson equation:

$$\frac{\mathrm{d}^2\phi(x)}{\mathrm{d}x^2} = -\frac{\rho(x)}{\epsilon_{\mathrm{SC}}} = -\frac{q}{\epsilon_{\mathrm{SC}}}(N_{\mathrm{D}}^{+}(x) - n(x) + p(x)), \tag{1.2}$$

where ρ is the charge density, ϵ_{SC} the dielectric permittivity of the semiconductor, N_{D}^{+} the concentration in ionized donor impurities, n the electron density in the conduction band, and p the hole density in the valence band. At room temperature, all the impurities are ionized, which means that $N_{\mathrm{D}}^{+} = N_{\mathrm{D}}$. Schottky's depletion approximation assumes that (i) the charge in the semiconductor is uniquely due to the ionized impurities, meaning that the free electron and hole concentration is negligible relatively to N_{D} ($n, p \ll N_{\mathrm{D}}$) and (ii) that the corresponding charge density is constant throughout the depletion zone. In that case, ρ is simply assumed to be a step function:

$$\rho(x) = \begin{cases} qN_{\mathrm{D}} & \text{for } 0 < x < w \\ 0 & \text{for } x > w, \end{cases}$$

where w is the depletion width.

Setting the origin of the x-axis where the depletion zone ends in the semiconductor and the orientation towards the MS interface (see Fig. 1.6), $\phi(x)$ is readily calculated to be equal to:

$$-\frac{qN_{\mathrm{D}}}{2\epsilon_{SC}}x^2, \tag{1.3}$$

with the following boundary conditions: $\phi(0) = 0$ and $\frac{\mathrm{d}\phi(x)}{\mathrm{d}x}\big|_{x=0} = 0$. The corresponding electric electric field $\boldsymbol{E}$ is:

$$-\frac{qN_{\mathrm{D}}x}{\epsilon_{SC}}\hat{\boldsymbol{x}}, \tag{1.4}$$

with $\hat{\boldsymbol{x}}$ the x-axis unit vector. The depletion width is simply calculated by imposing that $\phi(w) = -V_{\mathrm{BI}}$, leading to:

$$w = \sqrt{\frac{2\epsilon_{SC}}{qN_{\mathrm{D}}}V_{\mathrm{BI}}}, \tag{1.5}$$

where the built-in potential V_{BI} is given by:

$$qV_{\mathrm{BI}} = q\Phi_{\mathrm{B}n} - qV_{\mathrm{N}},$$

with qV_{N} the difference between E_{C} and E_{F}.

The surfacic charge density in the depletion region is simply given by:

$$Q_{\mathrm{SC}} = qN_{\mathrm{D}}w = \sqrt{2qN_{\mathrm{D}}\epsilon_{\mathrm{SC}}V_{\mathrm{BI}}}. \tag{1.6}$$

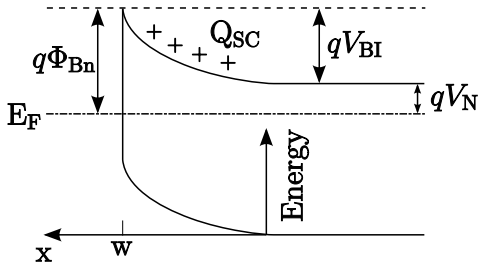

Figure 1.6: Energy band diagram of a MS heterostructure.

1.3.2 Non interacting Schottky barrier height models

Non interacting models of the SB formation include the Schottky-Mott model and various models based on the fixed separation view of the interface states. They suppose that no intimate contact is made between the metal and the semiconductor and that there is *a fortiori* no charge rearrangement at MS interfaces.

1.3.2.1 The Schottky-Mott model

In section 1.2.2, we have presented an intuitive approach to explain the formation of a Schottky contact and how to determine the Schottky-Mott relationship from an energy band diagram of the structure. We now give a mathematical derivation of the same relationship based on a *Gedankenexperiment*, as proposed by Tung [50]. The hypotheses are exactly identical as before, except that an electrical connection is now made between the metal and the semiconductor, resulting in the alignment of the Fermi level both sides before contact (see Fig. 1.7). In other words, the metal and the semiconductor are in thermodynamic equilibrium.

Suppose a tiny gap between the semiconductor and the metal. Since $\Phi_{\mathrm{M}} > \Phi_{\mathrm{SC}}$, there exists an electric field in the gap. This electric field can penetrate the semiconductor, which leads to the accumulation of identical charge densities with opposite sign on the surface of both solids. The electric field in the gap $\boldsymbol{E_\delta}$ can be calculated in a similar way to the

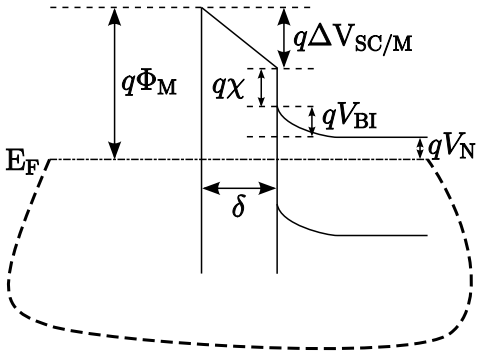

Figure 1.7: Energy band diagram of a semiconductor without surface states held at a distance δ from a metal. The metal and the semiconductor are connected to each other, resulting in a unique Fermi level through the system.

field between the two plates in a capacitor. The corresponding potential drop between the semiconductor and the metal is given by:

$$\Delta V_{\mathrm{SC/M}} = -\frac{Q\delta}{\epsilon_0},$$

with $Q = Q_{\mathrm{SC}}$, δ the gap width, and ϵ_0 the vacuum permittivity.

According to the energy band diagram in Fig. 1.7, we can determine that:

$$q\Phi_{\mathrm{M}} = q\chi + qV_{\mathrm{BI}} + qV_{\mathrm{N}} - q\Delta V_{\mathrm{SC/M}}.$$

Knowing the expression for Q_{SC} given by equation (1.6) that we combine to the previous equation, we can easily determine V_{BI} as a function of the gap width δ:

$$qV_{\mathrm{BI}}(\delta) = q\Phi_{\mathrm{M}} - q\chi - qV_{\mathrm{N}} + E_\delta - \sqrt{E_\delta\big(E_\delta + 2q\Phi_{\mathrm{M}} - 2q\chi - 2qV_{\mathrm{N}}\big)},$$

with

$$E_\delta = \frac{q^2\epsilon_{\mathrm{SC}}\delta^2 N_{\mathrm{D}}}{\epsilon_0^2}$$

the norm of $\boldsymbol{E_\delta}$.

We can see that, when the gap is infinite (and there is thus no interaction between the two materials), there is no band bending ($V_{\mathrm{BI}} = 0$). When the gap tends towards zero, $E_\delta = 0$, and one obtains:

$$qV_{\mathrm{BI}} = q\Phi_{\mathrm{M}} - q\chi - qV_{\mathrm{N}},$$

which is equivalent to the Schottky-Mott relation. It is a first order theory for the formation of a SB. As pointed out by Tung [50], the Schottky-Mott relationship is simply related to the absence of a gap between the semiconductor and the metal, and not to the absence of semiconductor surface states, as profusely expressed in the literature!

1.3.2.2 Charge neutrality level and Fermi level pinning

At the surface of any crystal lattice, where the periodicity is broken, there exist specific electronic states with no equivalent in the band structure of the bulk crystal. In the case of semiconductors, the presence of surface-specific states in the bandgap is known to pin the Fermi level of the semiconductor. To better understand the origin of the Fermi level pinning by surface states, we can introduce herethe concept of CNL.

At zero temperature, due to the step-like shape of the Fermi-Dirac statistics, the surface states are populated up to the Fermi level. The CNL is defined as the position of the Fermi level for which the net surface charge density is zero at 0 K, or, in other words, the surface is neutral. So, if the Fermi level is lower than the CNL, the surface presents a positive net charge while there is an excess of negative charges if the Fermi level is above the CNL.

Figure 1.8 features the energy band structure for a semiconductor with acceptor surface states. Electrons in the semiconductor populate the surface states. The occurrence of these negatively charged surface states involves the formation of a positive space charge region at the

semiconductor surface and an upward band bending. There is a pre-existing depletion region at the semiconductor surface even before any contact with the metal is made and the band diagram is no more flatband as it was in Figs. 1.3(a)-1.5(a).

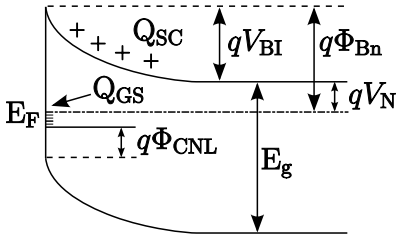

Figure 1.8: Energy band diagram for a semiconductor with surface states.

If one assumes that the density of surface states, D_{GS}, is roughly constant around the CNL, we can write, based on Fig. 1.8:

$$Q_{\mathrm{GS}} = qD_{\mathrm{GS}}(\Phi_{\mathrm{B}n} + \Phi_{\mathrm{CNL}} - E_{\mathrm{g}}) < 0,$$

where Q_{GS} is the gap states charge density, Φ_{CNL} the CNL position relatively to the maximum of the valence band, and $\Phi_{\mathrm{B}n}$ the difference between the minimum of the conduction band and the Fermi level at the surface of the semiconductor. It must be noted that $\Phi_{\mathrm{B}n}$ is only used by analogy to the SBH between an n-type semiconductor and a metal, since it is a convenient notation, even though there is no SBH in the present case. Charge neutrality at the interface ($Q_{\mathrm{SC}} + Q_{\mathrm{GS}} = 0$) leads to:

$$\sqrt{2\epsilon_{\mathrm{SC}} q N_{\mathrm{D}} V_{\mathrm{BI}}} + qD_{\mathrm{GS}}(q\Phi_{\mathrm{B}n} + q\Phi_{\mathrm{CNL}} - E_{\mathrm{g}}) = 0.$$

The position of the Fermi level relatively to the conduction band minimum at the interface is easily deduced from that equation:

$$q\Phi_{\mathrm{B}n} = E_{\mathrm{g}} - q\Phi_{\mathrm{CNL}} + \frac{\epsilon_{\mathrm{SC}} N_{\mathrm{D}} - \sqrt{\epsilon_{\mathrm{SC}}^2 N_{\mathrm{D}}^2 + 2\epsilon_{\mathrm{SC}} q^2 N_{\mathrm{D}} D_{\mathrm{GS}}^2 (E_{\mathrm{g}} - q\Phi_{\mathrm{CNL}} - qV_{\mathrm{N}})}}{q^2 D_{\mathrm{GS}}^2}. \quad (1.7)$$

The implication of surface states in Fermi level pinning clearly appears from that equation: even a relatively low value for D_{GS} positions the surface Fermi level close to the CNL. This is even more true for high D_{GS} since the last term of equation (1.7) tends towards 0 for $D_{\mathrm{GS}} \to +\infty$.

1.3.2.3 Surface states at metal-semiconductor interfaces: fixed separation model

In this section, we develop the most popular model that considers the influence of gap states on the electrostatics of the SB [33]. As explained in the previous section, the surface states essentially determine the band bending at the semiconductor surface. To account for deviations from the Schottky-Mott relationship, the fixed separation model supposes the presence of an interface dipole. The interface dipole is the central element of any theory attempting to explain Fermi level pinning [50]. The existence of this additional electric dipole involves a physical separation between charges of opposite sign. To create such a gap, the model artificially introduces a dielectric layer between the semiconductor (with surface states) and the metal. The MS interface properly speaking does not exist anymore! The model also makes the assumption that the gap states are a property of the semiconductor only. The influence of the metal on the SBH is reduced to its work function.

The energy band diagram of the structure is depicted in Fig. 1.9. The interfacial dielectric layer is characterized by a thickness δ_{int} and a

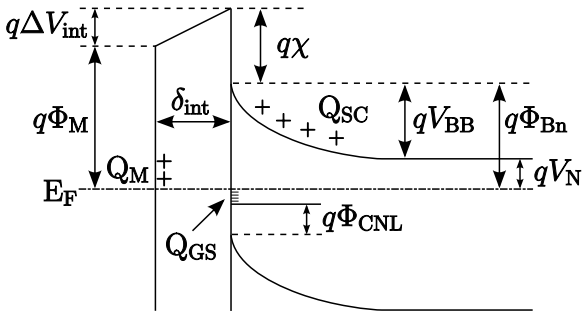

Figure 1.9: Energy band diagram for the fixed separation model of surface states. The metal and the semiconductor are separated by a dielectric layer.

permittivity ϵ_{int}. With the same definitions as in section 1.3.2.2, charge neutrality can now be expressed as:

$$Q_{\text{SC}} + Q_{\text{GS}} + Q_{\text{M}} = 0,$$

with Q_{M} the charge on the metal. Q_{M} is easily determined:

$$Q_{\text{M}} = \frac{\epsilon_{\text{int}} \Delta V_{\text{int}}}{\delta_{\text{int}}},$$

where ΔV_{int} is some kind of potential drop through the dielectric layer. Because ΔV_{int} symbolizes a correction to the Schottky-Mott relationship, it is called the "Schottky dipole" and can be written:

$$q\Delta V_{\text{int}} = q\Phi_{\text{B}n} - q\Phi_{\text{M}} + q\chi.$$

It is worth noting that the Schottky-Mott relationship is indeed restored if $\Delta V_{\text{int}} = 0$. Plugging the previous expressions for Q_{SC}, Q_{M} and Q_{GS} into the charge neutrality equation leads to:

$$\sqrt{2\epsilon_{\text{SC}} q N_{\text{D}} V_{\text{BI}}} + qD_{\text{GS}}(q\Phi_{\text{B}n} + q\Phi_{\text{CNL}} - E_{\text{g}}) + \frac{\epsilon_{\text{int}}(\Phi_{\text{B}n} - \Phi_{\text{M}} + \chi)}{\delta_{\text{int}}} = 0.$$

That equation is a second degree equation in $\Phi_{\text{B}n}$ and leads to a complicated expression for $\Phi_{\text{B}n}$. Usually, Q_{SC} is small comparatively to Q_{M} and Q_{GS} and can be neglected. With that approximation, the following expression can be found:

$$q\Phi_{\text{B}n} = q\gamma_{\text{GS}}(\Phi_{\text{M}} - \chi) + (1 - \gamma_{\text{GS}})(E_{\text{g}} - q\Phi_{\text{CNL}}), \tag{1.8}$$

where γ_{GS} is a constant defined by:

$$\gamma_{\text{GS}} = \left(1 + \frac{q^2 \delta_{\text{int}} D_{\text{GS}}}{\epsilon_{\text{int}}}\right)^{-1}.$$

It is interesting to note that γ_{GS} weakens the dependence of the SBH on Φ_{M}, in better agreement with the experimental observations. Moreover, if the density of gap states is very high (i.e. $\gamma_{\text{GS}} \ll 1$), the second term of equation (1.8) is dominant and the SBH is pinned near $E_{\text{g}} - \Phi_{\text{CNL}}$, the same result as the one established in section 1.3.2.2 but for MS contacts this time.

1.3.3 Models on bonds and dipoles at metal-semiconductor interfaces

Other models were developed to overcome the limitations of the non-interacting ones. Their main drawback is that these models do not work for intimate MS contacts (remember the dielectric layer). Indeed, they neglect the presence of interfacial chemical bonds that have a strong influence on the interface dipole and on the SBH itself. Hereabove, we give a short description of the two main rival approaches: the well-known MIGS model and the recently proposed bond-polarization model.

1.3.3.1 Metal-induced gap states

The MIGS model assumes that a metal in close proximity to a semiconductor can induce gap states, due to the penetration of the metal wave functions into the semiconductor, with a characteristic decay length. Nevertheless, it is important to notice that, even though MIGS are induced by the metal, they are actually supposed to be an intrinsic property of the semiconductor only. The presence of a continuum of gap states gives a metallic character to the semiconductor region in contact with the metal.

In this section, we only present the fixed separation version of the MIGS models (see Tung [50] for other models and more details). The model hypothesizes that the density of gap states, the CNL and the decay length are fixed for a given semiconductor, independently on the metal in contact with it!

This model is in fact identical to the fixed separation model for surface states presented in section 1.3.2.3. It assumes that the charge related to MIGS is still located on a plane at a fixed distance from the metal surface, to allow the existence of an electric dipole. The main difference with the previous model is that the dielectric layer is replaced by a superficial layer in the semiconductor where the metal wave functions penetrate and the MIGS are generated. The thickness of that layer roughly corresponds to the decay length of the MIGS δ_{GS}. In consequence, Fig. 1.9 is still adequate to describe the fixed separation model of the MIGS, even if the ingredients of the recipe are slightly different.

For a uniform density of MIGS, equation (1.8) is still valid, with slight modifications for γ_{GS} that can be written as:

$$\gamma_{\mathrm{GS}} = \left(1 + \frac{q^2 \delta_{\mathrm{GS}} D_{\mathrm{GS}}}{\epsilon_{\mathrm{GS}}}\right)^{-1}.$$

The permittivity is no more the permittivity of a dielectric layer but rather the permittivity of the interfacial semiconductor layer, ϵ_{GS}, where surface states penetrate. It is likely to suppose that ϵ_{GS} differs from ϵ_{SC}.

1.3.3.2 Bond-polarization theory

The main problem with the MIGS model resides in its basic assumption that the properties of the MIGS are determined by the semiconductor only, what is in clear disagreement with plenty of experimental results. Indeed, there is no *a priori* good reason to think that the response (i.e. the MIGS) does not depend on its "stimulus" (i.e. the metal). So, each MS interface must be characterized by a specific set of D_{GS}, Φ_{CNL},

and δ_{int}. That view is more representative of the chemistry at work at MS interfaces, which is usually different from a given MS couple to another, and is more in agreement with the intuitive picture of the SBH formation mechanism.

Following that line of thought, Tung proposed in 2000 [41] a physically sound theory to explain the Fermi level pinning, theory based on physico-chemical methods used to analyze the chemical bonds of small molecules. Tung's model assumes that the interfacial dipole arises from a transfer of charges between the metal and the semiconductor, considering the MS interface as a giant molecule. The charge transfer is assumed to occur only between the atoms directly involved in the interface bonds (see Fig. 1.10)! The interface is supposed to be atomically flat. Without

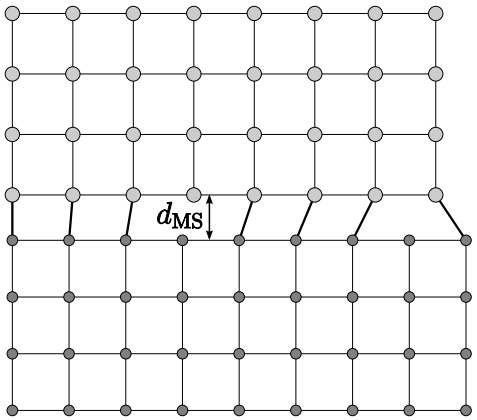

Figure 1.10: Schematic representation of the interface between two crystals. The charge transfer between the crystals is assumed to occur only between the atoms directly involved in the chemical bonds at the interface.

entering into the mathematical details, which can be found in Tung's very interesting paper [41], we directly jump to the final expressions for the Schottky dipole and the SBH, respectively:

$$\Delta V_{\text{int}} = -\frac{qN_{\text{B}}d_{\text{MS}}(q\Phi_{\text{M}} - q\chi - E_{\text{g}}/2)}{\epsilon_{\text{int}}(E_{\text{g}} + \kappa)},$$

$$q\Phi_{\text{B}n} = q\gamma_{\text{B}}(\Phi_{\text{M}} - \chi) + (1 - \gamma_{\text{B}})\frac{E_{\text{g}}}{2},$$

where

$$\gamma_{\text{B}} = 1 - \frac{q^2 N_{\text{B}} d_{\text{MS}}}{\epsilon_{\text{int}}(E_{\text{g}} + \kappa)},$$

with N_B the density of chemical bonds at the interface, d_{MS} the distance between the interfacial planes, and κ an energy parameter regrouping all the interactions between (direct) neighbor atoms (hopping interactions).

This equation has the same functional form as the equation for the fixed separation models (equation (1.8)), with $E_g/2$ instead of $E_g - \Phi_{CNL}$, even though both equations are obtained from very different basic physical hypotheses. The conceptual difference between the bond-polarization and the MIGS approaches is contained into γ_B.

1.4 Ohmic contacts

According to Sze and Ng [42], an "ohmic contact" is defined as a MS contact with a negligible junction resistance relative to the total resistance of the semiconductor device. A good ohmic contact should ideally not limit the current flowing through the device, with a voltage drop small enough compared with the drop across the active region of the device. It presents linear (ohmic) or quasi-linear current-voltage characteristics. Ohmic contacts are of prime importance in semiconductor technology since they provide an interface between the semiconductor device and the outside world.

Even if metals with sufficiently low work functions ($\Phi_M < \Phi_{SC}$) to produce very low or even negative SBHs do exist, "natural" ohmic contacts are rarely observed in practice because most of MS interfaces are plagued by Fermi level pinning. If it were the case, scientists would not be devoting so much effort into getting very low SBHs and the present thesis would be without purpose (at least from a practical point of view)!

The macroscopic parameter qualifiying an ohmic contact is the specific contact resistance ρ_c. It is defined as the reciprocal derivative of the specific contact resistance ρ_c with respect to the voltage across the interface V:

$$\rho_c \equiv \left(\frac{\mathrm{d}J}{\mathrm{d}V}\right)^{-1},$$

with units in $\Omega\,\mathrm{cm}^2$. When evaluated at $V = 0$, ρ_c is an important factor to measure the quality of ohmic contacts.

As already mentioned in the introduction, two solutions emerge to approach ideal ohmic contacts: (i) passivating the semiconductor surface to repair the defects causing Fermi level pinning (see Fig. 1.11(a)) or (ii) to introduce a thin high doping layer at the surface of the semiconductor to enhance current injection by tunneling (see Fig. 1.11(b)). With the first approach, interface states are suppressed and it is possible in principle to restore the Schottky-Mott relationship and to fabricate accumulation-like contacts with the appropriate metal. The second method proposes a

different philosophy consisting in "hiding" all the phenomena occurring at the MS interface behind a heavily doped shallow layer. An evolution of that technique is DS where an extremely thin and highly doped layer[6] is accumulated at the MS interface. Experimental realizations of this concept will be presented in chapter 4.

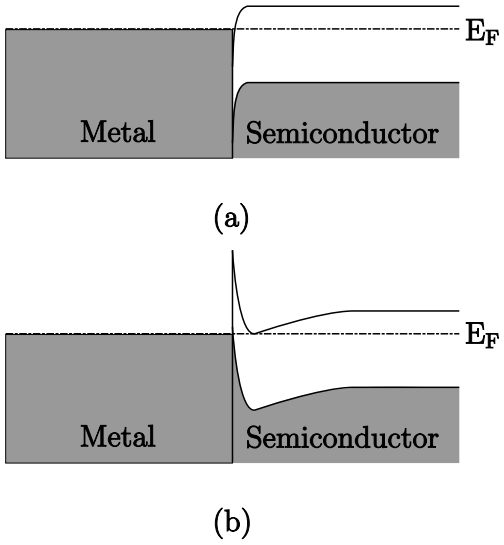

Figure 1.11: Energy band diagram for the two techniques to achieve ohmic contacts: (a) passivation and (b) high doping shallow junction.

In the remainder of the section, the discussion is limited to ohmic contacts realized by metallic contacts over highly doped junctions. A shallow doping layer with a high concentration at the semiconductor surface does not change the SBH properly speaking. On the other hand, it yields a thinning of the barrier promoting current injection into or out the contact via tunneling[7], resulting in an lower "effective" SBH.

The specific contact resistance can be expressed as [51]:

$$\rho_{\mathrm{c}} \propto \exp\left(\frac{4\pi\sqrt{\epsilon_{\mathrm{SC}} m^*}}{h}\left[\frac{\Phi_{\mathrm{B}}}{\sqrt{N}}\right]\right),$$

with N the doping of the shallow junction, m^* the effective mass in the semiconductor, and h the Planck constant. This equation is calculated from the expression for tunnel injection as derived by Padovani and

[6] Ideally a Dirac distribution.

[7] This is why this type of contact is sometimes called a "tunnel contact".

Stratton [52]. As we can see, ρ_c can be tuned via the SBH and/or the doping concentration.

The contact resistance R_C is also dependent on the current injection surface. With the device miniaturization, R_C becomes increasingly dominant. In a very simple case where the current density is uniform over the surface of the contact A, R_C and ρ_c are trivially related by:

$$R_C = \frac{\rho_c}{A}. \tag{1.9}$$

In the case of horizontal (or lateral) current flow into or out of a contact (typically in the case of a MOSFET) as featured in Fig. 1.12, the contact resistance is determined by [53]:

$$R_C = \frac{\rho_c}{L_T W} \coth(\frac{L}{L_T}),$$

where W is the contact width, L the contact length, $L_T = \sqrt{\rho_c / R_S}$ the transfer length, and R_S the sheet resistance of the diffusion layer. The transfer length can be thought as the length over which the voltage due to current transfer through the MS contact has dropped to $1/e$ of its maximal value. For $x \ll 1$ ($L \ll L_T$), $\coth(x) \approx \frac{1}{x}$ and we find that $R_C = \frac{\rho_c}{LW}$, identical to equation (1.9). In the other limit case ($L \gg L_T$), $\coth(\frac{L}{L_T}) \approx 1$ and $R_C = \frac{\rho_c}{L_T W}$, meaning that the effective (electrical) contact area $L_T W$ is much smaller than the actual (physical) surface LW. The current density flowing across the contact is then higher than if the contact was completely active, which can cause degradations to the device.

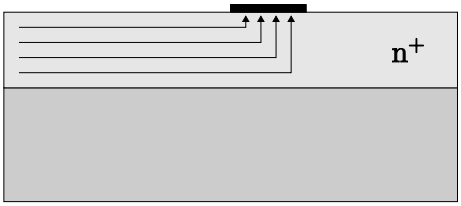

Figure 1.12: Current flow for a metallic contact to a horizontal diffusion layer.

1.5 Summary

In the present chapter, we presented an overview of the MS contact theory. The first section gave a chronology of the key achievements in

the field, from the first explanation of the rectifying effect by Schottky and Mott to the last major advance brought by the bond-polarization theory of Tung. Next, we reminded the concept of energy band both for metals and semiconductors. That consideration led to the distinction of three kinds of energy band diagrams for MS contacts. Afterwards, the principal SBH models found in the literature were exposed. First, non-interacting models, which assume no intimate contact between the metal and the semiconductor, have been reviewed. Then, the attention was focused on models on bonds and dipole at intimate MS interfaces. Finally, we discussed the ohmic contacts and introduced an important technological parameter, the specific contact resistance.

Chapter 2

Characterization techniques

After exposing the essence of the SB physics in chapter 1, we turn now to the electrical and physical characterization techniques that will be used extensively to study the properties of MS contacts. The first section is dedicated to electrical characterization and the second one to material characterization.

2.1 Electrical characterization

The understanding of current injection in MS rectifying junctions and how the current flow is affected by the SBH can be used to extract the SBH. To that purpose, we tackle hereafter the electronic transport through MS rectifying contacts also called "Schottky diodes". The first section deals with the principle of operation of the Schottky diode. Then, it is shown that the applied voltage has some influence on the SBH through the "Schottky effect". Next, the main part of the chapter is devoted to the electron transport mechanisms at work in the Schottky diode. Afterwards, the principal existing SBH extraction techniques are detailed. We also present the new method used in this work, more fitting to extract low SBHs. Finally, our experimental setup for SBH extraction is presented.

2.1.1 The Schottky diode

2.1.1.1 Principle of operation

The thermal equilibrium band energy diagram of the Schottky diode was already presented in chapter 1 at Fig. 1.4(b). Let us now examine what happens when an external bias is applied to the structure. If

we apply a forward bias (i.e. + on the metal and − on the semiconductor) V_{F}, the Fermi level in the semiconductor (still n-type) is raised with respect to the Fermi level in the metal (see Fig. 2.1(a)) and the equilibrium is disturbed. As a result, the barrier for electrons coming from the semiconductor is reduced to $q(V_{\mathrm{BI}} - V_{\mathrm{F}})$ (and the depletion region depth accordingly) and more electrons can diffuse from the semiconductor to the metal. On the other side, $\Phi_{\mathrm{B}n}$, the barrier for electrons flowing into the semiconductor, is independent on the polarization and remains unchanged. If a reverse bias V_{R} is applied to the system, the barrier for the electrons coming from the semiconductor is increased to $q(V_{\mathrm{BI}} + V_{\mathrm{R}})$ (see Fig. 2.1(b)). The electron flow is then limited by $\Phi_{\mathrm{B}n}$ and the Schottky junction exhibits a pronounced rectifying behavior. In both cases, equations (1.5) and (1.6) for the depletion width and charge remain valid, replacing V_{BI} by $V_{\mathrm{BI}} - V_{\mathrm{F}}$ or $V_{\mathrm{BI}} + V_{\mathrm{R}}$.

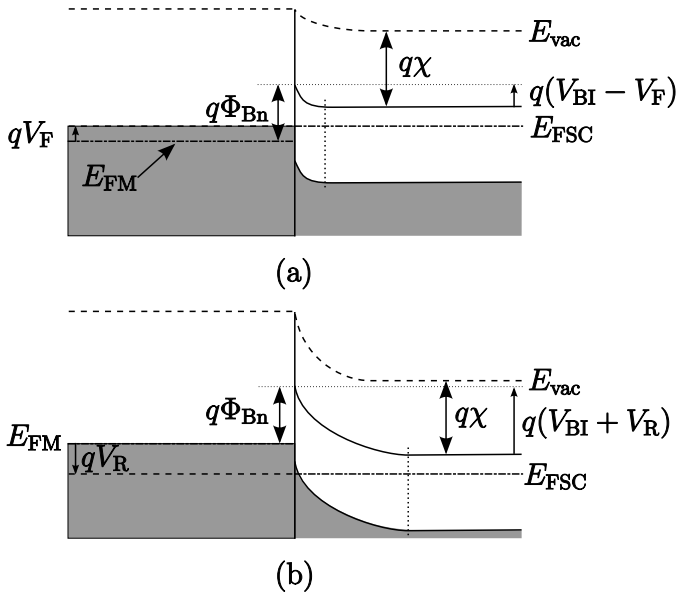

Figure 2.1: Energy band diagram of a Schottky junction under (a) forward and (b) reverse bias.

2.1.1.2 The Schottky effect

In reality, the SBH shows a slight dependence on the applied bias, through the Schottky effect. The Schottky effect is the lowering of the Schottky barrier due to the combined effect of the image-force of an

electron and the electric field in the depletion region. Indeed, image charges build up in the metal electrode of a MS junction as electrons approach the MS interface (see Fig. 2.2(a)). It can be shown that the resulting electric field in the semiconductor is identical to that of the carrier itself and another carrier with opposite charge at equal distance but on the opposite side of the interface (see Fig. 2.2(b)). This charge is called the image charge.

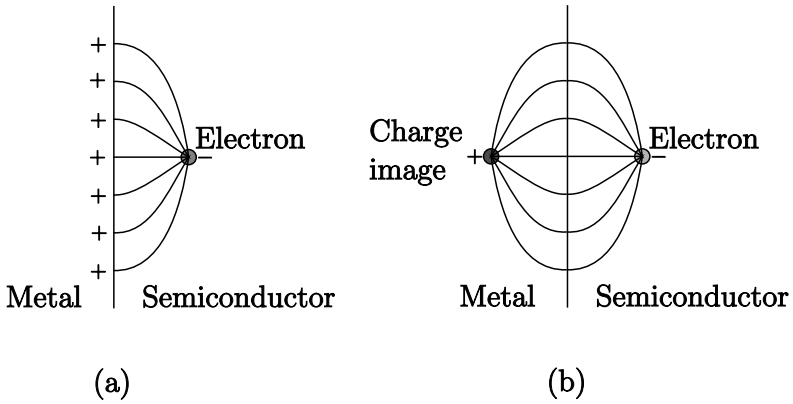

Figure 2.2: (a) Field lines and surface charges due to an electron in close proximity to a perfect conductor and (b) equivalent field lines due to an electron and its image charge.

The barrier lowering (BL) is determined by calculating the potential due to the image charge and adding it to the potential within the depletion region (see Fig. 2.3). The attractive electrostatic force $\boldsymbol{F}$ exerted between the electron at a distance x of the MS interface and its image charge is simply given by:

$$\boldsymbol{F} = \frac{-q^2}{4\pi(2x)^2\epsilon_{\mathrm{SC}}}\hat{\boldsymbol{x}} = \frac{-q^2}{16\pi\epsilon_{\mathrm{SC}}x^2}\hat{\boldsymbol{x}}.$$

This force confers the electron a potential energy $-\frac{q^2}{16\pi\epsilon_{\mathrm{SC}}x}$ relatively to an electron located at an infinite distance from the metallic plan. For the sake of simplification, the electric field in the depletion region is assumed to be constant and gives the electron a potential energy $-qEx$. Finally, the total potential energy of the electron PE is given by:

$$PE(x) = -\frac{q^2}{16\pi\epsilon_{\mathrm{SC}}x} - qEx.$$

The BL (also referred to as "image-force" lowering) $\Delta\Phi$ can be deter-

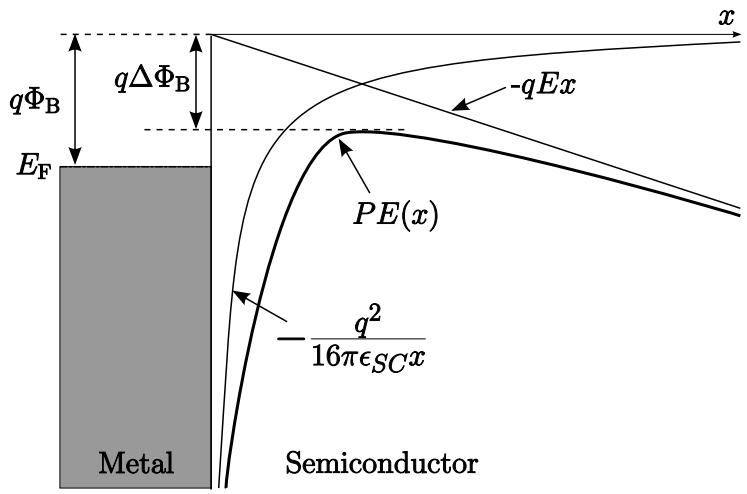

Figure 2.3: The Schottky effect results from the combined effects of the electric field in the depletion region and the image charge.

mined by calculating the minimum of PE, what leads to:

$$\Delta\Phi = \sqrt{\frac{qE}{4\pi\epsilon_{\mathrm{SC}}}}.$$

Finally, if we replace E by its maximum value i.e. at the MS interface ($E(w) = -qN_{\mathrm{D}}w/\epsilon_{\mathrm{SC}}$ from equation (1.4)), the BL can be written as:

$$\Delta\Phi = \sqrt[4]{\frac{q^3 N_{\mathrm{D}}}{8\pi^2\epsilon_{\mathrm{SC}}^3}(V_{\mathrm{BI}} - V_{\mathrm{F}})}.$$

2.1.1.3 Current transport mechanisms

Based on the energy band diagram displayed in Figs. 2.4(a) and 2.4(b), we can roughly discriminate three regimes for the current transport in a Schottky diode: (i) thermionic emission (TE) over the Schottky barrier, (ii) field emission (FE) near the Fermi level by tunneling through the barrier, and (iii) thermionic-field emission (TFE), combination of TE and FE, by tunneling of thermally excited carriers through a thinner barrier than FE. The relative contributions of each component depend on the absolute temperature and the doping level. For example, at room temperature, TE occurs at a low doping level ($\mathrm{N} \leq 10^{17}$ cm^{-3}), TFE is favored at moderate doping ($10^{17} \leq \mathrm{N} \leq 10^{19}$ cm^{-3}), and FE is promoted at high doping ($\mathrm{N} \geq 10^{19}$ cm^{-3}). A more general classification

is based on the comparison between the thermal energy kT (with k the Boltzmann constant and T the absolute temperature) and the parameter $E_{00} = \frac{qh}{4\pi}\frac{N}{m^*\epsilon_{SC}}$, which is characteristic of the semiconductor: TE, TFE, or FE dominates the current transport if $kT \gg E_{00}$, $kT \approx E_{00}$, or $kT \ll E_{00}$, respectively.

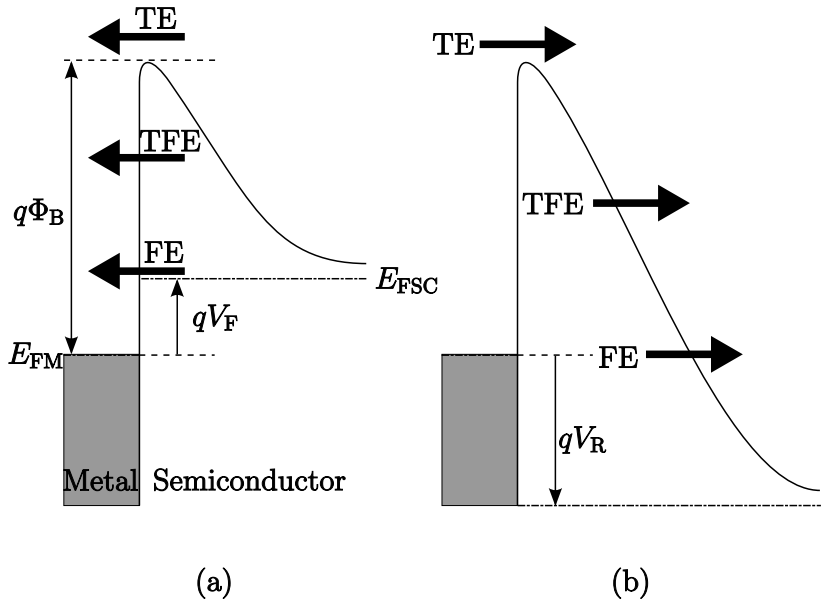

Figure 2.4: Energy band diagram of a Schottky diode with the three principal transport regimes (TE, TFE, and TE) under (a) forward bias and (b) reverse bias, respectively.

2.1.1.3.1 Thermionic emission At room temperature and without external bias, only a few electrons from the semiconductor will have enough thermal energy to overcome the barrier and to reach the metal. This current is noted $I_{s\to m}$ (after the notation used in [42]). This current is counterbalanced by a current in the opposite direction, from the metal to the semiconductor, $I_{m\to s}$. Without applied bias, we have thus: $I_{s\to m} = -I_{m\to s}$. In forward mode, since the SB for the electrons coming from the semiconductor is lowered, more electrons are transmitted to the metal and $I_{s\to m}$ increases. Simultaneously, the number of electrons flowing in the opposite direction remains unchanged and $I_{m\to s}$ is constant. In reverse mode, $I_{s\to m}$ decreases since the barrier increases while $I_{m\to s}$ keeps constant.

At room temperature and low doping, the electronic transport be-

tween the metal and the semiconductor is realized by TE above the Schottky barrier. Hans Bethe developed the TE theory from the hypotheses that (i) $q\Phi_{\mathrm{B}n} \gg kT$, (ii) thermodynamic equilibrium is established at the plane that determines emission, and (iii) the existence of a net current flow does not disturb this equilibrium. The corresponding current can be expressed as follows[1]:

$$I_{s\to m} = AA^*T^2 \exp(-\frac{q\Phi_{\mathrm{B}n}}{kT}) \exp(\frac{qV_{\mathrm{A}}}{kT}), \tag{2.1}$$

where A is the area of the contact, V_{A} the applied voltage, and

$$A^* = \frac{4\pi q m^* k^2}{h^3}$$

the effective Richardson constant for TE. Remembering that (i) $I_{s\to m} = -I_{m\to s}$ for $V_{\mathrm{A}} = 0$ and that (ii) $I_{m\to s}$ does not depend on V_{A}, $I_{m\to s}$ is readily deduced to be:

$$I_{m\to s} = -AA^*T^2 \exp(-\frac{q\Phi_{\mathrm{B}n}}{kT}).$$

The total current flowing through the MS junction is given by the sum of $I_{s\to m}$ and $I_{m\to s}$:

$$I = AA^*T^2 \exp(-\frac{q\Phi_{\mathrm{B}n}}{kT})\Big(\exp(\frac{qV_{\mathrm{A}}}{kT}) - 1\Big).$$

Taking into account the image-force lowering, the previous equation can be directly rewritten as:

$$I = AA^*T^2 \exp\Big(-\frac{q(\Phi_{\mathrm{B}n} - \Delta\Phi)}{kT}\Big)\Big(\exp(\frac{qV_{\mathrm{A}}}{kT}) - 1\Big).$$

Considering the semiconductor series resistance R_{SC} between the diode contacts, the equation can be finally modified as:

$$I = AA^*T^2 \exp\Big(-\frac{q(\Phi_{\mathrm{B}n} - \Delta\Phi)}{kT}\Big)\Big\{\exp\Big(\frac{q(V_{\mathrm{A}} - R_{\mathrm{SC}}I)}{kT}\Big) - 1\Big\}. \tag{2.2}$$

2.1.1.3.2 Thermionic-field emission Several models of TFE or FE exist, based on slighly different starting hypotheses. In the present text, we expose the approach developed by Crowell and Rideout [55], which has the advantage over the other models (for example Padovani and Stratton [52]) to provide a smooth transition between TE and FE transport regimes.

[1]The full derivation can be found in [42] or in the original paper of Bethe [54].

Forward mode The detailed energy band diagram of a MS interface is shown in Fig. 2.5, together with the definition of the variables. Let us introduce the energy $E_{\mathrm{BB}} = q(V_{\mathrm{BI}} - V_{\mathrm{F}})$, which represents the

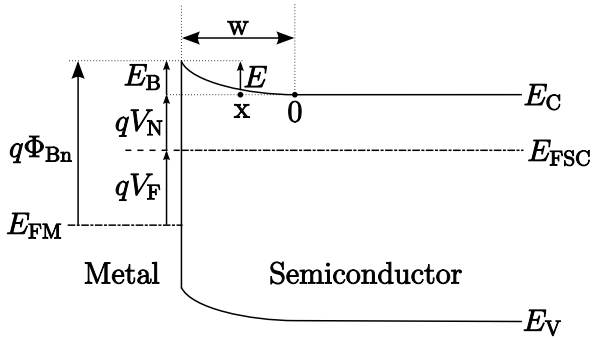

Figure 2.5: Detailed energy band diagram of a MS interface.

total band bending energy at the MS interface in the semiconductor depletion region. An electron at position x possesses an energy E relatively to E_{C}. The transmission probability τ through the SB under the Werner-Kramers-Brillouin approximation for $E < E_{\mathrm{BB}}$ is expressed as:

$$\tau(E) = \exp\Big[\frac{-4\pi}{h}\int_x^w \Big(2m^*(q\phi(x') - E)\Big)^{1/2}\Big]\mathrm{d}x'.$$

When $E \geq E_{\mathrm{BB}}$, the probability is equal to 1 and we are then in the case of pure TE.

The forward current density J_{F} (for carriers flowing from the semiconductor to the metal) can be written as:

$$\frac{A^*T}{k}\int_0^\infty f_{\mathrm{SC}}(E)\tau(E)\mathrm{d}E, \tag{2.3}$$

where f_{SC} is the occupation probability in the semiconductor. The occupation probability can be approximated by the Maxwell-Boltzmann distribution:

$$\exp(-\frac{E' - E_{\mathrm{FSC}}}{kT}) = \exp(-\frac{qV_{\mathrm{N}} + E}{kT}), \tag{2.4}$$

the electron energy E' being equal to $E_{\mathrm{FSC}} + qV_{\mathrm{N}} + E$ (see Fig. 2.5).

It is interesting to introduce here the flatband current density J_{m}, facilitating the final writing for J_{F}:

$$J_{\mathrm{m}} = A^*T^2\exp(\frac{-qV_{\mathrm{N}}}{kT}). \tag{2.5}$$

It corresponds to the absence of band bending i.e. $V_{\mathrm{F}} = V_{\mathrm{BI}}$ in equation (2.1). After integration (see appendix A for the complete calculation), the normalized forward current density can be written as:

$$\frac{J_{\mathrm{F}}}{J_{\mathrm{m}}} = \frac{E_{\mathrm{BB}}}{kT} \int_0^1 \exp\Big\{ \frac{-E_{\mathrm{BB}}}{kT} \big(\alpha + \frac{kT}{E_{00}} y(\alpha)\big) \Big\} \mathrm{d}\alpha + \exp(\frac{-E_{\mathrm{BB}}}{kT}), \quad (2.6)$$

where $\alpha = \frac{E}{E_{\mathrm{BB}}}$ is the normalized energy and $y(\alpha)$ is a dimensionless function defined as:

$$y(\alpha) = \sqrt{1-\alpha} - \alpha \log(\frac{1+\sqrt{1-\alpha}}{\sqrt{\alpha}}).$$

The first term of this sum represents FE (tunneling through the barrier for $E < E_{\mathrm{BB}}$) and the second one is nothing else but the TE component (see equation (2.1)).

Reverse mode Crowell and Rideout limited their calculations to the forward mode. The model was extended to the reverse mode by Dubois *et al.* [4]. In a similar way to the forward mode case, the reverse current density J_{R} (for carriers flowing from the metal to the semiconductor) can be written as:

$$\frac{A^* T}{k} \int_0^\infty f_{\mathrm{M}}(E) \tau(E) \mathrm{d}E,$$

where f_{M} is the occupation probability in the metal. When a non-equilibrium state under an externally applied voltage is considered, the occupation probability in the semiconductor and in the metal are connected through the following relationship:

$$f_{SC}(E) = \exp\big(\frac{-(qV_{\mathrm{N}} + E)}{kT}\big) = f_M(E) \exp(\frac{qV_{\mathrm{F}}}{kT}),$$

what directly implies that J_{F} and J_{R} are related by the following relationship:

$$J_{\mathrm{F}} = J_{\mathrm{R}} \exp(\frac{qV_{\mathrm{F}}}{kT}).$$

Since $V_{\mathrm{R}} = -V_{\mathrm{F}}$, the previous equation becomes:

$$J_{\mathrm{R}} = J_{\mathrm{F}} \exp(\frac{qV_{\mathrm{R}}}{kT}).$$

From equation (2.6), it is easy to show that J_{R} can be expressed as:

$$\frac{J_{\mathrm{R}}}{J_{\mathrm{r0}}} = 1 + \frac{E_{\mathrm{BB}}}{kT} \int_0^1 \exp\Big\{ \frac{-E_{\mathrm{BB}}}{kT} \big(\alpha - 1 + \frac{kT}{E_{00}} y(\alpha)\big) \Big\} \mathrm{d}\alpha,$$

with

$$J_{\mathrm{r0}} = A^* T^2 \exp(\frac{-q\Phi_{\mathrm{B}}}{kT}).$$

2.1.2 Determination of the Schottky barrier height

Basically, the methods to measure SBHs can be regrouped into two categories: photo-emission and electrical measurements. The electrical characterization techniques of Schottky diodes are: (i) current-voltage (I-V), (ii) capacitance-voltage (C-V), and (iii) activation-energy. The purpose of this section is to review the previous methods and to put the emphasis on their limitations when applied to the extraction of (very) low SBHs on low doping semiconductor substrates. After constructively criticizing the previous techniques, we justify the new method extensively used throughout the present text.

2.1.2.1 Photoemission measurement

Photoemission measurement relies on the well-known photoelectric effect whose theoretical description was developed by Fowler [56]. The working principle is illustrated in Fig. 2.6(a). When a MS junction is illuminated by photons with an energy $h\nu$ (with ν the light frequency) higher than the SBH ($\mathrm{h}\nu > q\Phi_{\mathrm{B}n}$), electrons can be emitted from the metal to the semiconductor (process 1 in Fig. 2.6(b)), giving rise to a photocurrent. In addition to photoemission, there is a second contribution to the photocurrent by band-to-band excitation (process 2 in Fig. 2.6(b)). This mechanism is parasitic and can be avoided if $\mathrm{h}\nu < E_{\mathrm{g}}$. The photocurrent is measured and can be used to calculate the photoyield which represents the photocurrent per absorbed photon. The SBH is then extrapolated from Fowler plots, i.e. the photoyield versus the incident photon energy.

The technique is appropriate to the extraction of midgap SBHs (at least 0.4 eV) but not to band-edge SBHs for the following reasons. First, the analytical expression of the photoyield becomes inaccurate for high and small photon energies. Secondly, the photocurrent level is typically in the μA range and is plagued by thermally-activated current (especially for low SBHs), which renders its detection rather difficult.

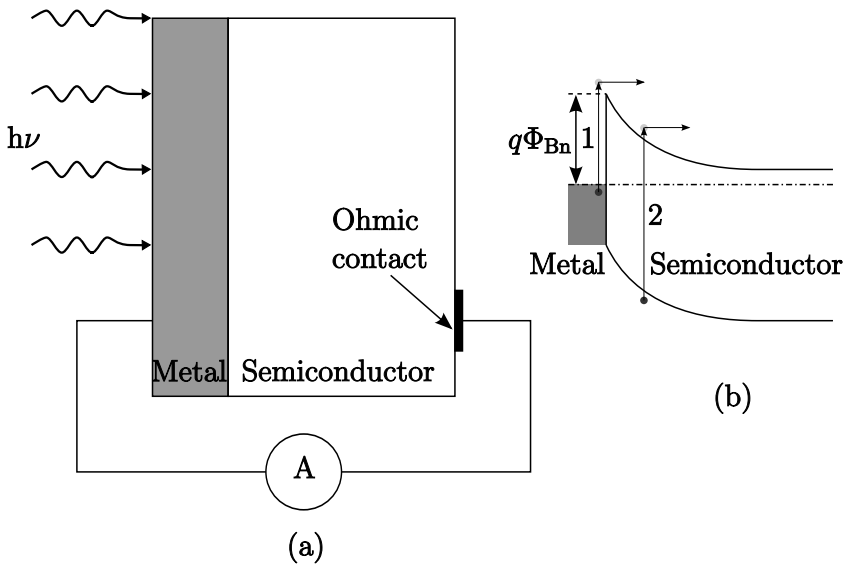

Figure 2.6: Working principle of the photoemission technique.

2.1.2.2 Electrical techniques

2.1.2.2.1 Current-voltage technique The I-V characteristics of the Schottky diode in forward mode (considering only TE) was given by equation (2.2). Since A^* and $\Delta\Phi$ are weak functions of the applied bias, this equation is often transformed into:

$$I = AA^*T^2 \exp\Big(-\frac{q\Phi_{\mathrm{B}}}{kT}\Big)\Big\{\exp\Big(\frac{q(V_{\mathrm{A}} - R_{\mathrm{SC}}I)}{\eta kT}\Big) - 1\Big\},$$

where the ideality factor η is an empirical constant used to account for all dependences on the applied bias and/or the temperature. If R_{SC} is negligible, η can be written as:

$$\begin{aligned}\eta &\equiv \frac{q}{kT}\frac{\mathrm{d}V_{\mathrm{A}}}{\mathrm{d}(\ln I)} \\ &= \Big(1 + \frac{\mathrm{d}\Delta\Phi}{\mathrm{d}V_{\mathrm{A}}} + \frac{kT}{q}\frac{\mathrm{d}\ln(AA^*)}{\mathrm{d}V_{\mathrm{A}}}\Big)^{-1}.\end{aligned}$$

As far as the extraction of low or very low SBHs on low doping semiconductors is concerned, the I-V method proves somewhat inaccurate because R_{SC} strongly dominates the total resistance of the system. Another drawback is the introduction of the ideality factor η which could hide many other physical mechanisms at work in the current transport.

Finally, the proper measurement of a Schottky diode requires a back-side ohmic contact which could affect the determination of very low SBHs since their impact on the current could be of the same order of magnitude.

2.1.2.2.2 Capacitance-voltage technique If the electron concentration n is not neglected in equation (1.2), the depletion charge Q_{SC} can be shown to contain a supplementary term [40]:

$$\sqrt{2\epsilon_{\mathrm{SC}} q N_{\mathrm{D}} (V_{\mathrm{BI}} - V_{\mathrm{A}} - kT/q)}.$$

It is preferable to work in reverse mode ($V_{\mathrm{A}} = -V_{\mathrm{R}}$) since the capacitance associated to the depletion zone C_{D} is larger. In that case, C_{D} can be calculated as:

$$C_{\mathrm{D}} = \frac{\partial Q_{\mathrm{SC}}}{\partial V_{\mathrm{R}}} = \sqrt{\frac{q\epsilon_{\mathrm{SC}} N_{\mathrm{D}}}{2(V_{\mathrm{BI}} + V_{\mathrm{R}} - kT/q)}}.$$

Reminding that $V_{\mathrm{BI}} = \Phi_{\mathrm{B}n} - V_{\mathrm{N}}$, $\Phi_{\mathrm{B}n}$ can determined from $1/(C_{\mathrm{D}})^2$-V_{R} plots by the following relationship:

$$\Phi_{\mathrm{B}n} = V_{\mathrm{N}} + kT/q - V_{\mathrm{Rint}},$$

where V_{Rint} is the intercept on the voltage axis.

Several criticisms can be emitted as for the application of the C-V technique to very low SBH extraction on low doping substrates. First, a precise extraction of V_{Rint} depends on the linearity of the $1/(C_{\mathrm{D}})^2$-V_{R} diagram that can be altered by unaccounted for BL mechanisms (image-force, etc.). In addition, a low doping value implies a steep slope and an inaccurate determination of V_{Rint}. The technique supposes depletion of the semiconductor layer in contact with the metal, correct assumption for high barriers but not necessarily for low ones. Finally, for low SBHs, a non negligible current component can be emitted over the barrier by TE and must consequently be taken into account in addition to the displacement current associated to the capacitance. All previous criticisms point out that the C-V method is inefficient for low SBH measurements.

2.1.2.2.3 Activation-energy technique The big advantage of that technique is that it does not require the knowledge of the current injection area. As we already mentioned in section 1.4, the actual (geometric) contact area can considerably differ from the electrical surface of injection.

The method is once again based on the thermionic equation (2.2), used either in forward or in reverse mode. In forward mode, neglecting the effect of R_{SC} and $\Delta\Phi$, the TE current equation can be transformed into:

$$\ln\left(\frac{I_F}{T^2}\right) = \ln(AA^*) - \frac{q(\Phi_B - V_F)}{kT},$$

with I_F the current in forward mode. I-V measurements are performed at several temperatures and a so-called "Arrhenius plot", which displays I_F/T^2 versus $1/T$, can be generated. The SBH is given by the slope of the Arrhenius plot. The main problem of the technique is the impact of R_{SC} on V_F. If R_{SC} is too large, it limits the current flowing through the system and renders the SBH extraction impracticable.

Alternatively, it is possible to reduce the voltage drop on R_{SC} operating in reverse mode, since most of the bias spreads over the Schottky junction. In that case, the reverse current I_R can be written as:

$$\ln\left(\frac{I_R}{T^2}\right) = \ln(AA^*) - \frac{q\Phi_B}{kT},$$

and the barrier can be determined the same way as in direct mode. For pure TE theory, the SBH is independent on V_R and I_R is supposed to saturate with V_R. In practice, however, I_R does not saturate because the SBH shows some dependence on V_R through BL ($\Delta\Phi(V_R)$) and tunneling. In addition, for low SBHs and low doping substrates, the effect of the R_{SC} must be accounted for, because the magnitude of I_R is much higher, causing a large voltage drop on R_{SC}. As previously, if R_{SC} limits the current flow, the separation of the respective contributions of the Schottky junction and R_{SC} is difficult and the SBH cannot be determined precisely.

Owing to all limitations of the classical methods exposed previously, Dubois *et al.* proposed to use Crowell and Rideout's model to extract low or very low SBHs. Remind here once again that the original model includes TE and FE, and is further enhanced with image-force lowering[2]. Both FE and image-force lowering introduce non negligible contributions to the total current that must be taken into account for an accurate SBH determination. The measured system is not a single Schottky diode but a symmetric structure (R_{SC} comprised between two "back-to-back" or "face-to-face" Schottky diodes for MS contacts on p- or n-type semiconductor, respectively) emulating the architecture of a SBMOSFET. It avoids the need to realize a backside ohmic contact that could impair an accurate SBH determination. The temperature dependence of R_{SC} is

[2]This model will be denominated as the "TFE+BL" model in the rest of the text.

modeled by a superlinear relationship:

$$R_{\mathrm{SC}} = R_{\mathrm{SC}}(300)\Big(\frac{T}{300}\Big)^{a},$$

where the coefficient a is greater than 1.

It is still an activation-energy method where a voltage V is applied between the two contacts and the resulting current I measured at various temperatures T. The Schottky contact can be qualitatively characterized by an equivalent Schottky resistance $R_{\mathrm{Sch}} = \big(\partial I/\partial V\big)^{-1}$ at low voltage. For given SBH and R_{SC}, the current is limited by R_{SC} at high temperature, while the transport is governed by R_{Sch} at low temperature (more specifically, I is limited by the diode in reverse mode). The I-V-T characteristics are converted into an Arrhenius plot where the ohmic and Schottky regimes can be clearly discriminated: positive slope in the ohmic regime since I increases with decreasing T and steep negative slope since I decreases exponentially with decreasing T. The Arrhenius plot is fitted thereafter with the previous model of the face-to-face structure. For a fixed V, we can define a transition temperature at which the current transport switches from ohmic to Schottky behavior ($R_{\mathrm{SC}} = R_{\mathrm{Sch}}$). The transition temperature is a good empirical indicator of the SBH because the lower the transition temperature, the lower the SBH. For the sake of illustration, typical experimental I-V-T characteristics and the corresponding Arrhenius plot for a contact between Er silicide and n-Si are given in Figs. 2.7(a) and 2.7(b), respectively. In both cases, the ohmic and Schottky regions are easily distinguishable from each other.

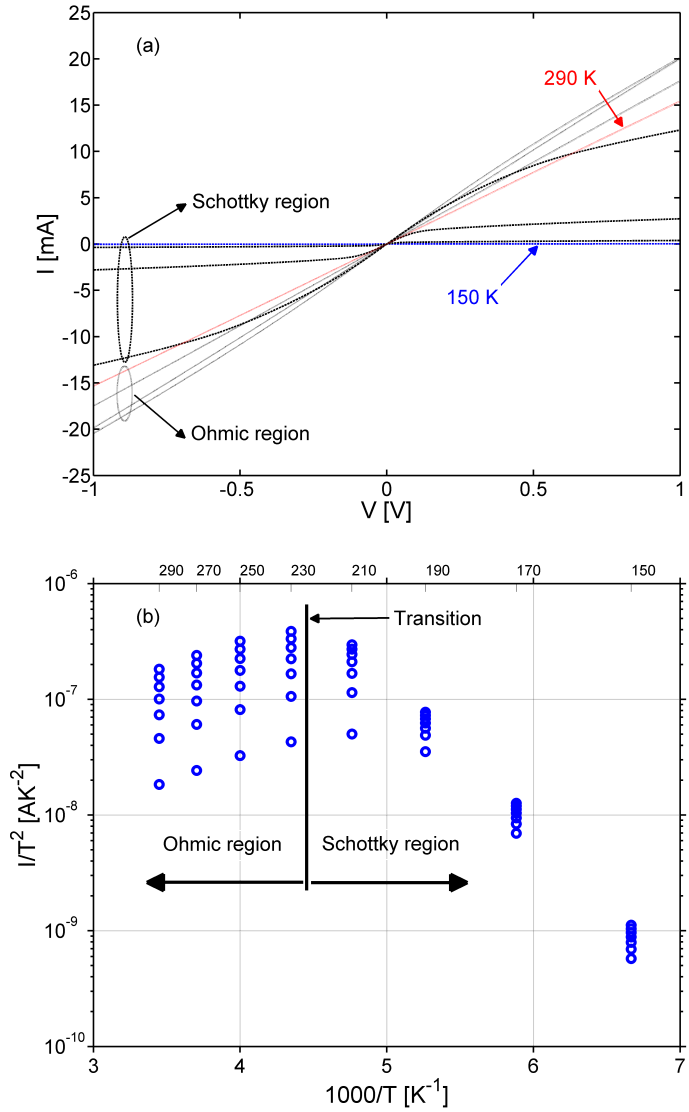

Figure 2.7: (a) Typical experimental I-V-T characteristics for a contact between Er silicide and n-Si. The measurements were performed between 150 and 290 K. The 150 and 290 K curves are colored in blue and red, respectively. The I-V curves in the ohmic and Schottky regions are dotted and dashed, respectively. (b) The corresponding Arrhenius plot, with the separation between the ohmic and Schottky regions.

2.1.3 Experimental setup for the Schottky barrier height extraction

The cryogenic system that we use to perform low temperature measurements is featured in Fig. 2.8(a). It consists in a can with a sample holder at one end which is introduced into a dewar filled with helium or nitrogen. The sample holder (see Fig. 2.8(b)) is wired to a Fischer push-pull connector located at the other end of the can. The location of the sample is indicated by the green ellipse and the thermometer by the red one. The Fischer connector is then joined to coaxial connectors fixed to a box (see Fig. 2.8(c)) via a cable. These coaxial connectors can be in turn linked to various instruments in a rack (sources, lock-in amplifiers, multimeters, etc.).

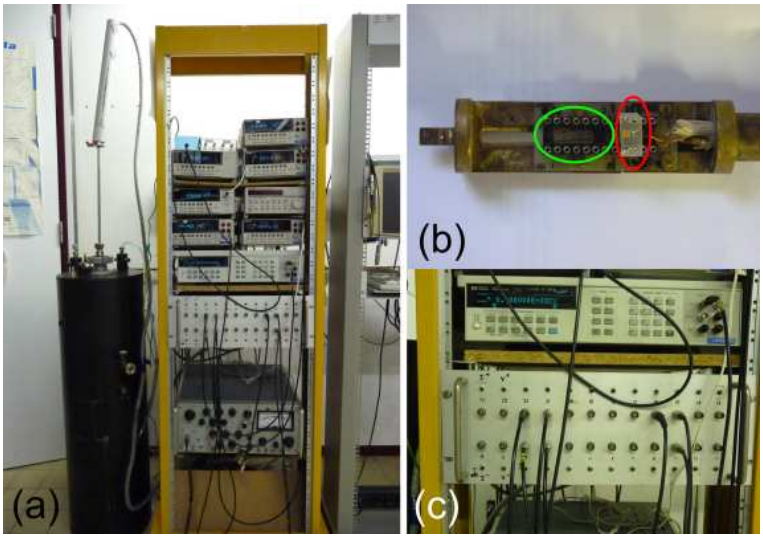

Figure 2.8: (a) Experimental setup used for low temperature SBH extraction: on the left side, dewar and can; on the right side, box with coaxial connectors and rack with measurement instruments. (b) Closer view on the box with coaxial connectors. (c) Sample holder.

In our work, the SBH is determined from I-V curves of two face-to-face Schottky diodes measured by four-point contact technique (remember section 2.1.2.2.3). A voltage (V_{2C}) is applied between two contacts and the real voltage drop (V_{4C}) is measured between the two other ones. The experimental I-V_{4C}-T curves are then transformed into Arrhenius plots for some selected V_{4C} biases. As depicted in Fig. 2.9, the face-to-face Schottky diodes are simply a two-contact structure (two large silicide

squares separated by a silicon gap). The sample holder necessitates to encapsulate the face-to-face Schottky diodes onto a chip with 16 pads. To do so, the wafer is diced in small pieces with diodes, then the pieces are stuck with epoxy on the chip and the diodes finally bonded with aluminium wires. We perform four-contact measurements to eliminate the parasitic resistances external to the device. The advantage of the wire bonding is that the contacts do not move during the measurement session due to cooling, contrary to probing with needles.

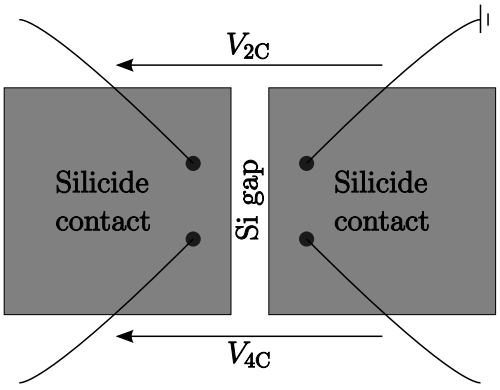

Figure 2.9: Top view of two silicided contacts bonded with four Al wires.

2.2 Physical characterization

The different methods for material characterization used in the present work are briefly detailed here. The purpose of this chapter is to provide the reader, who might not be familiar with these techniques, with sufficient information to understand the experimental results exposed in next chapters. We deal with four physical characterization methods namely "x-ray diffraction (XRD), "x-ray photoelectron spectroscopy" (XPS), "transmission electron microscopy" (TEM), and "secondary ion mass spectroscopy" (SIMS). Their description is inspired from the following reference books: [57] for XRD, [58] for XPS, [59] for TEM, and [45] for SIMS.

2.2.1 X-ray diffraction

When a wave characterized by a wavelength λ is sent on an array of regularly organized obstacles (planes of atoms in a crystal for instance) separated by a distance d the order of magnitude of λ, diffraction occurs.

The wave scatters over each obstacle, producing spherical waves which can interfere with each other. In most directions, the waves cancel out each other through destructive interference while they add constructively in a few specific directions, given by the well known "Bragg's law" (see Fig. 2.10):

$$2d\sin\theta = m\lambda,$$

with θ the incidence angle and m any integer.

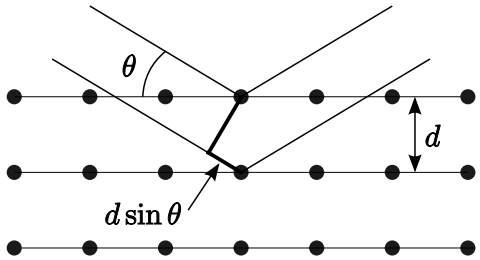

Figure 2.10: Schematic representation of wave diffraction by planes of regularly organized objects. Constructive interference occurs only in directions where the path-length difference $2d\sin\theta$ equals an integer multiple of λ.

If diffraction is applied to the peculiar case of atoms within a crystal, x-rays are used as incident waves, with typical wavelengths in the 1-100 Å range. The related technique is XRD. It is a very common method used to yield the crystalline structure of a given material. It relies on the elastic scattering of x-rays from the electronic cloud surrounding the atoms constituting the material.

Table 2.1 regroups the experimental configurations used in practice for diffraction. They are implemented in a way to satisfy Bragg's law. The "Debye-Scherrer" approach consists in collecting reflections from polycrystalline samples (most often as a powder) hit by a monochromatic radiation. A second technique, the "Laue" method, makes use of a polychromatic (or "white") source with a large spectrum of wavelengths illuminating a single crystal. The combination of a polycrystalline sample with a polychromatic beam is not useful because it produces too many diffractions. Finally, the structure determination of a specific crystal (which is our concern here) with a monochromatic source is called "single-crystal diffraction".

When they land on a screen, these scattered x-ray beams form a diffraction pattern of spots (for single crystals) or rings (for polycrystals), corresponding to constructive interferences. For single-crystal XRD, each

	Radiation	
Sample type	Monochromatic	Polychromatic
Powder	Debye-Scherrer	None
Single crystal	Single-crystal methods	Laue

Table 2.1: Experimental methods for diffraction.

spot is called a reflection, since it corresponds to the reflection of the x-rays from one set of evenly spaced planes within the crystal. In an x-ray diffractometer, as the crystal is gradually rotated, the intensities and angles of the diffracted beams are recorded by an x-ray detector and a goniometer, respectively. A typical diffraction pattern comprises a list of detector counts versus the angle(s).

In an x-ray powder diffractometer, the angles between the x-ray source, specimen, and detector must be accurately determined. More specifically, two angles are required: the angle of incidence called ω in the general case and the angle between the incident and detected beam (2θ). A very convenient disposition of the specimen, detector and source is the "Bragg-Brentano" geometry (see Fig. 2.11) i.e. the detector and the source are located on the same circle and the sample surface is tangential to the center of the circle and touches the geometrical diffractometer axis ($\omega = \theta$). Such a goniometer is called "two-circle" since two motors are necessary to perform the two circular movements. Two configurations are possible with the Bragg-Brentano geometry (in both cases, the detector is mobile):

- θ-2θ (Fig. 2.11(a)): the x-ray source is kept fixed and the sample holder can rotate. We can see that if the sample holder is in turn rotated by an angle θ^*, the detector is rotated by $2\theta^*$, hence its name. Mechanically speaking, it is the simplest mounting since the x-ray source is the heaviest part of the diffractometer.

- θ-θ (Fig. 2.11(b)): the x-ray source is mobile and the sample holder is fixed.

In a powder diffractometer, only two degrees of freedom are enough to modify the diffraction conditions (rotation of the sample and of the detector). In contrast, more degrees of freedom are required to obtain diffraction patterns from single crystals with a monochromatic wave. To get more information from those samples, it is necessary to rotate them in the three spatial directions. In comparison to polycrystalline specimens, diffractions from single crystals are more intense but measurements necessitate a considerable amount of time due to the additional

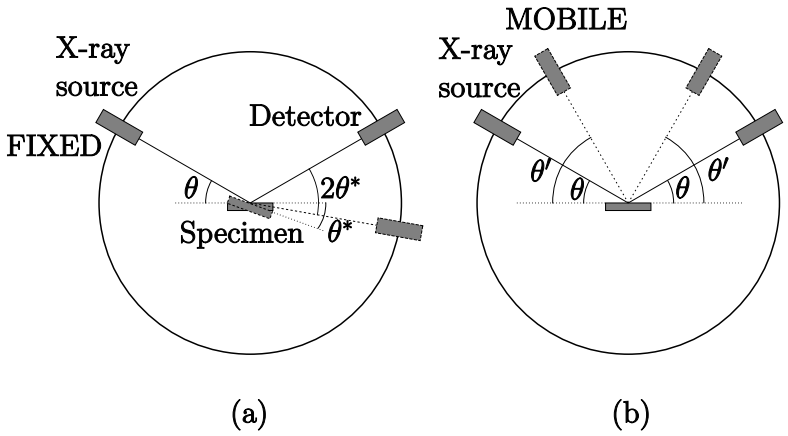

Figure 2.11: The two configurations in the Bragg-Brentano geometry (i.e. the detector and the source are located on the same circle): (a) θ-2θ and (b) θ-θ.

parameters. In addition to the detector angle 2θ and the incidence angle ω, we can add the tilt angle χ and the spin angle φ. Such a mounting is called a "four-circle" diffractometer and can be realized by the "eulerian geometry" illustrated in Fig. 2.12.

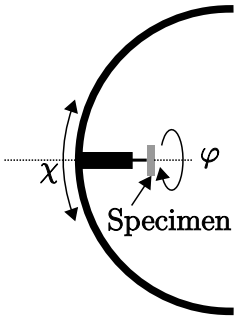

Figure 2.12: Vertical view of a four-circle diffractometer in the eulerian geometry, with the additional χ and φ angles.

2.2.2 X-ray photoelectron spectroscopy

"Photoelectron spectroscopy" is based on the well-known photoelectric effect: as a photon impacts on the surface of a material, an electron is liberated and emitted into vacuum with a given kinetic energy. This

technique can be used to determine the elemental composition, the empirical formula, the chemical state, and the electronic state of the elements (H and He excepted) which compose a material. For low energy photons ($E \leq 100$ eV), only electrons from the valence band can be extracted. The corresponding method is called "ultraviolet photoelectron spectroscopy". For more energetic photons (i.e. for XPS), electrons can be ejected from any orbital as long as their binding energy (BE) is lower than the incident photon energy. This allows to explore the core levels of a material, which depend on the chemical state of the sample. For that reason, XPS is also called "electron spectroscopy for chemical analysis".

It is a surface-sensitive technique because the emitted electrons originate from the very surface of the material (first 5-50 Å), even though the x-ray penetration depth is much higher (1-5 μm). All deeper photoemitted electrons, which are generated as the x-rays penetrate into the material, are either recaptured or trapped in various excited states within the material. The "electron escape depth" is defined as "the distance into the sample measured from the physical surface from which all but a fraction 1/e of the particles or radiation detected have originated". The escape depth is related to the "inelastic electron mean free path", which depends on the considered material and on the electron kinetic energy. Because of the very small electron escape depth, XPS requires to work under ultrahigh vacuum (UHV) conditions since any superficial contamination makes it impracticable. Another reason why UHV is mandatory is to allow the electron to reach without collision the detector which is located several tens of centimeters from the surface of emission. Depth profiling is possible with an ion gun that sputters the surface (typically Ar^+). The surface of the sample is analyzed between two sputtering cycles. The drawback of ion sputtering is that it can affect the oxidation state of the sample under analysis[3]. And it is of course a destructive technique. Another way to perform profiling is to tilt the sample (called "angle-resolved XPS").

Let us now give more details about the working principle of XPS (see Fig. 2.13). The photons from the light source impinge on the sample and the electrons excited by the photoelectric effect are analyzed with respect to their kinetic energy (E_K) and their momentum $\vec{p}$ (via their respective angle with the incident light and the surface). Knowing the energy of the light $h\nu$ and the work function of the material Φ, it is possible to extract the BE E_B (referenced to the Fermi level) of the electrons via

[3]This is of course more particularly the case for oxygen-sensitive elements like RE metals.

the following expression:

$$E_{\mathrm{K}} = h\nu - \Phi - |E_{\mathrm{B}}|.$$

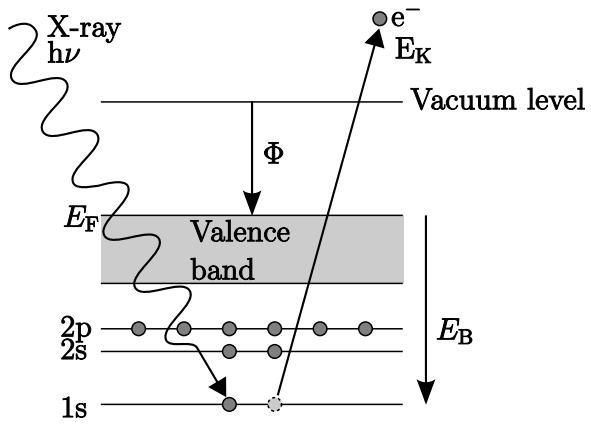

Figure 2.13: Working principle of XPS: an x-ray beam illuminates the surface of the sample. Core electrons are subsequently excited and emitted.

In practice, the photoemission is very often described by a process in three distinct and independent steps called the "three-step model". The first step is photoionization: one electron absorbs one photon and is thereby excited. During the second step, the electron travels through the sample to reach the surface. In the third and last step, the electron passes through the surface and enters into the vacuum where it can be detected. In principle, the photoemission should be considered as a whole. But the results obtained by the intuitive three-step model are not significantly different from those of a more realistic one-step theory.

A typical XPS spectrum is a plot of the number of electrons detected (sometimes per unit time) versus the BE of the electrons detected. Each element produces a characteristic set of XPS peaks at characteristic BEs that directly identify each element that exist in or on the surface of the material being analyzed. These characteristic peaks correspond to the electron orbitals of the electrons within the atoms, for instance, $1s$, $2s$, $2p$, $3s$, etc. The number of detected electrons in each of the characteristic peaks is directly related to the amount of element within the area (volume) irradiated. To generate atomic percentage values, each raw XPS signal must be corrected by dividing its signal intensity (number of

electrons detected) by a "relative sensitivity factor" and normalized over all of the elements detected.

2.2.3 Transmission electron microscopy

TEM is a microscopy technique whereby an electron beam is transmitted through a very thin sample. The interaction between the sample and the beam produces an image which can be visualized on a screen via CCD detectors (in modern instruments at least). In practice, the diffraction patterns from x-rays are more quantitative than their electron equivalent. In return, the latter present an important advantage: electrons are easy to focus. This implies that they can be used to study microscopic regions from a specimen and even single microcrystals. The working principle of a TEM can be visualized by means of the ray diagram for a two-lens system as shown in Fig. 2.14. The "back focal plane" of lens 1 (called the "objective lens") contains groupings of rays that have left the specimen at the same angle. The diffraction pattern of the sample is therefore formed at the back focal plane. An aperture (called the "objective aperture") can be placed there. The image of the specimen through lens 1 is focused in the "image plane". Lens 2 (the "intermediate lens") is used to either produce an image ("imaging mode") or a diffraction pattern ("diffraction mode") of the specimen on the "viewing screen".

In the simplest form of the imaging mode ("bright-field" or "aperture-less" imaging mode), all transmited and all diffracted electron beams leaving the specimen are combined to form an image on the viewing screen (see Fig. 2.14(a)). The bright-field image mode produces poor contrast images of the specimen. Thanks to the "objective aperture", it is possible to select either the transmitted beams (bright-field image mode, see Fig. 2.14(b)) or some specific diffracted beams ("dark-field" image mode, see Fig. 2.14(c)). This technique is called "diffraction contrast" and considers the variation in intensity of electron diffraction through the sample.

With another aperture placed in the image plane, it is possible to confine a diffraction pattern to a selected area of the sample (the size limit is around 1 μm). This mode is called "selected area diffraction". The techniques presented before belong to "conventional TEM".

To perform real nanodiffraction, more sophisticated techniques like "convergent-beam electron diffraction" must be used. With convergent-beam electron diffraction, the shape of the incident beam can be controlled accurately, which makes it possible to analyze nanometer size regions from the sample.

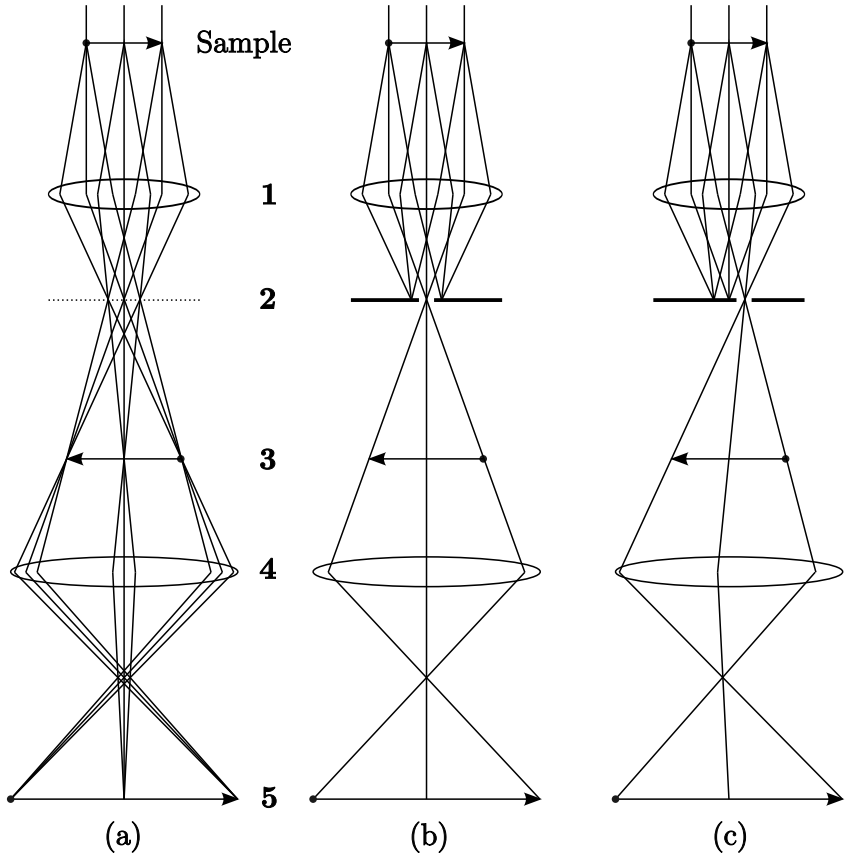

Figure 2.14: Ray diagram for a two-lens system, representative of the TEM optics: (a) apertureless bright field image mode, (b) bright field image mode, and (c) dark field image mode.

Besides the intensity of diffracted electron beams, it is also possible to take advantage of their phase. The phase of the diffracted electron wave is preserved after passing through the specimen and interferes with the transmitted beam. This technique of "phase-contrast imaging" is exploited in "high-resolution TEM" (HRTEM) to create pictures with atomic resolution.

In addition to imaging, the highly energetic electrons in the TEM can be used to perform "analytical TEM". These electrons can provoke electronic excitations in atoms of the sample and provide useful chemical informations. Two types of spectrometric techniques are:

- "energy-dispersive x-ray spectrometry" (EDS): a small region of the specimen is exposed to a focused electron beam and produces x-rays from electron deexcitations. The extracted x-ray spectrum allows for identifying the constituent atoms (characterized by specific energy peaks) and determining atomic concentrations (in a similar way to XPS).

- "electron energy-loss spectrometry" (EELS): the technique measures the energy losses of electrons to plasmons or core excitations after passing through the specimen.

2.2.4 Secondary ion mass spectroscopy

The basic principle of SIMS is illustrated in Fig. 2.15. Material from the analyzed sample is progressively removed by ion beam sputtering (the primary ion beam) and sent to a mass spectrometer. The secondary atom beam is constituted by the sputtered material and mostly contains neutral particles. A small fraction only (approximately 1%) is ejected as positive or negative ions and can be analyzed by the mass spectrometer, which determines the mass/charge ratio of the ions. This allows to reveal the elemental, isotopic, or molecular composition of the surface. SIMS is the most sensitive surface analysis technique, with detection limits in the 10^{12}-10^{16} cm^{-3} range, depending on the element.

During the sputtering process, ions transfer their momentum to atoms in the substrate, causing their displacement. Sputtering takes place when the incident projectiles transfer enough energy to the atoms of the surface to allow them to escape from the solid. The primary ions lose their energy as they come to rest in the sample and are consequently implanted into the specimen, causing lattice damage. The "sputtering yield" is defined as the average number of atoms sputtered per incident primary ion. It depends on the target material, its crystallographic orientation, and, of course, on the nature, energy, and incident angle of the primary ion

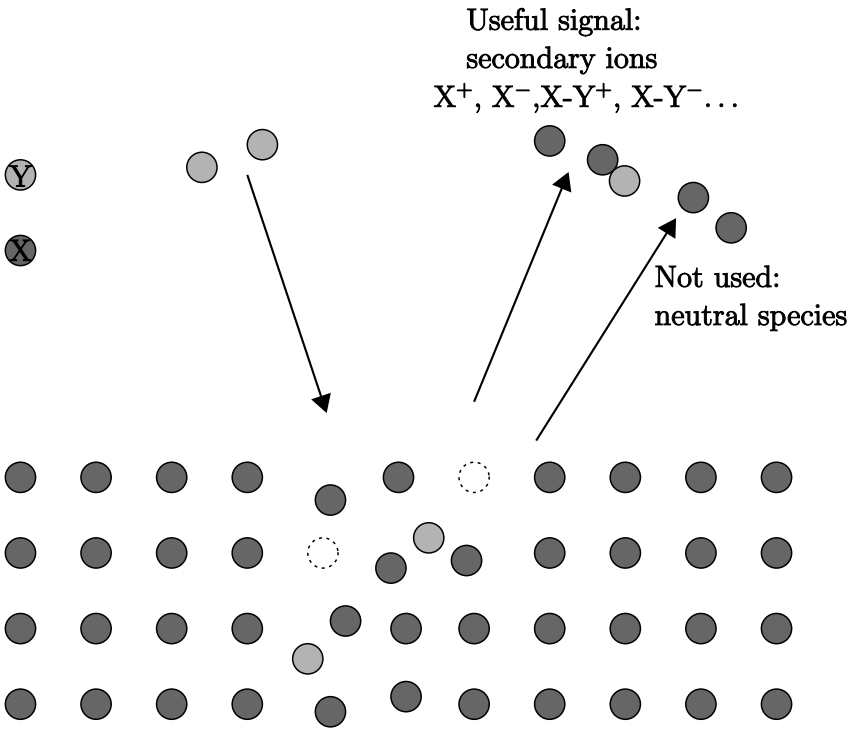

Figure 2.15: A primary beam of Y ions is projected over a crystal constituted by X atoms. A secondary ion beam containing ions of the type X^+, X^-, $X\text{-}Y^+$, $X\text{-}Y^-$, etc. is produced and analyzed by mass spectrometry.

beam. Typical primary ions are Cs^+, O_2^+, O^-, and Ar^+. What matters, in practice, is not the total yield but the yield of the ionized particles. For a given species, this secondary ion yield is influenced by the type of primary ions in use. For example, for Si, B, and Al (electropositive elements) are better detected by O_2^+ while As, P, and Sb (electronegative elements) have greater yields with Cs^+. SIMS can be used in two modes of operation: the "static mode", for very low sputtering rates and superficial analysis, and the "dynamic mode", at a higher sputtering rate, for depth profiling[4].

2.3 Summary

This second chapter described the electrical and material characterization techniques abundantly used in the experimental part of this thesis,

[4]This configuration is used in this work.

tackled in the next two chapters. The extraction techniques of the SBH are based on the electrical characteristics predicted by the theory of current injection in a Schottky contact. In consequence, the mechanisms of current transport in a Schottky diode were first detailed. We have illustrated that the current flow is the result of a combination between TE above the SB and FE through the SB. It was also shown that the voltage has an influence on the SBH through the Schottky effect. After assessing the different SBH extraction methods, we presented a new technique very appropriate to low SBH determination, combining TE, FE, and BL by image-force. In the second part of this chapter, we exposed the material characterization techniques, very complementary to get a clear picture of the material under study. XRD is useful for the unambiguous identification of crystalline compounds. XPS is a valuable tool to inspect a compound subject to chemical transformations. TEM can provide various informations, mainly structural and morphological, but also of crystallographic or chemical nature, and is probably the most comprehensive technique of all. Finally, SIMS is the most sensitive technique to detect very small concentrations of a chemical species into a material.

Chapter 3

Formation of Er silicide contacts

The present chapter is dedicated to the growth and the characterization of Er silicide thin films. We first give a very complete state of the art concerning the fabrication and the physical properties of RE silicide films, with a specific focus on Er silicide. The last two sections of the chapter detail the work performed during the thesis about the structural and electrical characterization of Er silicide grown in various conditions. Section 3.3 deals with Er silicide formed in UHV conditions while section 3.4 exposes growth by *ex situ* annealing with a protective capping layer.

3.1 Introduction

Among all existing metals, the RE elements, or lanthanides, are known to present the lowest SBH to n-Si. Only a few research groups provide a value for the SBH of RE silicides. The most studied one is Er disilicide, $ErSi_{2-x}$, which presents a SBH of about 0.28 eV [60, 61]. Classically, like other silicides, RE silicides are formed by metal deposition followed by heating, involving solid-state reaction with Si. In addition to exhibit the lowest SBH to electrons, RE silicides possess several other advantages such as a relatively low resistivity [60], a low lattice mismatch with Si [62] and the possibility of epitaxial growth [60, 62]. RE metals are also very sensitive to contamination by oxygen during deposition and annealing, and thus quickly oxidize [63,64], causing a deterioration of the quality of the formed silicide films and a possible increase in Φ_{Bn} [65]. This high sensitivity to oxygen implies the need to perform the annealing under special conditions. Ideally, the solid-state reaction should be performed *in situ* in UHV conditions, just after evaporation, without

breaking the vacuum. Alternately, if the vacuum is broken between the evaporation and the annealing, it is necessary to cover REs with a capping layer preventing the penetration of oxygen after deposition and stopping the diffusion of residual oxygen during *ex situ* annealing.

Furthermore, the formation of RE silicide films by solid-state reaction is commonly plagued by various kinds of defects [66, 67], like "pinholes", "pits" or pyramids. These defects result in short circuits or direct contact of upper layers to Si substrate, thereby degrading the device performance and decreasing device reliability. Their occurrence can be suppressed by deposition of an amorphous Si capping overlayer [66, 68, 69], pre-amorphization of the Si substrate [67] or deposition of an amorphous Si interlayer [70, 71].

3.2 State of the art

The list of references selected to write this state of the art is of course not an exhaustive one but it is representative of the most relevant publications related to RE silicides, and more specifically Er silicide. As much as possible, we try to expose the advances in the field following a chronological order. Those papers mainly deal with the process conditions necessary to get low SBH Er silicide contacts to *n*-Si with a good film morphology.

The first publication regarding the formation of RE silicides over a Si wafer [63] considers the solid-state furnace reaction (also called solid-phase reaction) of Er, Tb, and Y on Si(100) and Si(111) substrates. It is shown that the reactions on Si(111) occur at temperatures approximately 100 °C higher than the reactions on Si(100). The discrepancy might be due to a slower diffusion related to the Si substrate orientation. The as-formed alloys are Si-rich silicides (with a composition close to $RESi_{1.7}$) and present an hexagonal AlB_2-type structure, with defects in the occupancy of the Si sites (one out of six Si atoms is missing whence the notation $ErSi_{1.7}$ or $ErSi_{2-x}$ where $x = 1/6$). Furthermore, the reaction on Si(100) processes with dramatic suddenness within a few Kelvins, indicating that nucleation is probably the growth mechanism. For the authors, this "critical temperature" behavior suggests the existence of a sharp threshold for silicide growth by nucleation.

An alternate interpretation to the "threshold temperature" phenomenon is given in [70]. Ion implantation is used to modify the formation of silicide phases. With a low ion bombardment through the metal-Si interface or the deposition of amorphous Si (a-Si) between the metal and the Si substrate (without breaking vacuum!), a change of reaction kinetics from

an abrupt silicide formation at higher temperature (like [63]) to a layer-by-layer silicide formation at lower temperature is observed. The effect of ion implantation is believed to lead to the dispersion of interfacial contaminants (mainly Si or RE oxides), responsible for the threshold temperature and the abruptness of reaction typical of unimplanted samples. Regardless of the preparation method of the Si substrate, samples exposed to air before Er deposition always result in an abrupt reaction.

RE metals oxidize very quickly in air even at room temperature [63, 64], preventing the silicidation from occurring or giving a poor quality oxidized silicide. To avoid oxidation when vacuum is broken for annealing, Tu *et al.* [72] propose to cover REs with a bilayer of W and Pt, successively evaporated in one step. Pt is a very efficient barrier for oxygen diffusion and W prevents RE and Pt from intermixing [73]. For the first time, the authors extract the SBH of RE silicides (by I-V measurements) and find a value of 0.37-0.39 eV for n-type Si and 0.7 eV for p-type Si. These values are confirmed by [74] both by electrical and photoemission extractions.

The surface morphology of RE silicides grown by furnace annealing is found to be dominated by heavy pitting when the surface of the wafer is only prepared in normal pressure conditions [75], without further treatment in the deposition chamber. The pits are rectangular or square, suggesting that they are crystallographic by nature, reflecting the underlying symmetry of the Si(100) substrate. In the same conditions, the formation of pits is avoided when an a-Si layer is sandwiched between the Si substrate and the Er film. Furthermore, if the Si surface is treated under vacuum conditions (backside heating) prior to Er deposition or the Si-metal interface exposed to ion mixing to break up and disperse interfacial contaminants, the surface presents a low density of very shallow pits. According to the authors, interfacial contamination is the most likely hypothesis for the formation of pits. Since Si is known to be the main diffusing species in Er silicide formation [76], the pits result from a localized restriction of the Si flow during silicidation due to interfacial contaminants.

There is a close link between the pit formation and the sudden onset of rapid silicide growth at a critical temperature, both of them caused by the interfacial barrier. So long as this interfacial layer is not broken down, the silicidation is inhibited. Assuming the presence of an interfacial barrier, it is possible to relate the critical temperature to an activation energy for its dissolution [77]. Moreover, samples studied in that work are annealed by e-beam and exhibit a very smooth surface, smoother than that produced by furnace annealing.

This pitting is shown to be detrimental to the electrical properties of

Schottky diodes created with Er silicide [68]. More precisely, Wu *et al.* fabricate pitted (single Er deposition over Si) and unpitted (Er with an a-Si capping layer over Si) Er silicide films by solid-phase reaction and observe an increase of the SBH to holes ($q\Phi_{Bp}$) for planar films.

The nature of this interfacial barrier is firstly considered to be Si oxide only, but Knapp *et al.* [78] propose that it is more likely attributable to a carbon layer, since Si oxide is readily broken down by the highly reactive Er upon deposition. The cleaning technique might be at the origin of this supplementary layer [79]. In the best conditions, a SBH of 0.78 eV is obtained on *p*-type Si.

In two different papers [80, 81], Wu *et al.* investigate the formation of Er silicide under special conditions. In the first one [80], the effect on the SBH of the presence of a thin interfacial Si oxide film is studied. It is found that there is a correlation between the SBH and the presence of the thin oxide film. Samples with oxide exhibit a SBH to *p*-type Si of 0.68 eV while clean samples show a higher SBH of ∼0.8 eV. The authors also report the SBH of Er and Er silicide on oxide-free *p*-type Si to be identical (∼0.8 eV), suggesting that the stoechiometry of the metallic contact does not appear to affect the SBH, as long as a specific metal is present at the interface. In the second article [81], the presence of Ge in Er silicide and its effect on the SBH formation is explored. It is shown that the Ge/Er ratio in the formed Er-Si-Ge alloy affects the SBH in a significant way, indicating that the SBH of a metallic compound on Si also depends on the composition of the alloy, in addition to the dependence on the metallic species.

So far, only a few publications are devoted to the formation of epitaxial RE silicides, except for a few results reported in [63, 76]. In fact, epitaxial growth between Er silicide and Si(111) is possible since their lattice mismatch is very small [62]. Knapp *et al.* [62] demonstrate the formation of epitaxial RE silicides on Si(111) by fast e-beam heating. In another paper, they suggest the presence of Si vacancies organized in a superlattice [82], while Baglin *et al.* [63, 76] rather mention a random distribution of the vacant positions. As already noticed hereabove, the main difficulty with furnace annealed RE silicides is to get smooth silicide layers, unless special care is taken to prepare the Si surface.

After presenting many results regarding Er silicide, we focus now our attention to the growth of Y silicide by furnace annealing. In effect, the formation mechanism of pits and the solutions for producing silicide films with a good morphology is better documented for Y silicide with respect to Er silicide.

Gurvitch *et al.* [83] demonstrate that it is possible to produce one of the best epitaxial silicides with Y over Si(111) substrates, using sputter

deposition and high vacuum (HV) annealing. The grown films are apparently pinhole- and Si vacancy-free. The substrate cleaning method has outmost importance to reach epitaxial quality. A SBH of 0.36 eV is extracted from n-type wafers.

In a following thorough study, Siegal *et al.* [84] report about the growth of Y silicide over Si(111) in UHV by four different methods. Solid-phase epitaxy, reaction between a metal overlayer and the Si substrate, results in poor epitaxial quality and triangular pinholes. Reactive deposition at 300 °C (i.e. deposition on a heated substrate) with a Si capping improves the epitaxy but pinholes are still present. The situation worsens as the annealing temperature increases but both the epitaxial quality and the resistivity of the film improve. Reactive deposition with templates (i.e. a pre-formed thin Y silicide film) gives better epitaxial quality and lower pinhole density than reactive deposition with a Si capping. Despite the increased degree of structural order, the resistivity is higher. Combining reactive deposition to templates and a Si capping does not lead to any significant amelioration. In addition, the lowest pinhole areal coverage is shown to be obtained with the thinnest silicide film. Even though the authors do not succeed in suppressing the pinholes, they point out that the pinhole issue appears to have its roots in the initial reaction between Y an Si.

Pursuing their investigation on Y silicide, Siegal *et al.* [85] explain that, since the growth of Y silicide from Y overlayer is controlled by nucleation [63, 76], such a reaction invariably leads to the formation of pinholes. The only way to avoid the pinhole formation is to prevent the reaction between Y atoms and atoms from the Si substrate, in order to promote layer-by-layer growth instead of nucleation. Such conditions can be achieved by successive deposition of Y and Si in a stoechiometric ratio at room temperature. Indeed, the activation energy for the reaction between deposited Si and Y is lower than the nucleation one because of a lower interface free energy. When the deposition temperature is below the nucleation threshold (300 °C), the layer-by-layer growth is favored and pinhole-free films can be formed. Moreover, subsequent high temperature annealing, necessary to reach epitaxy, does not open pinholes.

Lee *et al.* [86] report the first observation of "solid-state amorphization" for RE metal/Si systems [87] i.e. the formation of a Si-rich amorphous silicide interlayer during the deposition of Y at low (room) temperature on Si. There exists a critical thickness for the amorphous intermixed layer, thickness beyond which the formation of crystalline phases starts. That critical thickness for the Y/Si couple turns out to be exceptionally high among all metal/Si systems.

After this long digression on the mechanisms of defect formation in Y silicide, we resume now our discussion about Er silicide. Using UHV codeposition of Er and Si (called "molecular beam epitaxy codeposition") followed by solid-phase reaction in a furnace, Arnaud d'Avitaya *et al.* [88] obtain pit-free films with a high epitaxial quality. The films are continuous and monocrystalline, and form a vacancy-rich hexagonal AlB_2-type lattice, as already observed several times here above. Duboz *et al.* [60] study the electrical properties of such thin epitaxial erbium silicide films. Low temperature resistivity measurements show that the resistivity decreases with temperature and tends to a limiting residual resistivity at low temperature (∼20 K), typical behavior of a crystalline semi-metallic material. The room temperature resistivity is found to be equal to 34 $\mu\Omega$cm. SBH measurements on p-type and n-type Si give SBHs of 0.74 and 0.28 eV, respectively (smaller than reported in [72]). The reason why the sum of $q\Phi_{Bn}$ and $q\Phi_{Bp}$ is not equal to the bandgap of Si is not explained.

In a similar but more complete study, Sagnes *et al.* [89] find that the residual resistivity strongly increases when the silicide thickness decreases, due to surface scattering. Using the transmission line method, the specific contact resistance of Er silicide on n-Si(100) (from 10^{18} to 10^{20} cm^{-3}) is found to be as low as 3.7×10^{-8} Ωcm^2 [90] (comparatively 10^4 lower than that for Al). The experimental data are also compatible with a SBH of 0.37 eV. It is shown that, upon annealing, ρ_c rapidly drops (within 2 min) and then remains independent on the anneal time (for a fixed annealing temperature). Identically, ρ_c is found to be independent on the anneal temperature (for a fixed annealing time).

Unewisse *et al.* [61] identify two kinds of silicides, obtained in very close conditions but at two slighlty different temperatures. At 410 °C, the barrier is equal to 0.28 eV and equal to 0.36 eV at 450 °C. These values are in agreement with the previously reported results. This SBH difference is likely related to the roughness of the silicide-Si interface: the smoother the interface, the lower the barrier.

Summarizing the previous results obtained for Φ_{Bn}, Muret *et al.* [91] clearly establish that the values are grouped around two distinct numbers: ∼0.38 [72, 74, 90] and ∼0.28 eV [60, 61]. When the preparation conditions and the morphologies of the samples studied in those articles are carefully analyzed, it appears that they cannot be correlated to the SBH. Very different preparation methods can result in very similar SBHs, or, conversely, very similar preparation conditions can give different SBHs. After growing Er silicide films in various conditions, the authors find no clear correlation with the SBH. In another paper by the same group [65], the authors show that there exists a correlation between

the SBH and the oxygen content into the silicide: a concentration lower than 0.3% is necessary to obtain a SBH of 0.28 eV. However, Grimaldi *et al.* [92] show that introducing a small amount of oxygen during Er deposition improves the crystalline quality of the silicide. The proposed explanation for that finding involves the incorporation of oxygen in substitutional position in the Si vacancies.

Kaltsas *et al.* [93] explore the epitaxial growth of erbium silicide on Si(100) in a more conventional evaporator operating under HV conditions. The films are prepared either by (1) Er deposition and annealing or (2) codeposition of Er and Si and *in situ* annealing. In case (1), the silicide film is found to present a high crystalline quality but exhibits rough interfaces. The films formed in case (2) are smooth and double-layered: polycrystalline at the surface and crystalline under. The codeposited samples exhibit a lower resistivity than the other ones, probably due to lower oxygen content in the silicide film. It is also observed that silicide in the neighbourhood of SiO_2 reduces oxygen from it with a consequent resistivity increase of the silicide. Conditions of case (1) lead to a SBH on *p*-type Si of 0.71 eV, lower than the one obtained for Er silicide grown by molecular beam epitaxy [60,88]. This may be correlated to a rough interface, as in [61]. The same group also shows that the phase of the silicide is tetragonal, of the $ThSi_2$-type (induced by the (100) orientation of the Si substrate), for samples prepared by single Er deposition [94] and an hexagonal/tetragonal mixture for samples prepared by codeposition of Si and Er [95]. Indeed, for the single Er deposition samples, the silicidation starts from the interface and so the influence of the substrate orientation is stronger. In a complementary work, Travlos *et al.* [96] show that the crystalline structure depends on several other parameters: the method of growth (single Er layer deposition, Si cap over Er or codeposition), the temperature of growth, the stoichiometry of the layer and, to a lesser degree, the stress developed in the layer during growth. Furthermore, the resistivity is found to be the smallest for the tetragonal phase ($\sim$70 $\mu\Omega$cm) (see also [97]).

In a series of papers [69, 98, 99], researchers add a supplementary ingredient ignored so far to the understanding of the defect formation in RE silicides, namely the solid-state amorphization. Luo *et al.* [98] study the growth kinetics of Er and Tb silicides. Identically to Y [86], they show that the Er/Tb silicide film is amorphous when the annealing temperature is low and the annealing time short enough. Upon higher temperature ($\leq$ 300 °C) and/or prolonged annealing, as the amorphous layer thickens, the diffusion flux becomes limited and isolated epitaxial regions start to nucleate at the interface to Si, between two amorphous regions, initiating a competitive growth between the amorphous and the

crystalline phases. The epitaxial regions act as diffusion barriers for Si, which diffuses then preferentially through the openings, progressively creating recess areas. This results in the formation of a high density of amorphous recess regions between two epitaxial ones. Finally, the growth of the amorphous phase slows down and the epitaxial islands can continue grow to form a continuous uneven epitaxial film. No pinholes are observed but the rough interface observed at relatively low annealing temperatures is a sign that annealing at higher temperature could cause pinhole formation. A similar behavior is observed for Gd silicide [99] except that the growth of epitaxial $GdSi_{2-x}$ is facilitated compared with $ErSi_{2-x}$ and $TbSi_{2-x}$ because of a smaller lattice mismatch. As result, unlike Er and Tb, the growth of the Gd-Si amorphous layer is suppressed with the onset of epitaxial $GdSi_{2-x}$ nucleation.

In a following paper [69], the same group pursues its investigation of RE silicide growth (with Dy) for higher annealing temperatures. Based on cross-sectional TEM (XTEM) pictures, they deduce a "Stranski-Krastanov" growth mode (layer-by-layer plus island growth) for Dy silicide i.e. epitaxial islands, where the Si consumption is greater, form between two planar epitaxial regions. This growth process is slightly different from the "Volmer-Weber" growth (i.e. growth by islands) typical of Er and Tb [98] at low temperatures. Due to the Stranski-Krastanov growth behavior, the epitaxial Dy silicide film presents a high density of recessed regions at the initial stage of the silicidation. When the growth is performed at higher temperature (700 °C), Dy silicide in the recessed regions evolves to a polycrystalline state, due to the bad lattice match in these curved regions. The polycrystalline nature of the recessed regions is beneficial to the diffusion of Si from the substrate along the grain boundaries towards the Er film. As a result, the recessed regions become deeper and larger with the annealing time. In the end, the silicide film in the recessed regions can break apart due to thermal instability and form pinholes. The solution proposed to obtain pinhole-free Dy silicide is thus to minimize the consumption of Si from the substrate by depositing an appropriate thickness of amorphous Si over the Er film (calculated taking into account the unavoidable formation of the amorphous interlayer after RE deposition). That Si capping layer is consumed during the silicidation instead of Si atoms from the bulk. In a further paper very similar to the previous one [66], the authors obtain pinhole-free epitaxial Yb and Er silicides on atomically clean Si(111) using the same method.

Alternately, Travlos *et al.* [100] propose a different mechanism for the formation of pinholes (with Dy). As already mentioned in the previous papers, a thin amorphous RE silicide film forms during the deposition of RE metals at room temperature because of solid-state amorphization.

At the initial stages of silicidation, Si diffuse through the amorphous interlayer to react with Dy, increasing the thickness of the a-layer. At the same time, a thin part of the a-layer in contact with Si crystallizes. Further Si diffusion increases the thickness of both the crystalline and amorphous layers. All of a sudden, both the silicide and the unreacted Dy layers lift off from the substrate in some places, probably because of intense stresses associated with volumetric changes during the silicide formation. Si can continue to diffuse through the regions still in contact with the substrate, which causes roughening of the interface because of a local depletion of Si under the lifted areas. When the Dy layer is completely consumed, stresses decrease and the silicide film can get back into contact with the Si substrate.

To prevent the pinhole formation, Tan *et al.* [67] successfully propose to amorphize the Si substrate (by Ar plasma clean or shallow Si implantation) prior to Er deposition. Er silicide formed on unamorphized Si present "hump-like" defects but are highly epitaxial. On the other hand, amorphized samples present no defect but Er silicide becomes polycrystalline. In a next paper [101], light is shed on the formation of above-mentioned "hump-like" defects. Unlike the pits that form under a local depletion of Si atoms [69, 98, 99], those pyramidal defects form under epitaxial strains arisen from the Er silicide growth. More specifically, during the silicide growth, the silicide film separates from the Si substrate to release compressive epitaxial stresses (similarly to [100]). Then Si can diffuse into the void left by the buckling of the silicide film, which gives the pyramid-like structures. This illustrates again that RE silicides are extremely sensitive to the crystallographic properties of the underlying substrate. In a third paper [102], the same authors argue that pre-amorphization of the Si substrate globally improves the electrical performance of Er-silicided Schottky diodes, causing at the same time a reduction of Φ_{Bn} and of the ideality factor.

Jiang *et al.* [71] produce pinhole-free Yb silicide films introducing a thin amorphous layer between the Si sustrate and the Yb film. The as-formed films are more polycrystalline than the one grown without the interlayer and are not contaminated by oxygen thanks to a Ti/TiN bi-capping [103]. The technique works even if the thickness of the Si layer is so small that silicidation still requires the consumption of Si atoms from the substrate, contrary to the Si capping method, requiring an accurate control of the Si thickness.

Huang *et al.* [104] perform the annealing of various Er thicknesses without capping in a very pure nitrogen atmosphere. They show that the type of defect formed depends on the thickness of the Er layer: pyramids are formed for thin layers and pinholes for thicker layers. Both

kinds of defects have a rectangular or square shape, reflecting the (100) orientation of the underlying Si substrate. Since the thinner films are strongly oxidized, the authors perform SBH extraction for thick samples only. They find that (i) the SBH varies with the annealing temperature, (ii) it is best fitted with a model taking SBH inhomogeneities into account, and (iii) it is comprised between 0.34 and 0.43 eV. Using a W capping layer, the same authors [105] obtain a very smooth, unoxidized Er silicide film, and extract a relatively low SBH of 0.41 eV. Contrary to Si deposition, both capping and interlayer methods, that technique presents the advantage to be compatible with device integration. In two almost identical articles [106, 107], Jun *et al.* observe a dependence of the SBH on the measurement temperature (at low temperature) and attribute it to trap-assisted tunneling.

Huda *et al.* [108] are the first authors to report the formation of Er silicide over a silicon-on-insulator (SOI) substrate. They show that the grown film is stable for an annealing temperature below 800 °C and extract a low SBH of 0.27 eV. In another study devoted to the Er silicide growth over SOI wafers, Kim *et al.* [109] show that the deposited Er thickness must be less than 1.5 times the Si thickness to fully silicide the Si film. If more, an Er-rich film forms between the silicide and the buried oxide which provokes the removal of the silicide during the stripping of unreacted Er.

The growth of germanides [110] and silico-germanides [111] is also investigated. In the first case [110], Er germanide is formed for annealing above 400 °C but the samples are heavily contaminated by oxygen if no precaution is taken. Growth in vacuum or with a Ti cap decreases but does not suppress the oxygen contamination and results in defect-free and low resistivity Er germanide films. The same observation can be made for the growth of Er silico-germanides [111].

In two separate papers [112, 113], Reckinger *et al.* investigate the SBH dependence on the annealing temperature of contacts between Er silicide and *n*-Si. The SBH is shown to decrease progressively with temperature increase to reach a minimal value of 0.28 eV. The SBH drop is associated to the formation of crystalline Er silicide [113]. On the other hand, the SBH is found to raise slightly if the annealing temperature is further increased [112]. This augmentation appears in correlation with an enhanced oxygen diffusion upon high temperature annealing.

3.3 Formation in ultrahigh vacuum conditions

Before investigating the growth of Er silicide with a protective capping layer, we process reference samples deposited and annealed in UHV, without breaking the vacuum between the two steps. The SBH extraction from such samples can serve as a calibration since the $ErSi_{2-x}$/Si contacts produced in UHV conditions result in a well-established SBH of 0.28 eV [60, 61].

3.3.1 Sample preparation

The initial bulk substrates are n-type lowly doped Si(100) wafers (phosphorus-doped with a resistivity of 5-10 Ωcm). The test structures for SBH measurement consist in two 1000 μm^2 square contacts separated by a micrometer gap defined by e-beam lithography to produce face-to-face diodes. To define the pattern, a negative tone e-beam resist called hydrogen silsesquioxane (HSQ) is used. After annealing, HSQ holds the remarkable property to evolve from a cage-like monomer to a network-like polymer that approaches the structure of Si dioxide (SiO_2). The thickness of the obtained oxide is 200 nm. Si pieces are also left bare for structural characterization.

First, the samples are cleaned in sulfuric peroxide mixture (SPM), mixture of sulfuric acid (H_2SO_4) and hydrogen peroxide (H_2O_2). After rinsing in de-ionized (DI) water, they are dipped into 1% hydrofluoric (HF) acid to remove the grown oxide, rinsed, and dried with N_2. The wafers are immediately inserted into the evaporation chamber, to limit oxide regrowth in ambient air. The deposition is performed in an e-beam evaporator operating under UHV (base pressure $\sim 5 \times 10^{-9}$ mbar). 20 nm of Er are deposited without breaking the vacuum. Then the samples are transferred to the adjacent annealing chamber, without breaking the vacuum and annealed during 1 hour at 500 and 600 °C, respectively. After cooling down to room temperature, the samples are unloaded and the unreacted Er is removed by SPM. The samples including face-to-face diodes are diced and wire-bonded for SBH determination.

3.3.2 Physical characterization

In order to evaluate the quality of the deposition, we display in Fig. 3.1 a high magnification micrograph for an as-deposited Er film covered with a protective 10 nm thick Ti layer. The Er and Ti thicknesses measured from Fig. 3.1 are found to be close to their respective initial target of 25 and 10 nm. It is also interesting to notice the presence of

a thin amorphous Er-Si (a-Er/Si) layer between the Er layer and the Si substrate. This intermixing of two metallic elements to form amorphous interlayers is the solid-state amorphization already evoked in section 3.2.

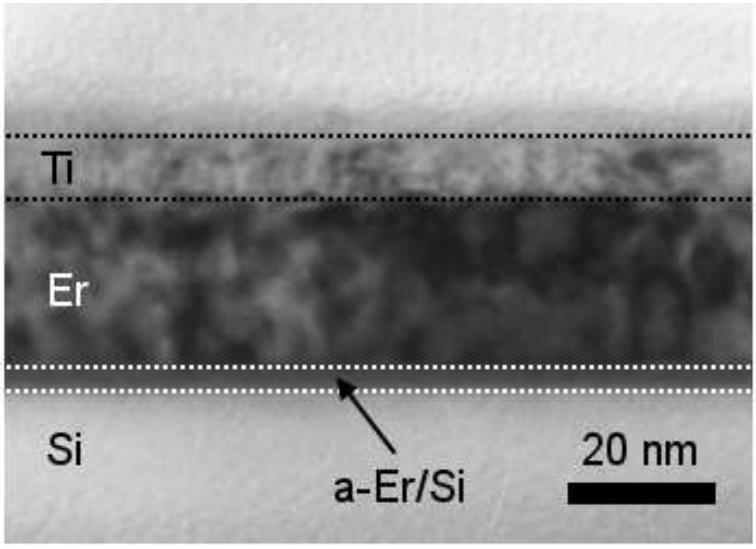

Figure 3.1: High magnification XTEM micrographs of an as-deposited Er film evaporated in UHV conditions and covered with a protective Ti layer.

The phases formed after annealing of Er in UHV at 600 °C are identified by θ-2θ XRD. Figure 3.2 presents the XRD spectra for the 600 °C sample before and after stripping, respectively. In both cases, we can observe the occurrence of a unique peak with very similar intensities located at $2\theta = 27.1°$. It corresponds to the 100 reflection of $ErSi_{2-x}$. This result confirms the formation of $ErSi_{2-x}$ along with the preservation of the $ErSi_{2-x}$ film after stripping.

The XTEM analyses featured in Fig. 3.3 lend support to the XRD conclusions. In Fig. 3.3(a), we can observe a residual Er layer of ∼4 nm on a 33 nm thick $ErSi_{2-x}$ film. The SPM stripping leaves the silicide film absolutely intact and removes Er nearly completely (see Fig. 3.3(b)). The interface between the $ErSi_{2-x}$ film and the Si substrate is very sharp and the $ErSi_{2-x}$ film is very homogeneous in thickness and regular.

Scanning electron microscopy (SEM) overviews of the surface of the $ErSi_{2-x}$ film exhibit pyramidal defects with a square base and the apex in the Si substrate (see Fig. 3.4(a)). The typical concentration of these

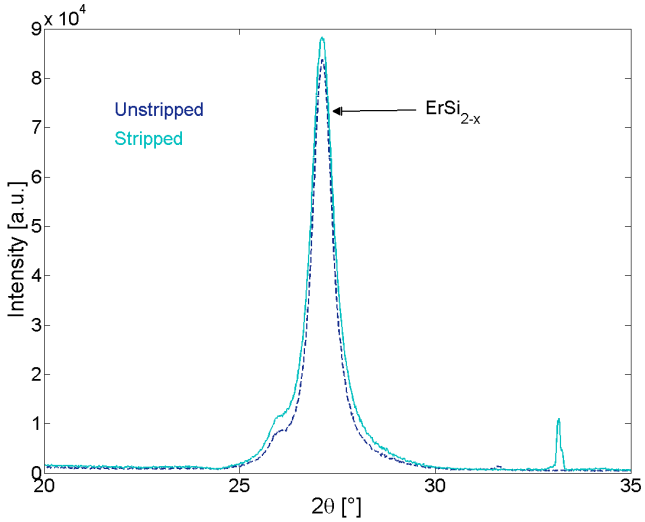

Figure 3.2: XRD spectra for $ErSi_{2-x}$ grown in UHV at 600 °C before and after stripping of unreacted Er. A nearly identical intense $ErSi_{2-x}$(100) peak can be observed in both cases.

defects amounts to $\sim 10^5$ cm^{-2} [101]. As we can see in Fig. 3.4(b) which focuses on one of the reversed pyramids, their typical size is in the micrometer range. Figure 3.4(c) reveals a high magnification scan of the $ErSi_{2-x}$ surface which shows some apparent superficial roughness.

XPS depth profiling is performed to investigate the composition of the $ErSi_{2-x}$ film. Core level spectra are recorded for erbium (Er $4d$), oxygen (O $1s$), and silicon (Si $2s$). The XPS analyses are performed with a Physical Electronics 5600 spectrometer fitted in an UHV chamber (base pressure $\sim 10^{-10}$ mbar). We use a monochromatized Al x-ray source (hν = 1486.6 eV) and the detection angle is 45° with respect to the sample surface normal. Depth profile analysis is realized by sputtering using an Ar^+ ion gun operated at 1 keV with a beam raster of 5×5 mm^2. The pass energy is set to 47 eV for depth profiles and 23 eV for more resolved spectra, leading to overall resolutions as measured from the full width at half-maximum of Ag $3d_{5/2}$ about 0.9 and 0.7 eV, respectively. Figure 3.5 exposes the corresponding intensity profiles for Er $4d$, O $1s$, and Si $2s$. The depth profile discloses that oxygen is confined to the very surface of the silicide film. This oxygen could originate from ambient air during the transfer to the XPS analysis chamber. The ratio between the Er $4d$ and Si $2s$ signals is constant, testifying to an homogeneous chemical

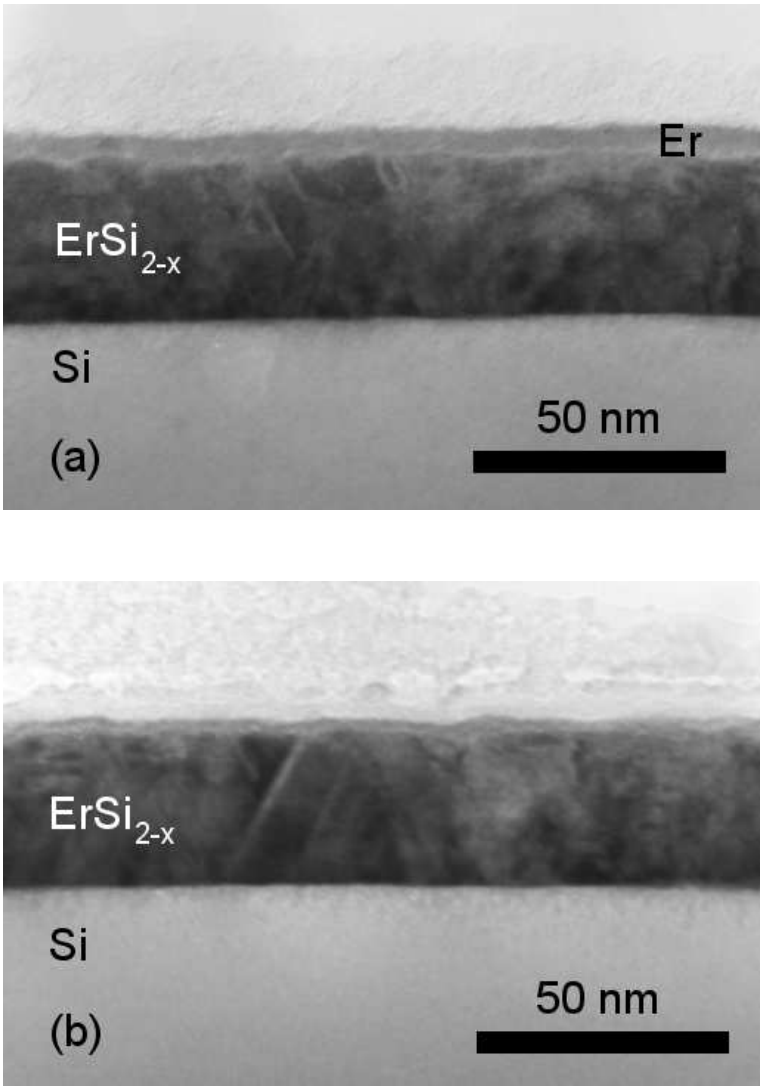

Figure 3.3: XTEM micrographs of $ErSi_{2-x}$ grown in UHV at 600 °C (a) before and (b) after stripping of unreacted Er.

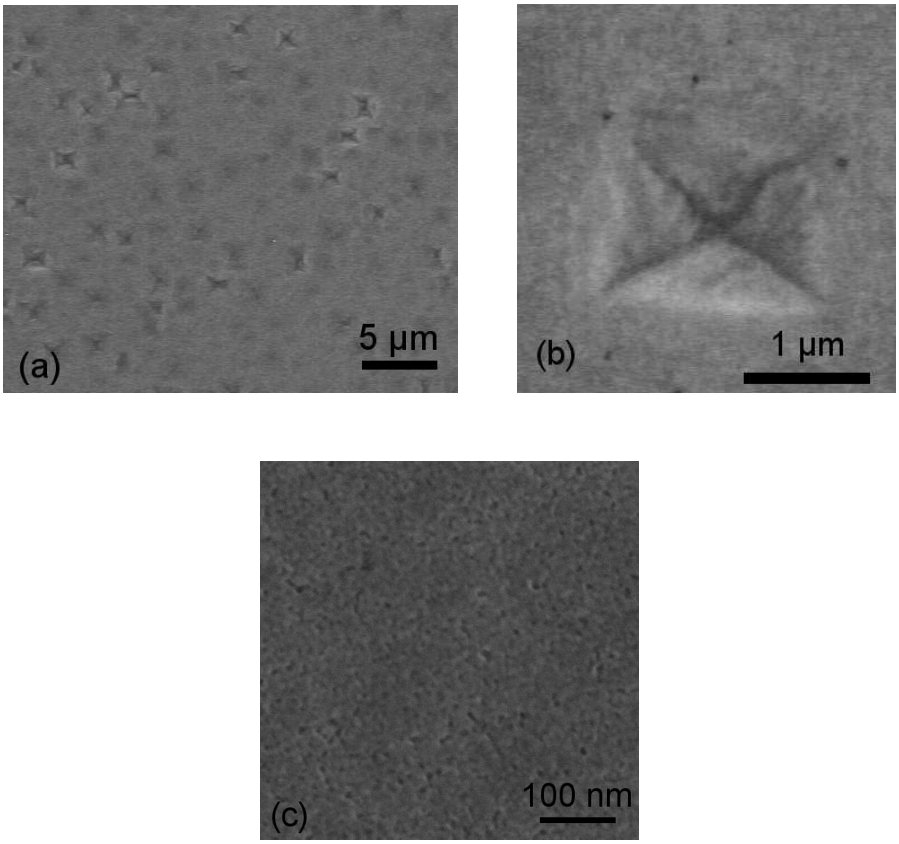

Figure 3.4: SEM pictures of the surface of $ErSi_{2-x}$ grown in UHV at 600 °C after stripping: (a) many pyramidal defects are observed at small magnification, (b) zoom on one of these defects, and (c) high magnification scan of the $ErSi_{2-x}$ surface.

composition.

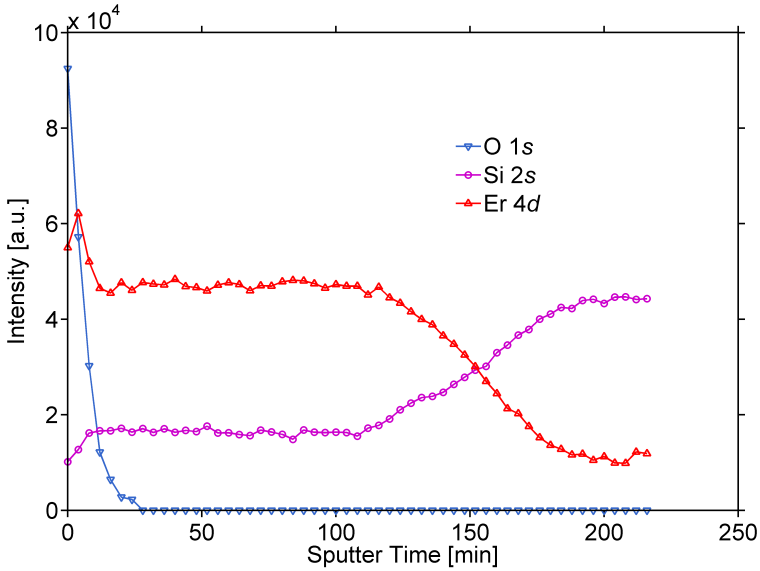

Figure 3.5: XPS intensity depth profiles of $ErSi_{2-x}$ grown in UHV at 600 °C.

3.3.3 Electrical characterization

Figure 3.6 exhibits the Arrhenius plots for $ErSi_{2-x}$ grown in UHV at 500 and 600 °C, respectively. In addition to the experimental data represented by red squares (500 °C) or black circles (600 °C), the fit for 600 °C is also displayed. The *I-V* measurements are performed between 150 and 290 K with a step of 20 K. The selected V_{4C} biases range from 0.1 up to 1 V with a step of 0.15 V. The experimental data are fitted with the TFE+BL model. The corresponding SBHs are determined to be equal to 0.3 (500 °C) and 0.295 eV (600 °C), respectively. These values are in good agreement with the state-of-the-art value of 0.28 eV.

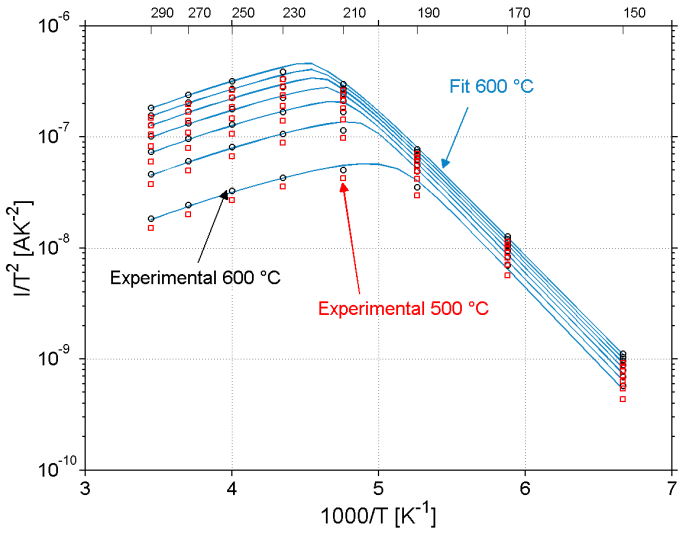

Figure 3.6: Arrhenius plots of $ErSi_{2-x}$ grown in UHV at 500 and 600 °C, respectively.

3.4 Formation with a Ti cap by *ex situ* annealing

Compared with growth in UHV conditions, the capping layer approach is interesting since it would considerably simplify the integration of RE silicides in an industrial CMOS process. A few authors have investigated the formation of RE silicides with a capping layer, for instance, Pt/W/Er [72], Pt/Si/Er [90], Si/Er [114], Mo/Er [98], Pt/Er [115], Ti/TiN/Yb [103], or W/Er [105]. In the perspective of RE silicide integration, the question of the removal of the sacrificial protecting layer must be taken into account. In the case of Pt, aqua regia is the only known stripping recipe. However, RE silicides are easily removed in a solution containing halogen ions [116]. Second, Pt mixes with RE metals even at 300 °C [73]. A Si capping layer is also incompatible with modern CMOS technology since the silicidation is performed all over the wafer, creating a single silicide layer that short-circuits all devices. W proves to be efficient to prevent oxidation but diffuses through the stack during the silicidation [105], which could have a negative impact on the SBH. On the opposite, Ti is a good candidate to serve as capping layer, since it is readily removed in SPM and does not mix with REs even at 800 °C [73].

3.4.1 Evaporation in ultrahigh vacuum conditions

In the present section, we investigate the efficiency of the capping layer technique to yield a low SBH with Er silicide grown over n-Si. More specifically, we explore the formation of Er silicide for Er evaporated in UHV conditions and covered with a thin Ti capping layer. The annealing is performed *ex situ* on a wide temperature range. The SBH is extracted for all considered annealing temperature, in correlation with physical characterization by XRD, TEM, and XPS.

3.4.1.1 Sample preparation

The initial bulk substrates are the same as previously written. First, they are cleaned in SPM. After rinsing in DI water, they are dipped into 1% HF acid to remove the grown oxide, rinsed, and dried with N_2. A Ni mechanical mask fixed on the wafers is used to pattern face-to-face Schottky diodes for SBH extraction. The wafers are immediately inserted into the evaporation chamber. The deposition is performed in the same e-beam evaporator operating under UHV conditions. 25 nm of Er and 10 nm of Ti are successively deposited without breaking the vacuum. Samples are also deposited without the protective Ti layer. The wafers are then brought to ambient conditions, transferred to an *ex situ* rapid thermal annealing (RTA) system and thermally activated in forming gas (95% N_2 + 5% H_2) for 2 min, from 300 to 600 °C with a step of 50 °C. One sample is left unannealed. The samples including diodes are diced and wire-bonded for SBH determination. The capping layer is not stripped to protect the surface of the silicide film and to facilitate bonding.

3.4.1.2 Schottky barrier height extraction

The SBH extraction is performed using I-V measurements at temperatures ranging from 150 to 290 K with a step of 20 K. The selected V_{4C} voltages range from 0.1 up to 1 V with a step of 0.15 V. The experimental data are fitted with the TFE+BL model. Figure 3.7 displays the dependence of the SBH on the annealing temperature. For the as-deposited sample, the extracted SBH amounts to 0.43 eV. After annealing at 300 °C, the SBH drops to 0.37 eV and is again substantially reduced to reach 0.28 eV upon annealing at 450 °C. Beyond that value, the SBH slightly increases. The remainder of this section is devoted to the explanation of the SBH dependence on the annealing temperature exhibited in Fig. 3.7, distinguishing two annealing temperature regions: below and above 450 °C).

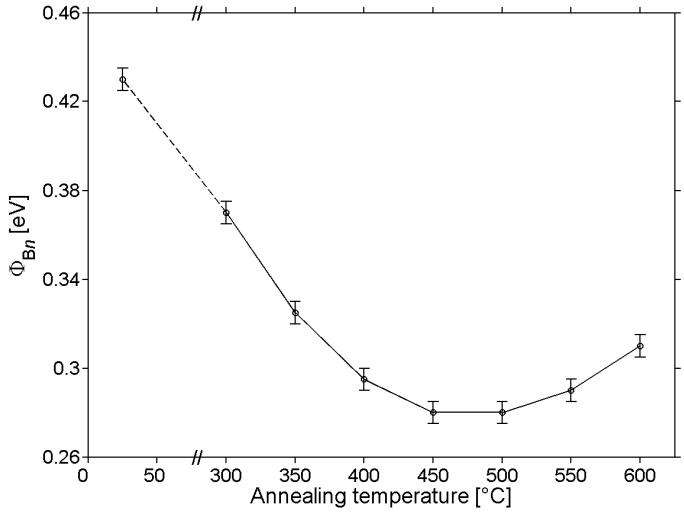

Figure 3.7: SBH of capped Er silicide contacts to n-Si as a function of the annealing temperature for the as-deposited sample and for the samples annealed between 300 and 600 °C with a step of 50 °C.

3.4.1.3 Low annealing temperature region

To emphasize further the strong impact of the annealing temperature on the electrical characteristics of the grown Er silicide film, we illustrate in Fig. 3.8 the evolution of the experimental Arrhenius plot for the as-deposited, 300, and 450 °C samples, respectively. We can observe that the transition temperature between the ohmic regime (positive slope in the Arrhenius plot) and the Schottky regime (negative slope in the Arrhenius plot) lowers with the annealing temperature, sign that the SBH decreases accordingly.

The formed phases are identified by θ-2θ XRD. Figure 3.9 presents the XRD spectra for the as-deposited, 300, and 450 °C samples, respectively. For the as-deposited sample, the intense peak registered at $2\theta = 32°$ matches the (002) peak of hexagonal Er. At 300 °C, the Er(002) peak disappears and a dominant peak at $2\theta = 30.4°$ ($d = 2.96$ Å) is now recorded. This peak does not belong to the diffraction pattern of body-centered cubic (BCC) Er sesquioxide (Er_2O_3). A similar peak ($d = 2.95$ Å) was previously reported for incompletely oxidized Er films [117, 118], with a lower oxygen content than Er_2O_3 (denoted ErO_x, with $x < 1.5$). At 350 °C, three peaks of similar intensities are detected. These peaks can all be related to Er compounds. The peak at $2\theta = 27.1°$ can be asso-

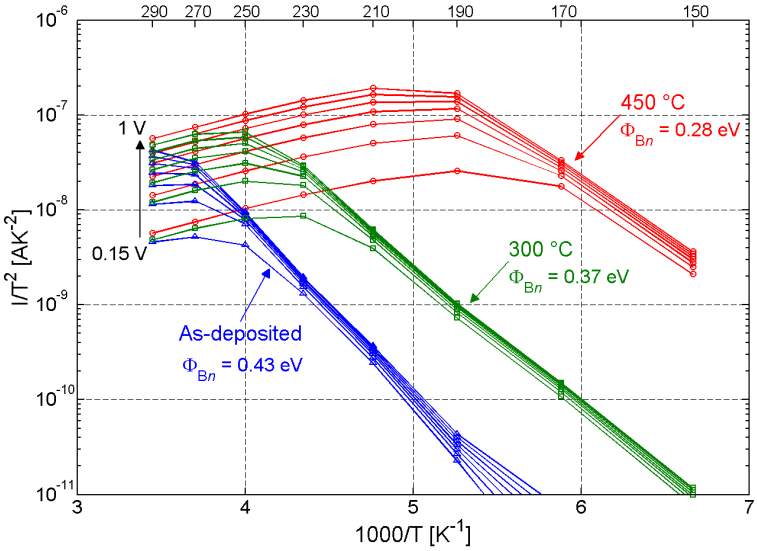

Figure 3.8: Arrhenius plots for the as-deposited, 300, and 450 °C samples, respectively.

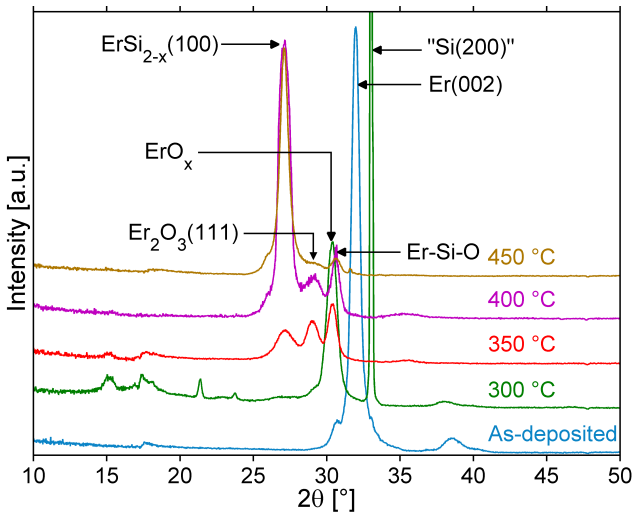

Figure 3.9: XRD spectra for the as-deposited sample and for the samples annealed between 300 and 450 °C with a step of 50 °C.

ciated to the (100) peak of hexagonal $ErSi_{2-x}$. In addition to the peak of ErO_x, another one appears (at $2\theta = 29°$), which is relevant to the (222) peak of BCC Er_2O_3. In consequence, we can infer that Er atoms in close contact to Si preferentially react with Si, while upper Er layers rather react with oxygen to form ErO_x and Er_2O_3. Indeed, some residual oxygen present in the annealing atmosphere can diffuse through the Ti cap during the thermal treatment and react with Er. When the annealing temperature is incremented to 400 °C, the $ErSi_{2-x}$(100) peak becomes dominant. More precisely, the intensity ratio between the $ErSi_{2-x}$(100) and BCC Er_2O_3(222) peaks is drastically increased, showing that the silicidation is now preponderant. Moreover, the ErO_x peak is replaced by a new peak at $2\theta = 30.7°$. This peak does neither belong to the diffraction patterns of hexagonal $ErSi_{2-x}$ or Er_2O_3. That peak could be relevant to a mixture phase of Er, Si, and O (Er pyrosilicate [111] or Er-Si-O [67]). More specifically, since Si is known to be the main diffusing species during the growth of $ErSi_{2-x}$ [76], it is likely to diffuse to the top region of the Er layer where it is also in presence with oxygen diffusing through the Ti cap. This results in the formation of a layer containing Er, Si, and O above $ErSi_{2-x}$. At 450 °C, the $ErSi_{2-x}$(100) peak prevails, with small amounts of Er-Si-O and Er_2O_3.

With the aim of better understanding the SBH dependence on the annealing temperature, we inspect the MS interface by TEM. Figures 3.10(a)-3.10(c) display XTEM images of samples annealed at 300, 350, and 400 °C, respectively. We can see that crystalline $ErSi_{2-x}$ forms at the interface with Si (hardly visible at 300 °C). That layer clearly thickens with the annealing temperature. In addition, Figs. 3.11(a)-3.11(c) exhibit HRTEM micrographs of the samples considered in Fig. 3.8. In Fig. 3.11(a), the thin interfacial film already discovered between Er and Si in Fig. 3.1 is measured to be ∼3 nm thick. At 300 °C (Fig. 3.11(b)), we can see that the intermixed a-Er/Si layer continues to grow, reaching a thickness of approximately 12 nm. Simultaneously, crystalline $ErSi_{2-x}$ islands start to nucleate at the MS interface [98]. On the other hand, Er completely reacts with Si to form a crystalline $ErSi_{2-x}$ film at 450 °C (Fig. 3.11(c)), as already revealed by the XRD measurements. From that analysis, it results that upon increasing annealing temperature, the Er-Si alloy progressively evolves from an amorphous state of undetermined composition to a crystalline one with the $ErSi_{2-x}$ phase. Since the SBH decreases accordingly, we may believe that there is a correlation between the SBH lowering and the formation of crystalline $ErSi_{2-x}$.

Very few research groups have investigated the parameters that influence the SBH of RE silicides. One study in particular provides some evidence for a correlation between the oxygen content in the silicide and

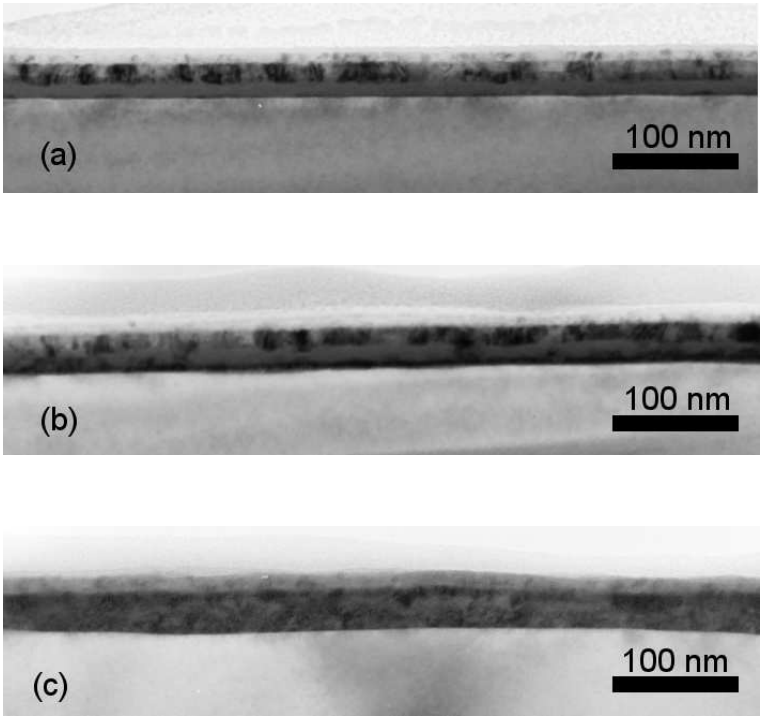

Figure 3.10: XTEM micrographs of the (a) 300, (b) 350, and (c) 400 °C samples, respectively.

the SBH [65]. To further reinforce our previous assertion, the possible oxygen contamination of the MS interface must be examined. To do so, changes of chemical composition are explored by XPS depth profiles. We focus on the as-deposited and 300 °C samples[1]. They are both introduced in the analysis chamber immediately after the evaporation to avoid oxidation in ambient air. Core level spectra are recorded for erbium (Er $4d$), oxygen (O $1s$), silicon (Si $2s$), and titanium (Ti $2p$). Figures 3.12(a) and 3.12(b) display the corresponding Er $4d$, O $1s$, and Si $2s$ intensity profiles, whereas Ti $2p$ is omitted for clarity. Figure 3.12(c) illustrates the evolution of the Er $4d$ and Si $2s$ BEs versus the sputter time (ST). Labels (capital letters) are used to mark specific positions in the stack.

From Fig. 3.12(a), it is disclosed that only the top of the Er layer is contaminated by a small amount of oxygen. Starting from marker

[1]The interface of the 450 °C sample, considered in section 3.4.1.4, will prove to be oxygen-free.

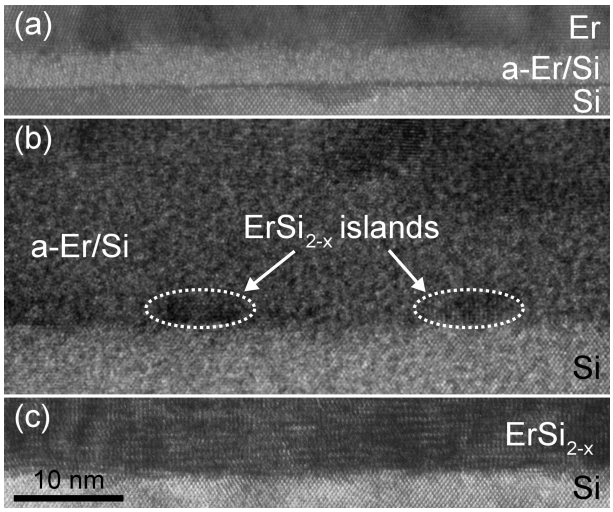

Figure 3.11: HRTEM micrographs of the MS interface for the (a) as-deposited, (b) 300, and (c) 450 °C samples, respectively.

A (ST = 40 min), the typical Er 4*d* BE is equal to 167.1 eV, relevant to metallic Er. Above marker A, no oxygen can be detected, within the experimental accuracy. Si appears at marker B (ST = 84 min), as indicated by a corresponding Si 2*s* BE of 149.5 eV. Since this BE is not relevant to elemental Si (Si 2*s* BE = 150.5-150.6 eV), it clearly suggests that a small part of the Er film is alloyed to Si, what is supported by the previous HRTEM pictures. Such a large Si 2*s* shift of ∼1.1 eV is comparable to the Si 2*p* shift noticed for an a-Er/Si mixture where Si atoms are more diluted into Er than in $ErSi_{2-x}$ [119, 120]. In addition, the Er 4*d* BE is found out to slightly shift towards 167.3 eV at marker B. Since it coincides with the detection of Si, it might be a supplementary signature of the Er-Si alloying.

At 300 °C (Fig. 3.12(b)), we can see that oxygen penetrates deeply into the sample. Roughly, between markers A' (ST = 64 min) and B' (ST = 124 min), Er is oxidized (Er 4*d* BE = 169.5 eV), corresponding to the ErO_x layer revealed by the XRD data. The layer located between positions B' and C' (ST = 176 min) is essentially composed of a mixture of Er silicide and Er oxide, with a decreasing proportion of Er oxide. Oxygen disappears at marker C'. After that position, the Si 2*s* BE progressively shifts towards the peak relevant to elemental Si, reached in D' (ST = 220 min) (see Fig. 3.12(c)), which position marks the interface with the Si substrate. Concomitantly, the typical Er 4*d* BE amounts

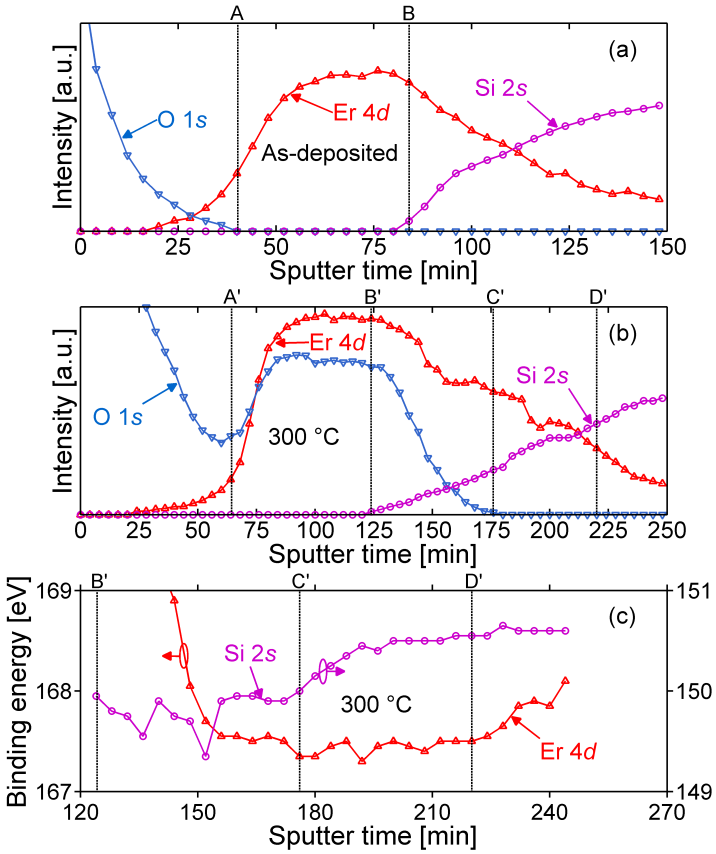

Figure 3.12: XPS depth intensity profiles for the (a) as-deposited and (b) 300 °C samples. (c) Er 4*d* and Si 2*s* BEs versus ST for the 300 °C sample.

to 167.4 eV and starts to differ beyond D'. The layer between C' and D' can be very likely assimilated to the a-Er/Si layer with crystalline $ErSi_{2-x}$ inclusions disclosed by HRTEM in Fig. 3.11(b). In any case, it is established that the respective MS interfaces of the as-deposited and 300 °C samples are both oxygen-free, within the experimental accuracy.

3.4.1.4 High annealing temperature region

3.4.1.4.1 Uncapped Er on *n*-Si Figure 3.13(a) shows a low magnification SEM picture of the surface for the uncapped sample annealed at 450 °C. In this image, many defects of various sizes can be observed. Figure 3.13(b) illustrates a zoom on one of these defects. This volcano-

like feature is very similar to the crack-like features in Er germanide reported by Liew *et al.* [110] for whom the formation of those cracks could be associated to the release of stress induced by the formation of Er oxide. Typical dimensions for those volcanoes range from 0.5 to 15 μm. In the central part of the volcano, the stress is so important that the surface is completely dislocated. At the periphery, the surface visibly underwent some stress, as it appears buckled, but the stress was not high enough to break apart the layer.

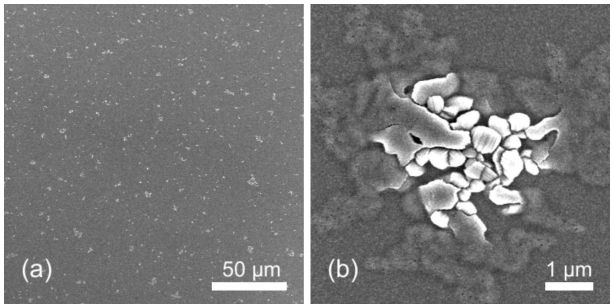

Figure 3.13: (a) Low magnification SEM picture of the surface of the uncapped sample annealed at 450 °C: the surface is scattered with many defects. (b) Focus on one of those defects.

Whatever the annealing temperature, the surface of the wafer is found to be nonuniformly silicided. Er is likely to oxidize when exposed to air before the annealing or/and during the annealing due to the presence of residual O_2 in the RTA chamber. In Fig. 3.14, results of XTEM analysis performed for a silicided area of the sample annealed at 600 °C confirm that the $ErSi_{2-x}$ film is very irregular, most likely heavily oxidized.

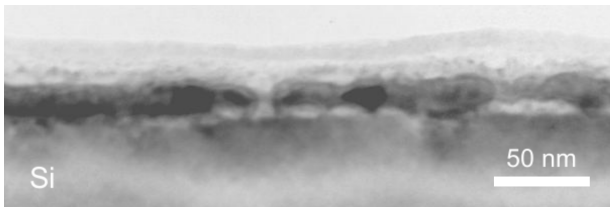

Figure 3.14: XTEM micrograph for the uncapped sample annealed at 600 °C.

3.4.1.4.2 Ti-capped Er on *n*-Si The necessity of a protecting layer to prevent oxidation during annealing has been illustrated by the poor quality of $ErSi_{2-x}$ films grown without capping. In order to avoid oxidation during *ex situ* annealing, a Ti layer is deposited over Er. To identify the formed compounds and to confirm the formation of $ErSi_{2-x}$, θ-2θ XRD analyses are performed for each annealing temperature, as exhibited in Fig. 3.15. A very intense $ErSi_{2-x}(100)$ peak is detected for all samples. The observation of such a strong peak is indicative of the formation of either highly textured or epitaxial $ErSi_{2-x}$ thin films, with an orientation relation of the type $ErSi_{2-x}(100)//Si(100)$. Another peak (at $2\theta = 30.6°$) is also disclosed for all annealing temperatures. As argued before, this peak is most likely relevant to Er-Si-O compounds. It is worth noting that the capping layer is not detected, probably because it is amorphous or too thin. Moreover, contrary to a recent publication [71], we do not observe the presence of diffraction peaks which could be related to Ti-Si phases.

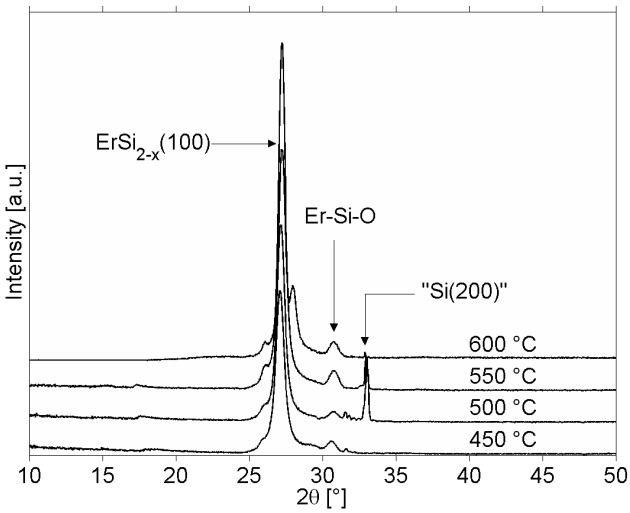

Figure 3.15: XRD spectra for the capped samples annealed at 450, 500, 550, and 600 °C, respectively. An intense $ErSi_{2-x}(100)$ peak can be observed for all annealing temperatures.

To further investigate the transformations of the Ti/Er/Si stack upon thermal annealing, we perform XTEM analyses. Figures 3.16(a)-3.16(d) exhibit low magnification XTEM micrographs of samples annealed by RTA at 450, 500, 550, and 600 °C, respectively (without cap strip-

ping). These images provide information on the global morphology of the $ErSi_{2-x}$ films. The $ErSi_{2-x}$/Si interface is found to be remarkably sharp in all cases. This result agrees with Chen *et al.* [121], showing that RTA eliminates interface roughness often observed for Er silicides formed in furnace. Besides, the capping layer remains intact and is visibly not mixed with Er during the annealing. No pits are observed in the $ErSi_{2-x}$ film, what could be due to the presence of the capping layer. Recently, Huang *et al.* [105] have indeed shown that capping layers can improve the morphology of $ErSi_{2-x}$ thin films.

Figures 3.17(a) and 3.17(b) present higher magnification micrographs for the samples annealed at 450 and 600 °C, respectively. From these figures, it clearly appears that the stacks resulting from annealing at 450 and 600 °C are divided into three distinct layers: the capping layer on the top, an intermediate layer of unknown composition, and finally the $ErSi_{2-x}$ one. Even though the exact composition of the intermediate layer is not known, it is likely mainly composed of Er atoms since the capping layer and the Er layer do not mix. It probably corresponds to the XRD peak identified as Er-Si-O.

XRD and XTEM analyses allow to evidence that the Ti/Er/Si stack is transformed into three distinct layers after annealing: (i) the capping layer mainly containing Ti, (ii) the intermediate layer possibly consisting of an Er-Si-O alloy and (iii) the bottom one composed of $ErSi_{2-x}$. In order to reveal the nature of the second layer and to investigate the modifications of the chemical composition in the stack after thermal treatment, XPS depth profiling is performed. Core level spectra are recorded from nitrogen (N 1s), titanium (Ti 2p), oxygen (O 1s), erbium (Er 4d), and silicon (Si 2s). The depth profile analysis is achieved by sputtering using an Ar^+ ion gun operated at 2 keV with a beam raster of 2×2 mm[22].

Figure 3.18 exhibits the atomic concentration depth profile of the Ti/Er/Si stack annealed at 450 °C. Figure 3.19 displays the corresponding core level spectra for N 1s, Ti 2p, O 1s, Er 4d, and Si 2s, respectively. For each element, we limit the plot to their zone of interest. To facilitate the discussion, we use different markers to locate specific positions in Figs. 3.18 and 3.19.

The Ti 2p signal can be found down to a depth corresponding to ST = 6 min. The top surface of the capping layer (marker A) is essentially composed of Ti dioxide (TiO_2), as indicated by the BEs of the Ti $2p_{3/2}$ (458.4 eV) and O 1s (530.1 eV) peaks [122]. A small nitrogen amount

[2]It is worth noting that the XPS equipment used here differs from the one used in sections 3.4.1.4, 3.3.2, and 3.4.2.1.

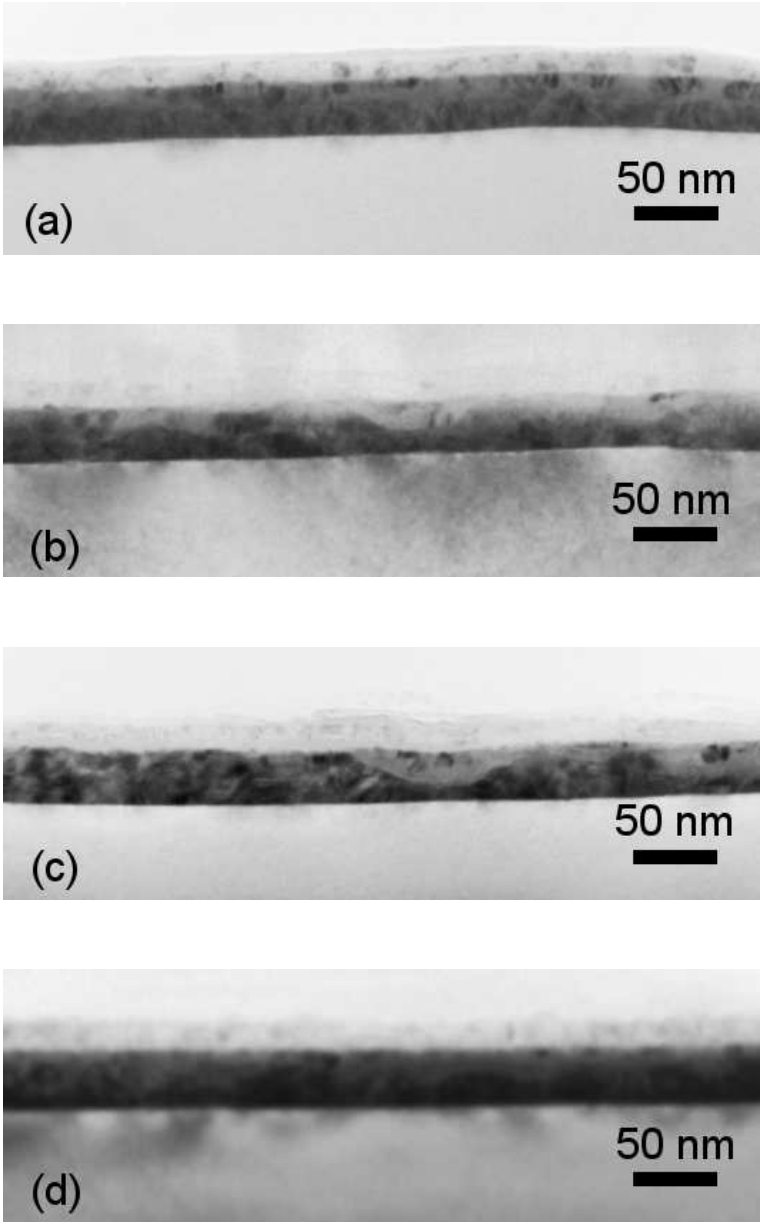

Figure 3.16: Low magnification XTEM micrographs of capped samples annealed at (a) 450, (b) 500, (c) 550, and (d) 600 °C, respectively.

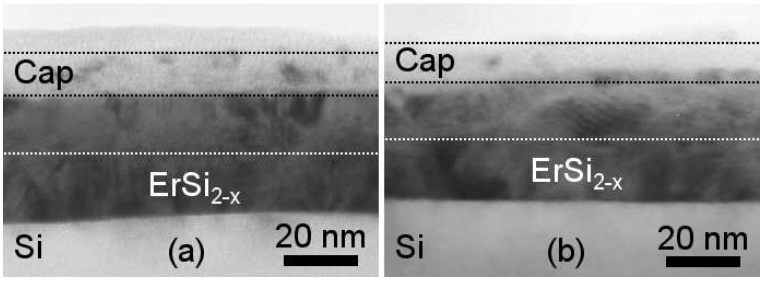

Figure 3.17: High magnification XTEM micrographs of capped samples annealed at (a) 450 and (b) 600 °C, respectively.

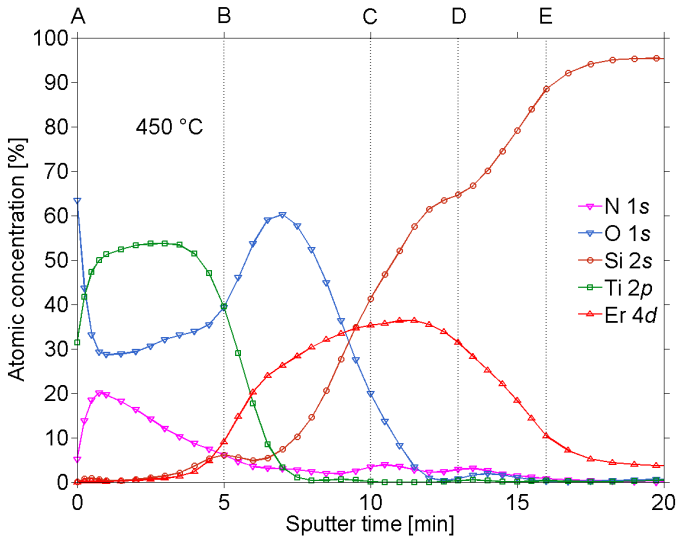

Figure 3.18: XPS atomic concentration depth profile of the capped sample annealed at 450 °C. The markers A to E indicate specific positions along the profile.

(about 10% in atomic concentration) is also present at this place. The corresponding N 1*s* peak of 397.1 eV is relevant to TiN_x [123]. Just below the surface, at ST = 0.5 min, the Ti $2p_{3/2}$ peak is shifted to a BE of 455.3 eV while the O 1*s* peak is shifted to 531.4 eV, revealing a strong change of chemical composition. Indeed, an O 1*s* peak of 531.4 eV is no more relevant to TiO_2 but rather to the TiO suboxide [124].

Within the subsurface region of the capping layer (between 0.5 and 5 min (marker B)), the characteristic BE of N 1*s* shifts from 397.1 to 397.8

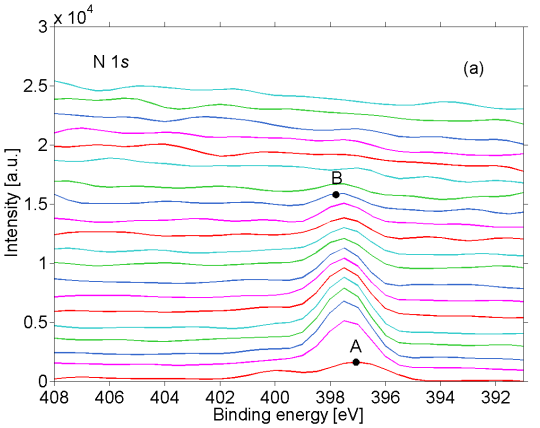
x 10^4
N 1s
(a)
B
A
Intensity [a.u.]
Binding energy [eV]
408 406 404 402 400 398 396 394 392
0 0.5 1 1.5 2 2.5 3

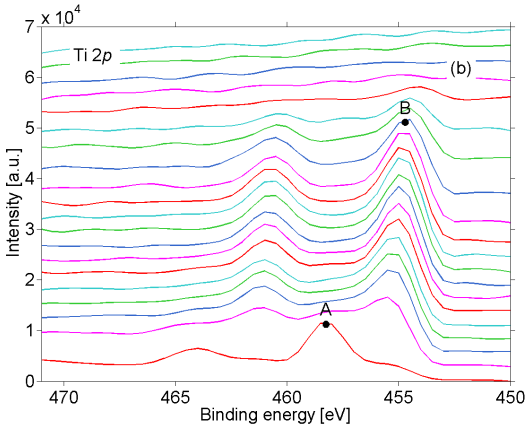
x 10^4
Ti 2p
(b)
B
A
Intensity [a.u.]
Binding energy [eV]
470 465 460 455 450
0 1 2 3 4 5 6 7

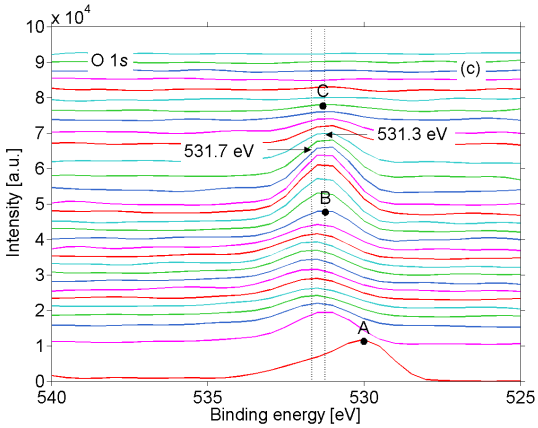
x 10^4
O 1s
(c)
C
531.7 eV
531.3 eV
B
A
Intensity [a.u.]
Binding energy [eV]
540 535 530 525
0 1 2 3 4 5 6 7 8 9 10

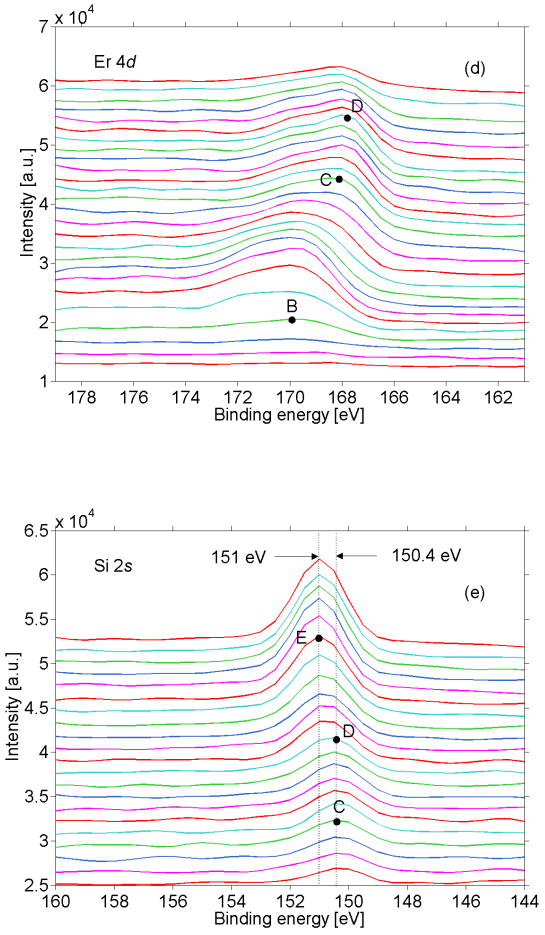

Figure 3.19: Series of spectra for capped Er silicide annealed at 450 °C corresponding to the core level spectra of (a) N 1*s*, (b) Ti 2*p*, (c) O 1*s*, (d) Er 4*d*, and (e) Si 2*s*, respectively.

eV, indicative of a progressive decrease of the nitrogen concentration in a TiN_x alloy [123], as also confirmed by the progressively decreasing atomic concentration. Simultaneously, the Ti $2p_{3/2}$ BEs are comprised between 455.3 (0.5 min) and 454.7 eV (5 min). The peak of O 1*s* remains centered around 531.7 eV. It results that the capping layer after annealing can be characterized by a TiO_xN_y composition. The Ti concentration is almost constant while the oxygen and nitrogen concentrations are respectively increasing and decreasing with depth. It is worth noting here

that nitrogen is only found in the capping layer.

Between 5 and 6 min, the presence of Er is detected with a peak of 170 eV while the peak of oxygen is shifted to 531.3 eV. Both these BEs correspond to Er oxide [125]. The ST of 5 min clearly marks the frontier between the cap and the Er layer.

The layer comprised between 5 and 7 min is mainly composed of Er oxide [3]. In that layer, oxygen is indeed characterized by a peak of 531.3 eV. From 8 min, the presence of Si is detected with a BE characteristic of $ErSi_{2-x}$ (150.4 eV). The Er $4d_{5/2}$ peak progressively shifts from 169.6 (8 min) to 168.4 eV (10 min), towards the typical peak of $ErSi_{2-x}$ [125], indicating that the proportion of $ErSi_{2-x}$ increases comparatively to Er oxide. The layer comprised between ST = 5 and 10 min (marker C) is thus a mixture of Er oxide and $ErSi_{2-x}$ with a progressively decreasing amount of Er oxide. That layer likely corresponds to the intermediate layer observed by XTEM and revealed by the peak at $2\theta = 30.6°$ in the XRD data. The previous results indicate that it seems to be composed of a mixture of Er, Si and O.

We can consider that the $ErSi_{2-x}$ layer properly speaking begins at ST = 10 min (marker C). A small amount of oxygen is found at the top of the silicided film. From ST = 11 min, the oxygen signal escapes detection. The layer between 11 and 13 min (marker D) is composed of pure $ErSi_{2-x}$ (with Er $4d_{5/2}$ and Si $2s$ peaks of 167.8 and 150.4 eV, respectively). At 13.5 min, the Si $2s$ BE starts to progressively shift to the peak of elemental Si (151 eV), meaning that the Si bulk is close to that position. The characteristic energy of elemental Si is registered after 16 min (marker E). It is worth noting here that, even if Er appears in the depth profile after 13 min, there is no more $ErSi_{2-x}$, since the Si $2s$ peak begins to shift to 151 eV. We believe that some Er is redeposited and even buried into the Si substrate during the sputtering process.

It is worth commenting here that it is in fact relatively difficult to precisely determine by XPS where the frontier between the intermediate layer and the $ErSi_{2-x}$ layer is located since there might be some Er redeposition on the substrate during the sputtering procedure. XTEM is much a more appropriate tool for that purpose. It appears nonetheless clear that there is a succession of three layers of different compositions but their respective location in the XPS profile must be considered as approximative. This illustrates the necessity of correlating the results of different complementary investigation methods like XTEM, XRD, and XPS to get a good overall picture of the transformations that the stack undergoes during the heating.

[3] It is a generic term regrouping ErO_x and Er_2O_3.

Figure 3.20 exposes the atomic concentration depth profile of the Ti/Er/Si stack annealed at 600 °C. A very similar analysis can be made for this sample, except for a few clear differences. First, we find out that oxygen penetrates deeper into the stack, what is understandable since

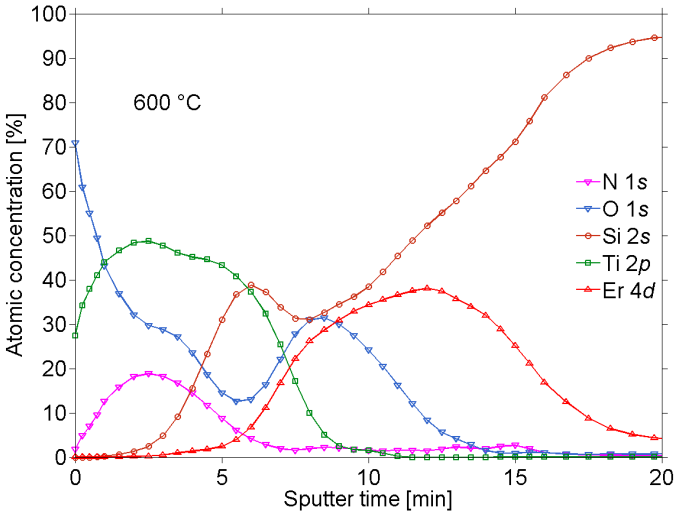

Figure 3.20: XPS atomic concentration depth profile of the capped sample annealed at 600 °C.

the annealing temperature is substantially higher. It is also striking to observe that Si diffuses appreciably closer towards the surface. In consequence, contrary to Fig. 3.18, we can see the simultaneous occurrence of Ti and Si in the last layers of the cap, what could be a sign of the formation of Ti-Si phases. However, this hypothesis must be discarded since it is known that the BEs of Ti and Si remain nearly unaffected by alloying in $TiSi_2$ [122], contrary to our observation. Another consequence of the enhanced Si diffusion is that the $ErSi_{2-x}$ and Er oxide layers are less distinctly separated and interpenetrate each other, as already disclosed by the XTEM results. Indeed, the presence of $ErSi_{2-x}$ extends on a much more important part of the stack, between 5 and 13 min, as testified by the Si 2*s* peak of 150.4 eV. In addition, the presence of a pure $ErSi_{2-x}$ layer (without apparent oxygen contamination), restricted to the region comprised between 11 and 13 min, can be identified. After 16 min of sputtering, the Si bulk is reached.

Figure 3.21 presents the experimental Arrhenius plot (circles) extracted from I-V_{4C}-T characteristics and the corresponding fit (solid

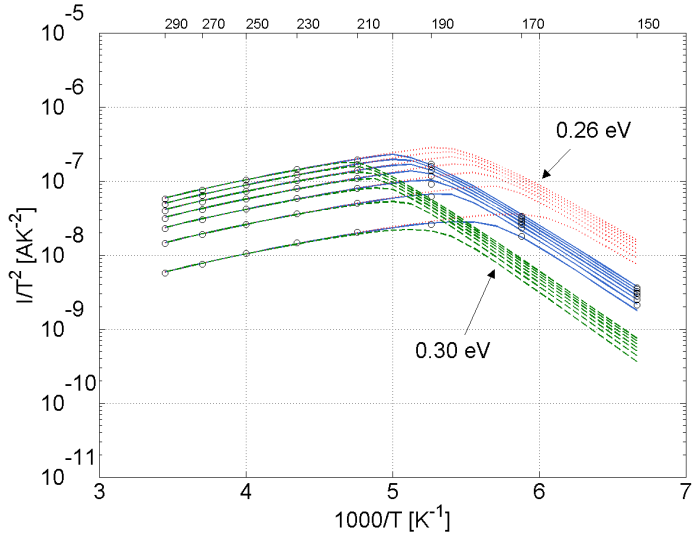

Figure 3.21: Experimental Arrhenius plot (circles) extracted from the I-V_{4C}-T characteristics and the corresponding fit (solid curves), for the capped sample annealed at 450 °C. The selected voltages range from 0.1 to 1 V with a step of 0.15 V for measurement temperatures ranging from 150 up to 290 K with a step of 20 K. The experimental data are fitted with the TFE+BL model. The extracted SBH is equal to 0.28 eV. A small increase (dashed curves for $\Phi_{Bn} = 0.30$ eV) or decrease (dotted curves for $\Phi_{Bn} = 0.26$ eV) in Φ_{Bn} results in a down- or upshift of the theoretical curves comparatively to the reference curve.

curves), for the sample annealed at 450 °C. The selected biases are 0.1 up to 1 V with a step of 0.15 V and the measurement temperatures range from 150 up to 290 K with a step of 20 K. The experimental data are fitted with the TFE+BL model. The extracted barrier is found to be equal to 0.28 eV, identical to the smallest SBH found in literature regarding $ErSi_{2-x}$ [60,61]. It is also worth noting that experimental and theoretical data fit remarkably well. Furthermore, a small increase (dashed curves for $\Phi_{Bn} = 0.30$ eV, in Fig. 3.21) or decrease (dotted curves for $\Phi_{Bn} = 0.26$ eV, in Fig. 3.21) of the SBH in the model results in a clearly visible down- or upshift of the theoretical curves comparatively to the reference curve corresponding to 0.28 eV. This indicates the high sensitivity of the model that allows a very accurate determination of the SBH. Moreover, the model allows an accurate fit on the whole measurement temperature range, suggesting a low level of interfa-

cial contamination. Indeed, it was recently pointed out that deviations from the TE model for $ErSi_{2-x}$ Schottky diodes are caused either by SBH inhomogeneities [104] or trap-assisted tunneling [106], both most likely due to some interfacial contamination. Since we do not observe such deviations from the TFE+BL model, the contamination level should be very low for our samples.

The presence of a small oxygen concentration at the interface was previously shown to be responsible for SBH augmentation [65]. In consequence, the state-of-the-art SBH of 0.28 eV manifests the efficiency of the Ti capping to preserve the $ErSi_{2-x}$/Si interface from oxygen diffusing through the cap during the thermal treatment. Another possible source of contamination in oxygen is related to the degree of cleanness of the Si surface prior to evaporation, more specifically the presence of a very thin layer of Si oxide. It is known that the presence of such a thin interfacial oxide before evaporation causes a dramatic increase of the SBH after heating [80]. For that reason, possible oxide regrowth in ambient air before the introduction in the evaporation chamber should be very limited in the present case. Consequently, the simple cleaning method (SPM + HF dip) used here appears sufficient to reach a low SBH, without the need of a complicated *in situ* procedure to prepare the Si surface [126]. Finally, the low SBH also indicates that, contrary to W [105], Ti does not diffuse to the $ErSi_{2-x}$/Si interface since the presence of interfacial Ti silicide would likely be responsible for a SBH augmentation owing to the high SBH of Ti silicide (around 0.6 eV). This confirms that Er and Ti do not intermix during the silicidation [73].

In Fig. 3.7, it can be observed that there is a plateau at 0.28 eV for the annealing temperatures of 450 and 500 °C, respectively. However, as and when the annealing temperature is increased, the SBH is slightly increased as well and amounts to 0.31 eV for 600 °C. Very few research groups have proposed hypotheses to account for the SBH increase comparatively to the state of the art of 0.28 eV. Unewisse *et al.* [61] have identified a correlation between the SBH and the degree of roughness of the $ErSi_{2-x}$/Si interface. Alternately, Muret *et al.* [65] have proposed that the oxygen concentration in $ErSi_{2-x}$ is directly related to the SBH: the higher the concentration, the higher the SBH.

Since the previous XTEM investigations do not exhibit any significant variation between the interfaces of samples heated at 450 and 600 °C (the interface is smooth in both cases), we suspect that oxygen contamination might play a role in the SBH increase. To verify this hypothesis, the photoemission measurements of the Er $4d$ core levels are fitted with a standard linear least-squares decomposition procedure. Such a procedure allows separating the respective contributions of Er oxide and

$ErSi_{2-x}$ in the Er $4d$ profile and thereby determining which compound is preponderant at the interface. Figures 3.22(a) and 3.22(b) show the resulting decomposition of the Er $4d$ profile into its Er $4d$(Er oxide) and Er $4d$($ErSi_{2-x}$) components, for 450 and 600 °C, respectively. Figure 3.22(c) illustrates the extracted basis spectra used for the decomposition: the peak at 167.8 eV is relevant to $ErSi_{2-x}$ while the peak at 169.8 eV is relevant to Er oxide. By integrating the surface under the profile curves exhibited in Figs. 3.22(a) and 3.22(b), we calculate the Er $4d$(Er oxide) proportion of the total Er $4d$ profile for each temperature.

First, we find out that no interfacial oxygen is recorded at 600 °C, within the experimental accuracy. However, when we compare the progression of the oxidation front (defined as the maximum of the Er oxide component, as illustrated in Figs. 3.22(a) and 3.22(b)) in direction of the interface at 450 and 600 °C, we discover that it gets appreciably closer to the interface for 600 °C. Moreover, the proportion of Er oxide increases from 28 to 36% between 450 and 600 °C. These two observations show that the $ErSi_{2-x}$ film grown at 600 °C is more contaminated by oxygen because the capability of the Ti cap to prevent oxygen diffusion during the silicidation is reduced at higher annealing temperatures. Even though no interfacial oxygen can be detected by XPS (with a 0.1-0.5 atomic-% detection limit), we cannot exclude the occurrence of a very small oxygen concentration which could result in a slight SBH augmentation, as already mentioned above. Alternately, this enhanced diffusion could provoke a slight morphological degradation of the $ErSi_{2-x}$/Si interface which could in turn affect the SBH [61]. Based on the XTEM micrographs presented here, we cannot totally revoke the roughness argument to explain the SBH increase. Planview HRTEM would provide more information. However that may be, the SBH extraction based on back-to-back Schottky diodes (and in consequence, the SBH itself) proves out to be remarkably sensitive to the intrinsic characteristics of the MS interface.

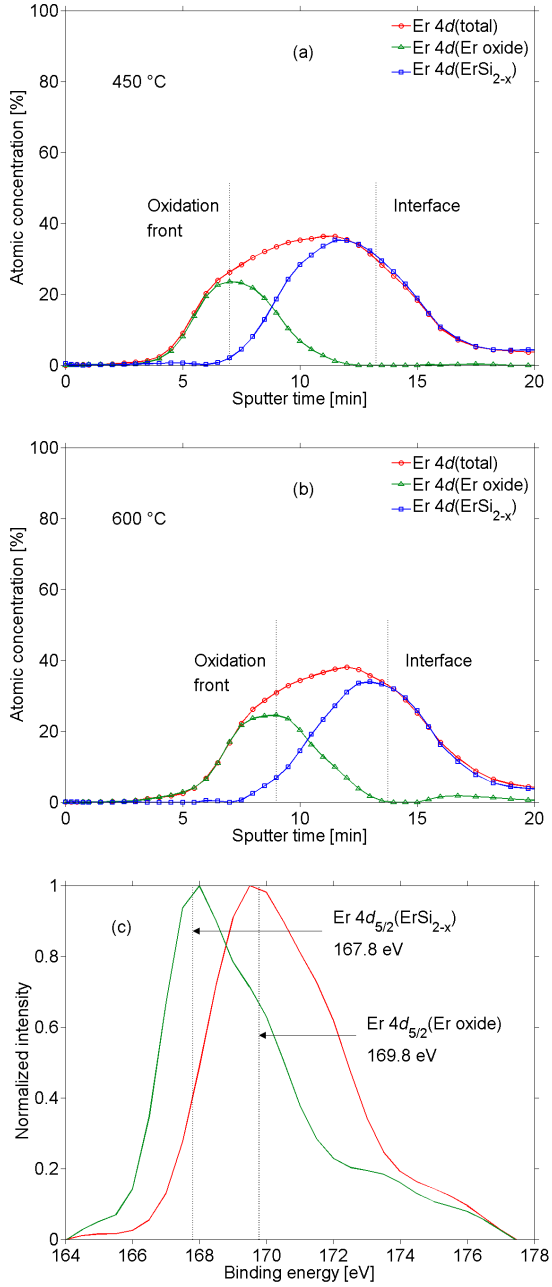

Figure 3.22: Decomposition of the Er 4*d* atomic concentration depth profile for the capped samples annealed at (a) 450 and (b) 600 °C, respectively. (c) Extracted basis spectra used for the decomposition: 167.8 and 169.8 eV are BEs relevant to $ErSi_{2-x}$ and Er oxide, respectively.

3.4.1.5 Summary

This section was devoted to the formation of Er silicide evaporated in UHV conditions with a thin Ti cap and grown *ex situ* by RTA. The SBH proved to progressively decrease with the augmentation of the annealing temperature, then reached a plateau of 0.28 eV between 450 and 500 °C, and, finally, increased slightly upon annealing at higher temperature (600 °C). From XRD and HRTEM inspections, the SBH drop in the low annealing temperature region ($\leq$ 450 °C) appeared associated to the progressive formation of crystalline Er silicide. Above 450 °C, no satisfactory explanation for the SBH increase was found. It could be attributed to an enhanced oxygen contamination of the Er silicide film due to the higher annealing temperature, as observed by XPS depth profiling. But XPS disclosed the presence of oxygen at the interface and thus its possible impact on the SBH, at least within the experimental accuracy.

3.4.2 Evaporation in high vacuum conditions

To further relax the constraints on the growth of $ErSi_{2-x}$, we propose here to investigate $ErSi_{2-x}$ formation with a Ti cap in a more conventional evaporation system operating under HV conditions. First, several stacks prepared in various conditions are deeply investigated by XPS. Next, based on the best process parameters determined by XPS, we extract SBHs for face-to-face diodes formed with a SiO_2 mask and extend the physical study to XTEM and XRD.

3.4.2.1 X-ray photoelectron spectroscopy investigation

From the previous sections, it clearly turns out that the top of the $ErSi_{2-x}$ film is contaminated by oxygen with a Ti cap of 10 nm. Before beginning any new study, it is first important to inspect the process conditions to minimize or even suppress oxygen contamination since oxygen is detrimental to the electrical properties of $ErSi_{2-x}$. In the following, we explore in detail by XPS the chemical state of Er covered by a Ti capping layer, either without thermal budget or subjected to *ex situ* RTA at low (300 °C) or moderate (600 °C) temperatures. We examine the progression of the solid-state reaction occurring between Er and Si at the interface with Si and the interaction between the superficial layers of the Er film and residual oxygen diffusing through the capping layer. In addition, since relatively few XPS data about Er-Si or Er-O reactions are disseminated in the literature, a supplementary motivation of our

study is to synthetize and to enhance the information available on that topic.

3.4.2.1.1 Sample preparation The Si wafers are prepared as previously mentioned prior to evaporation. The metal deposition is realized in an e-beam evaporator with a base pressure of $\sim 10^{-7}$ mbar. In order to clean the Er and Ti targets, 50 nm of metal are evaporated just before deposition (with the shutter closed). 25 nm of Er and different Ti thicknesses (10, 15, and 50 nm) are then successively deposited. Sample 1 (with 10 nm of Ti) is left as-deposited. Four samples (2 to 5) with various Ti thicknesses (t_{Ti}) are heated *ex situ* by RTA in nitrogen under diverse annealing conditions, immediately after extraction from the evaporator: (i) sample 2 with t_{Ti} = 10 nm annealed at 300 °C for 2 min with a 2 min initial purge, (ii) sample 3 with t_{Ti} = 15 nm annealed at 600 °C for 2 min with a 2 min initial purge, (iii) sample 4 with t_{Ti} = 50 nm annealed at 600 °C for 2 min with a 2 min initial purge, and (iv) sample 5 with t_{Ti} = 10 nm annealed at 600 °C for 2 min with a 10 min initial purge. To help the reader, Table 3.1 recapitulates the stack thicknesses and the RTA conditions.

Sample	t_{Ti} [nm]	Annealing temperature [°C]	Pre-RTA purge duration [min]
1	10	X	2
2	10	300	2
3	15	600	2
4	50	600	2
5	10	600	10

Table 3.1: Summary of the stack thicknesses and RTA conditions.

3.4.2.1.2 X-ray photoelectron spectroscopy data Core level spectra are recorded from erbium (Er 4*d*), oxygen (O 1*s*), silicon (Si 2*p* or Si 2*s*), and titanium (Ti 2*p*). For all five samples, intensity depth profiles are determined from the corresponding spectra. As previously, capital letters with distinct superscripts for each sample are used to mark characteristic positions along the intensity profile. The information that we can extract from intensity profiles is relatively poor in the specific case of Er. Quantitative analysis from such profiles is particularly delicate because of the relative difficulty to obtain accurate intensities, since Er possesses a complex spectrum for which the determination of the integration

boundaries is ambiguous. Moreover, discrepancies can arise from different sputter yields and burial effects. To push the investigation further, we rather focus on the BE changes, mainly from Er $4d$ and Si $2p/2s$ spectra. We also follow the modifications of the spectrum shape since it brings valuable extra information, especially for Er. BEs relative to metallic, oxidized or silicided Er can be found in [113,116,119,120,125,127–131]. To make the interpretation of the recorded spectra easier, Table 3.2 summarizes the Er $4d_{5/2}$, O $1s$, and Si $2p/2s$ BEs found in the above-mentioned papers. In addition, Table 3.2 also contains typical peak positions relevant to Si-O and Ti-O compounds [124,132–138] that could presumably form during RTA. When a BE is given in the text below, the reader is systematically invited to refer to Table 3.2 for more information about the corresponding reference. In addition, all BEs recorded at the different markers are gathered in Table 3.3, to facilitate the reading of the article.

Peak	Compound	BE [eV]	Reference
Er $4d_{5/2}$	Er	167.4+169 (sat.)	Swami
		167.6	Kennou
		167.1	Reckinger
	$ErSi_{2-x}$	167.6	Kennou
	Er/Si	167.3	Reckinger
	ErO_x	168.7	Uwamino
		168.6	Swami
		168.8	Wagner
		170.4	Guerfi,Kennou
	Er/O	169.2	Kennou
		169.5	Reckinger
O $1s$	Er_2O_3	530.6	Swami
		531.6	Guerfi,Netzer
	SiO_x ($x \approx 1$)	532-533	Kennou
	SiO_2	533.2	Kennou
		533.1	Larrieu
	TiO_2	529.3-531	Atuchin
		530.5	Demri
		529.8	Moses
Si $2s$	Si	150.7	Ogama
		150.5-150.6	Reckinger
	SiO_2	154.2	Anpo
	Er/Si	149.5	Reckinger
Si $2p$	Si	99.3	Lollman,Gokhale
	$ErSi_{2-x}$	99	Lollman
	Er/Si	98.1	Lollman
		Shift: 0 to 1.3	Wetzel
	SiO_2	∼103	Guerfi
	SiO_x	∼102	Guerfi
Ti $2p_{3/2}$	Ti	454	Atuchin
		454	Badrinarayanan
	TiO_2	459	Atuchin
		458.9	Gonbeau
		458.9	Demri

Table 3.2: XPS BEs relevant to Er $4d_{5/2}$, O $1s$, Si $2p/2s$, and Ti $2p_{3/2}$ core levels stemming from the literature.

Sample	Marker	ST [min]	Ti $2p_{3/2}$	O $1s$	Er $4d_{5/2}$	Si $2p/2s$
1	A	0	458.9	530.5	X	X
	B	56	453.7	530.9	167.7	X
	C	68	453.7	530.7	167.1	X
	D	80	453.5	530.7	167.1	X
	E	112	X	X	167.1	98.3
	F	132	X	X	167.3	98.9
	G	156	X	X	167.3	99.1
2	A'	0	459	530.5	X	X
	B'	56	454	530.9	169.4	X
	C'	96	454	531.1	169.5	X
	D'	124	X	531.1	169.5	149.5
	E'	152	X	531.1	169.1	149.7
	F'	168	X	531	167.5	149.6
	G'	184	X	530.7	167.3	149.8
	H'	208	X	X	167.3	150.3
	I'	236	X	X	167.5	150.5
3	A"	0	459.1	530.5	X	X
	B"	152	455.1	531.1	169.1	102.9/98.8
	C"	200	454.1	531	169.1	98.9
	D"	248	X	530.9	167.5	98.6
	E"	276	X	530.3	167.3	98.7
	F"	300	X	X	167.3	99.1
4	A*	48	454	531.4	X	149.7
	B*	96	453.8	531.2	X	149.8
	C*	152	453.8	530.9	167.3	149.9
	D*	232	X	X	167.3	150
	E*	280	X	X	167.3	150.5
5	A**	148	X	531.1	167.5	150.1
	B**	204	X	X	167.3	150.2
	C**	220	X	X	167.3	150.5

Table 3.3: Summary of the Ti $2p_{3/2}$, O $1s$, Er $4d_{5/2}$, and Si $2p/2s$ BEs [eV] recorded at the different markers for all considered samples.

3.4.2.1.3 As-deposited sample with a 10 nm thick Ti cap Figure 3.23 displays the XPS intensity depth profile for sample 1 (with markers A to G). It can be clearly observed that oxygen can penetrate into the Ti layer but remains essentially concentrated at the surface since the oxygen amount is seen to quickly decrease. The top surface (marker A) is characterized by a Ti $2p_{3/2}$ BE of 458.9 eV. Elemental Ti features a Ti $2p_{3/2}$ core level peak centered at 454 eV while its position is reported to shift to 458.9-459 eV when TiO_2 is considered. The presence of TiO_2 is therefore unambiguously identified at the top surface of the stack, expectable due to the strong reactivity of Ti in the presence of oxygen. Oxygen most probably originates from ambient air, by diffusion in the Ti cap during the transfer between the evaporation and the introduction in the XPS analysis chamber.

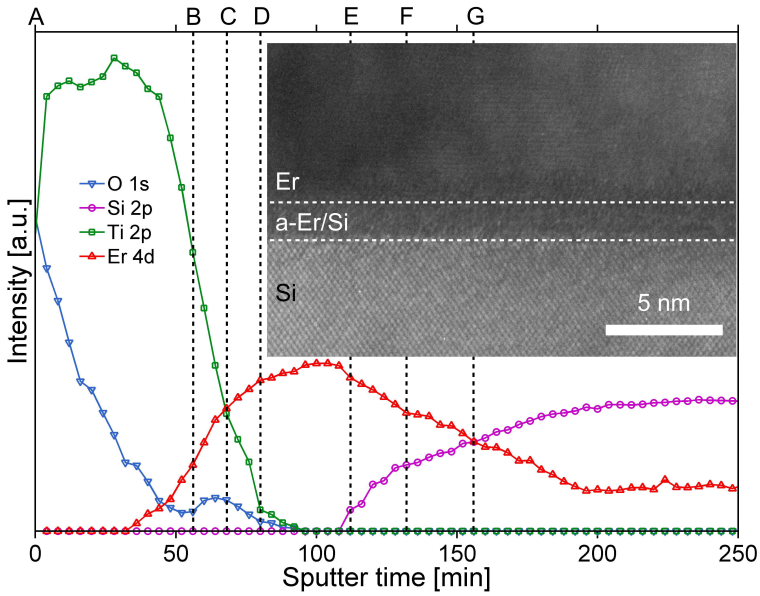

Figure 3.23: XPS intensity depth profile of the as-deposited Ti(10 nm)/Er(25 nm)/Si(100) stack. Particular positions along the profile are marked by labels A to G. Inset: cross-sectional HRTEM picture of the interface between a-Er/Si and Si.

Deep inside the top layer (marker B), near the interface with the Er film, Ti is weakly or not affected by oxidation, as confirmed by the Ti $2p_{3/2}$ peak position which is centered at 453.7 eV. Simultaneously, a small amount of Er is detected. It is interesting here to check for the efficiency of the Ti capping layer to preserve Er from oxidation after

a short time in ambient air. Before examining the chemical state of deposited Er at label B, we provide BE reference values for elemental and oxidized Er obtained from a sixth sample with a thick Er layer, deposited and analyzed in the same conditions. Figure 3.24 displays the corresponding normalized Er 4*d* core level spectra after background subtraction. For elemental Er (deep inside the film), we extract an Er $4d_{5/2}$ BE value of 167.1 eV, in fair agreement with the values found by Swami *et al.* (167.4 eV), Kennou *et al.* (167.6 eV), and the previous work. In addition, Swami *et al.* [130] mentioned that the Er $4d_{5/2}$ peak of elemental Er presents a well-resolved satellite peak[4] (with a core level peak of 169 eV), contrary to oxidized Er, as also observed here at 169.2 eV in Fig. 3.24. From the analysis of the oxidized surface of the same Er thick film, Er $4d_{5/2}$ and O 1*s* core levels are found to be centered at 169.3 and 531.2 eV, respectively. Previously published material gives corresponding BEs comprised between 168.6 and 170.4 eV for Er $4d_{5/2}$ and in the 530.6-531.6 eV range for O 1*s* (see Table 3.3). Even though those data are rather scattered, the Er $4d_{5/2}$ peak of oxidized Er can be readily recognized since it presents two plainly identifiable characteristics comparatively to metallic Er (see Fig. 3.24): (1) both main and satellite peaks merge in the oxide form and (2) the energy of the main peak is systematically about 2 eV higher than its metallic counterpart. The inspection of the Er 4*d* spectrum at marker B gives a BE equal to 167.7 eV. A likely interpretation is that Er at marker B is a mixture of oxidized and mainly elemental Er.

Slightly deeper, starting from marker C, the BE of the Er $4d_{5/2}$ main peak becomes constant and is determined to be 167.1 eV, as exhibited in Fig. 3.25 presenting the evolution of the Er $4d_{5/2}$ and Si 2*p* BEs versus ST. Figure 3.26, which gives the Er 4*d* normalized spectrum at some selected positions after background subtraction, illustrates also the appearance of the doublet peak structure from marker C, thereby confirming the metallic state of Er. But it is however worth noting that the match is not perfect between the peak of elemental Er in Fig. 3.24 and the Er 4*d* spectrum at C: it clearly turns out that the satellite peak to main peak intensity ratio is higher. This might hypothetically indicate that Er is not yet entirely metallic and could be very weakly oxidized. Just below C, at marker D, Er is now plainly metallic, as exhibited by the Er 4*d* spectrum in Fig. 3.26. Between markers B and D, the occurrence of a slight pile-up of oxygen is observed (see Fig. 3.23). This contamination could be either attributed to the residual oxidation of the Ti target

[4]To be precise, what we call the Er $4d_{5/2}$ BE throughout the text is that of the main Er $4d_{5/2}$ peak.

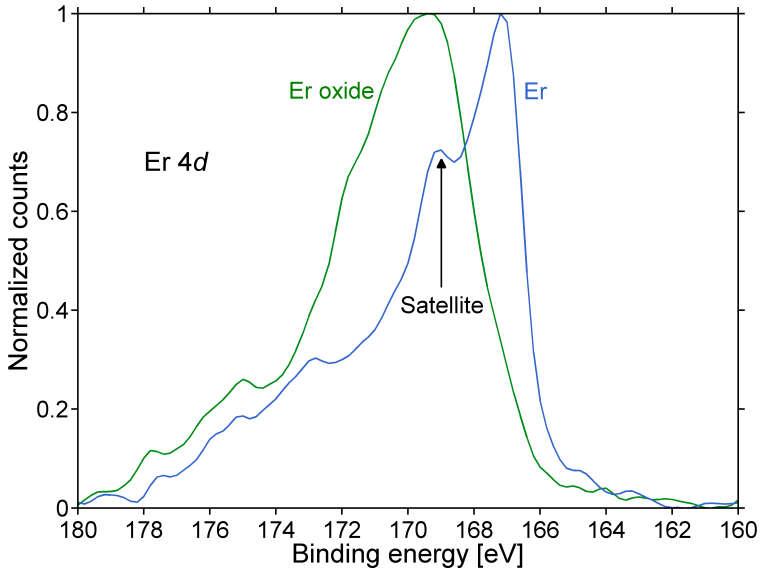

Figure 3.24: Typical normalized Er 4*d* core level spectra after background subtraction for metallic and oxidized Er, respectively. The spectra are obtained from a thick Er layer to serve as a reference. The Er $4d_{5/2}$ main peak of elemental Er is located at 167.1 eV while its satellite is at 169.2 eV. Oxidized Er is characterized by a unique peak at 169.3 eV.

in the crucible when Ti is evaporated onto the existing Er layer or to the exposition of Er to the residual vacuum in the deposition chamber before Ti deposition. Nevertheless, even with a Ti capping layer as thin as 10 nm, the oxidation of the Er film is very superficial.

More in depth, at a position referring to marker E, Si shows up, with a corresponding Si 2*p* peak of 98.3 eV, as shown in Fig. 3.25. Upon further sputtering, the Si 2*p* BE shows a consequential raise to 98.9 eV at label F, and then increases slowly to reach a plateau of 99.1 eV at marker G. Lollman *et al.* [120] observed a similar shift for the deposition of thin Er layers over Si(111). During the room-temperature deposition of Er, Er and Si atoms can intermix since the Er atoms react strongly with Si (solid-state amorphization [87]). With the increase of the deposited thickness, Si atoms are more diluted into the Er film and are consequently surrounded by a greater number of Er atoms, resulting in a larger Si 2*p* BE shift. Similarly, Wetzel *et al.* [119] reported a variation of the Si 2*p* BE for amorphous mixtures of Er and Si (Er_xSi_{1-x}, $x \leq 1$), depending on the concentration of Si in Er (large shift of 1.3

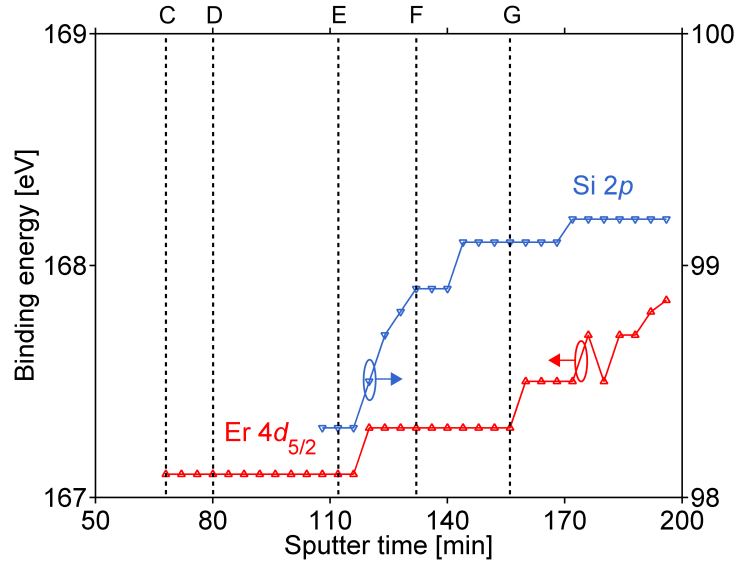

Figure 3.25: Er $4d_{5/2}$ and Si $2p$ BEs for the as-deposited Ti(10 nm)/Er(25 nm)/Si(100) stack, from marker C.

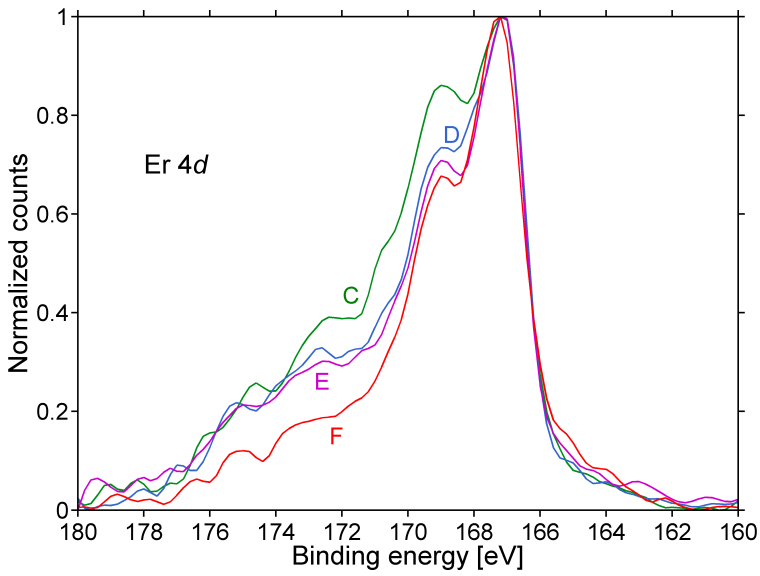

Figure 3.26: Normalized Er $4d$ core level spectra after background subtraction for the as-deposited Ti(10 nm)/Er(25 nm)/Si(100) stack, for markers C to F.

eV for $x \approx 0.8$). In consequence, the layer between E and G can be very likely identified with an Er/Si mixture of variable composition with an Er/Si intensity ratio that progressively decreases when approaching marker G, as indicated by the concomitant increase of the Si $2p$ BE (see Fig. 3.25). However, it is important to draw here the attention on one detail. As already mentioned before, the Si $2p$ BE in the Er/Si film (between E and G) in Fig. 3.25 exhibits two distinct behaviors: an abrupt variation (E-F) followed by a slow increase (F-G). Indeed, XPS does not only probe the very surface of the sample but also a small thickness below, depending widely on the material under investigation. This effect must all the more be taken into consideration when thin layers are considered. The previous comment is very general and is still valid for the remainder of our analysis. Consequently, we think that the change of behavior in the F-G layer is related to the Si substrate detection. A connection can be made between the Er/Si alloy and the thin a-Er/Si layer of 3 nm observed in the HRTEM picture (inset to Fig. 3.25). On the contrary, the Er $4d_{5/2}$ BE is constant (167.3 eV) throughout the intermixed layer (see Fig. 3.25). A typical Er $4d$ spectrum (extracted at marker F) that we attribute to silicided Er is shown in Fig. 3.26 with a shift of 0.2 eV towards higher BE after position E. The shapes of the elemental and silicided Er spectra are very similar. Kennou *et al.* [125] even observed no BE difference at all. A weak or negligible shift denotes a weak charge transfer between Si and Er upon alloying, as generally observed for transition metals [139].

After G, the Si $2p$ BE of 99.2 eV corresponds to elemental Si, meaning that we reach the Si bulk substrate while the Er $4d_{5/2}$ typical doublet structure progressively disappears but is still detected (see Fig. 3.23): Er is thought to redeposit and even bury into the substrate during the sputtering process due to its heavy mass ("knock-on effect" [140]).

3.4.2.1.4 Sample with a 10 nm thick Ti cap annealed at 300 °C

From Fig. 3.27, depicting the XPS intensity depth profile for sample 2 (with markers A' to H'), we can see that, after annealing at 300 °C, a large amount of oxygen diffuses through the whole stack. As previously, the surface (marker A') is composed of TiO_2. At label B' (same depth as B), the Er $4d_{5/2}$ core level is centered at 169.4 eV (instead of 167.7 eV for the as-deposited sample), a BE which is shifted by more than 2 eV when compared to its value for elemental Er. This observation demonstrates that Er is now present in its oxidized form. Concomitantly, the O $1s$ peak position is shifted from 530.5 eV at position A' to 531 eV at position B', indicating that oxygen is now preferably coupled to Er rather than to

Ti. Surprisingly, the Ti $2p_{3/2}$ BE energy is found to be equal to 454 eV, which can be ascribed to either elemental or slightly oxidized Ti. Those previous results could indicate that, at 300 °C, Er oxidizes much faster and preferentially compared with Ti. As a significant part of oxygen at position B' originates from diffusion through the Ti layer, it is speculated that Er could even reduce Ti oxide: a similar situation was reported by Kennou *et al.* [125] who observed the reduction of SiO_2 by Er at 750 °C. Moreover, the preferential formation of Er oxide relatively to Ti oxide is confirmed by the respective heats of formation of -1897.9 $kJmol^{-1}$ for Er_2O_3 and -944 $kJmol^{-1}$ for TiO_2 [141]. Below position

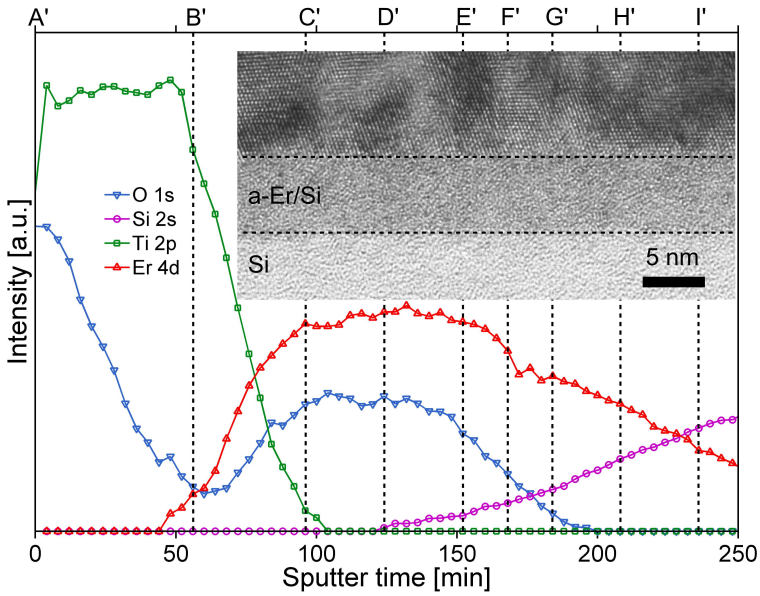

Figure 3.27: XPS intensity depth profile of the Ti(10 nm)/Er(25 nm)/Si(100) stack annealed at 300 °C for 2 min with a 2 min pre-RTA purge. Particular positions along the profile are marked by labels A' to I'. Inset: cross-sectional HRTEM picture of the interface between a-Er/Si and Si.

B', we can see that a considerable amount of oxygen penetrates into the cap (Fig. 3.27), causing a deep oxidation of the Er layer. This assertion is confirmed by the analysis of the Er $4d_{5/2}$ and O $1s$ peaks' positions at marker C' (slightly below the cap): BEs of 169.5 and 531.1 eV are respectively recorded. Between B' and C', Er is completely oxidized and we do not detect the presence of elemental Er anymore. The previous observations constitute evidence that Er is oxidized in depth due to the

activation of the diffusion of residual oxygen in the RTA chamber under the application of the thermal budget.

Si shows up at position D' with a weak Si 2*s* peak centered around 149.5 eV, as we can see in Fig. 3.28 showing the evolution of the Si 2*s* and Er $4d_{5/2}$ BEs versus ST. In comparison with BEs for pure Si (150.5 eV), this value of 149.5 eV suggests the formation of a small Er silicide quantity even though the Er $4d_{5/2}$ core level at D' firmly remains in the accepted range for oxidized Er (169.5 eV). Nevertheless, when compared to the BE at marker C' (oxidized Er without Si), it appears that the shape of the Er $4d_{5/2}$ peak somewhat transforms (see Fig. 3.29), leading also to think that a small part of the Er film could be alloyed to Si.

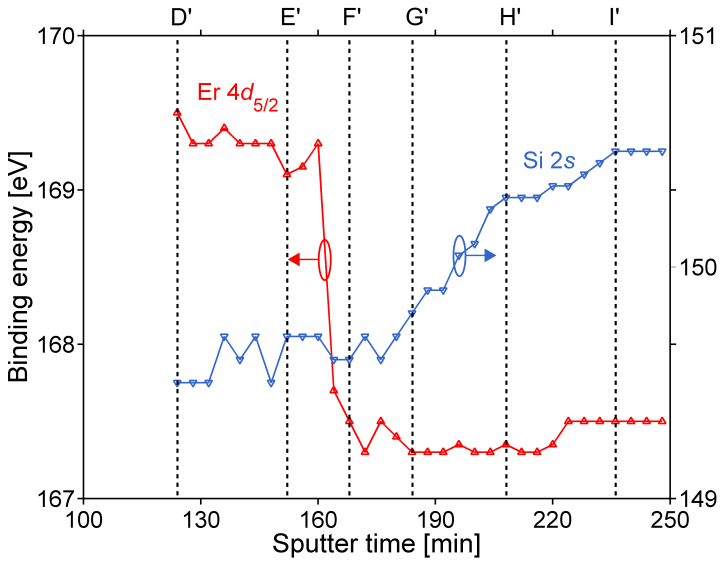

Figure 3.28: Er $4d_{5/2}$ and Si 2*s* BEs for the Ti(10 nm)/Er(25 nm)/Si(100) stack annealed at 300 °C for 2 min with a 2 min pre-RTA purge, from marker D'.

Upon further sputtering (positions E' and F'), the characteristic shape of the Er $4d_{5/2}$ peak continues to modify comparatively to marker D' (see Fig. 3.29), while the Si 2*s* BE remains roughly unchanged (Fig. 3.28). This suggests that, below marker D', the original metallic Er film is converted into a mixture of silicided and oxidized Er because of the antagonist diffusion of, on the one side, oxygen through the Ti cap and, on the other side, Si in Er in the opposite direction [76]. The evolution of both the Er $4d_{5/2}$ peak shape and BE probably reflects a progressive change in chemical environment, more specifically, the increase with

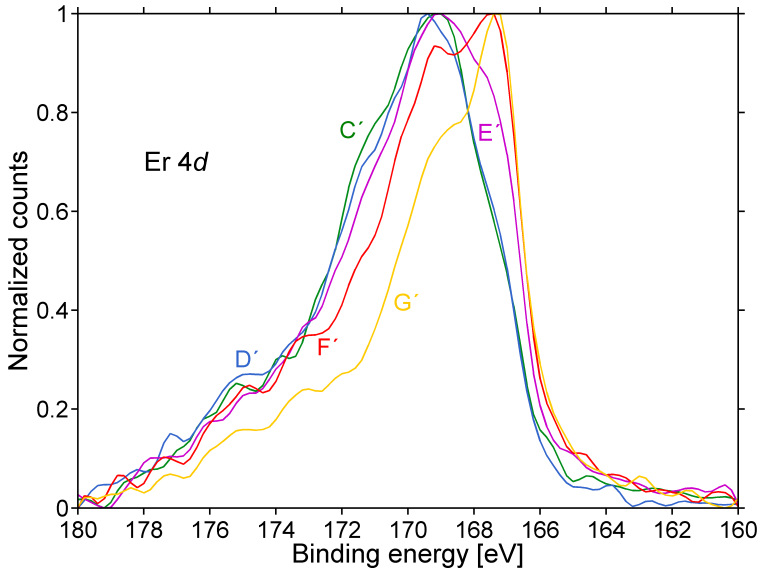

Figure 3.29: Normalized Er $4d$ core level spectra after background subtraction for the Ti(10 nm)/Er(25 nm)/Si(100) stack annealed at 300 °C for 2 min with a 2 min pre-RTA purge, for markers C' to G'.

depth of the Er silicide proportion in the alloy.

Indeed, at position G' (Fig. 3.29), the Er $4d_{5/2}$ peak is now split into a doublet structure very much alike the one depicted in Fig. 3.26 at marker F, meaning that Er is no more present in its oxide form and thus in all likelihood silicided. It is worth mentioning that the doublet already shows up before, at position F', but the global shape of the Er $4d_{5/2}$ core level at that label remains significantly different from that of Er silicide. From a quantitative standpoint, the Er $4d_{5/2}$ BE is recorded at 167.3 eV, BE which is assumed to be related to Er silicide formation as already noted at the interface with Si (marker F) of the previous as-deposited sample. The Si $2s$ BE of 149.8 eV reinforces the assertion that Er appears to be preferably coupled to Si at label G'. Despite the occurrence of some oxygen, there is no contradiction with the previous statement that Er forms a silicide at this position since, as already mentioned, the signature of both materials can be often detected on both sides of an interface.

In Fig. 3.28, we can see that below G', as previously observed for sample 1, the Er $4d_{5/2}$ BE is nearly constant (167.3 eV) while the Si $2s$ peak rapidly shifts from 149.8 to 150.3 eV (position H') and then slowly reaches 150.5 eV at label I'. Once again, the layer between G' and I' can be assimilated to an Er/Si mixture of variable composition and

can be associated to the a-Er/Si layer depicted in the HRTEM inset to Fig. 3.27. The same parallel can be made between layers H'-I' and F-G: the slow-down of the Si 2*p* BE shift can be linked to the onset of the Si substrate probing. But the comparative inspection of Figs. 3.23 and 3.27 suggests that the Er/Si layer is much broader at 300 °C (thickness E-G smaller than thickness F'-I'), as also confirmed by the HRTEM analyses (3 nm versus 6 nm).

3.4.2.1.5 Annealing at 600 °C To form a crystalline and stable Er silicide film with the present process conditions, annealing temperatures higher than 300 °C are required, at least 400 °C (see below). To better evidence the potential oxygen diffusion, we set the annealing temperature at 600 °C. Since the stack was already strongly oxidized at 300 °C for a 10 nm thick capping layer, we investigate the increase of the Ti layer thickness (15 nm for sample 3 and 50 nm for sample 4) as a means to improve the protection against oxygen diffusion. Another element that deserves further exploration is the potential impact of the residual oxygen concentration in the RTA chamber during the annealing. To that purpose, an additional sample with a fixed Ti thickness of 10 nm is annealed for a considerably longer pre-RTA purge time of 10 min (sample 5). It is worth recalling here that samples 3 and 4 are grown after a short pre-RTA purge step of 2 min, like samples 1 and 2.

Sample with a 15 nm thick Ti cap annealed with a pre-RTA purge of 2 min As featured in Fig. 3.30, a lot of oxygen penetrates into the stack and contaminates the top of the Er profile. Without surprise, the surface of the capping layer is composed of TiO_2 (marker A"). More in depth, the cap is essentially a mixture of TiO, TiO_2, and Ti, with a progressively decreasing TiO_2 amount.

A detectable Er signal can be registered from marker B". In the top of the Er profile (between positions B" and D"), Er is essentially oxidized (with characteristic O 1*s* and Er $4d_{5/2}$ BEs of 531.1 and 169.1 eV, respectively). Throughout the whole B"-D" region, the Si 2*p* spectra are characterized by two main peaks with roughly constant BEs at ∼103 and ∼98.8 eV (Fig. 3.31(a)). The first BE testifies to the persistence of stoechiometric Si oxide. If we have a closer look at the spectrum of the intermediate position C" in Fig. 3.31(a), we can also notice the presence of several small peaks between the two main ones, probably from Si suboxides. Comparing the Si 2*p* spectra at markers B", C", and D" in Fig. 3.31(a), it is also found out that the SiO_2 signal progressively fades out. As we know that $ErSi_{2-x}$ grows at 600 °C (confirmed by HRTEM and

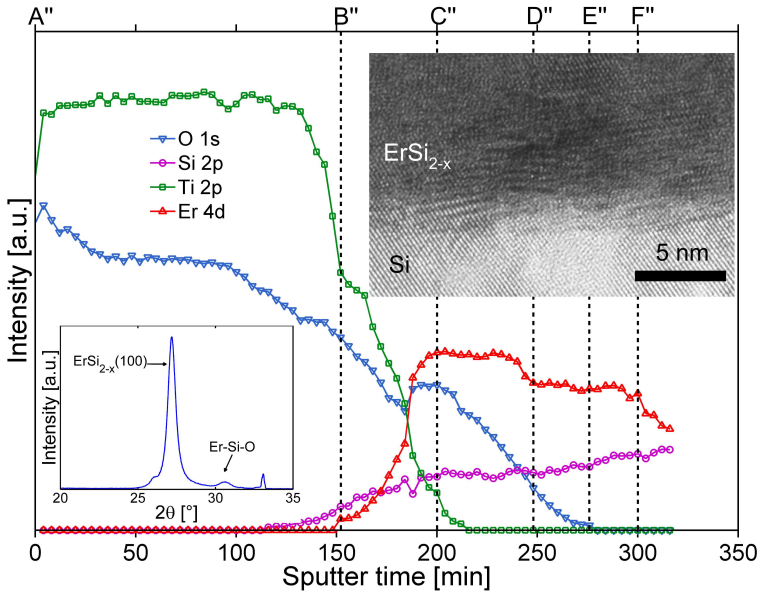

Figure 3.30: XPS intensity depth profile of the Ti(15 nm)/Er(25 nm)/Si(100) stack annealed at 600 °C for 2 min with a 2 min pre-RTA purge. Particular positions along the profile are marked by labels A" to F". Inset1: cross-sectional HRTEM picture of the interface between $ErSi_{2-x}$ and Si. Inset2: XRD spectrum with a strong peak corresponding to $ErSi_{2-x}$.

XRD analyses (insets to Fig. 3.30)), we believe that the small but visible ∼0.4 eV shift of the second Si 2*p* peak relatively to the elemental Si peak can be attributed to $ErSi_{2-x}$ [120] (see Fig. 3.31(a)). Between B" and D", the $ErSi_{2-x}$ Si 2*p* peak becomes steadily predominant comparatively to the SiO_x peaks, reflecting a progressive increase of the $ErSi_{2-x}$ proportion (see Fig. 3.31(a)). Before label D", the Er $4d_{5/2}$ core level of ∼169.1 eV can be unambiguously attributed to oxidized Er. Still, its shape shows a drastic modification between C" and D" (Fig. 3.31(b)), comparable to the one observed for sample 2. We can conclude that the layer between B" and D" is a mixture composed of, on the one side, oxidized Er and Si and, on the other side, $ErSi_{2-x}$ (possibly Er-Si-O compounds, as detected by XRD (inset to Fig. 3.30)), with a progressively increasing $ErSi_{2-x}$ concentration with depth.

The typical doublet structure of Er silicide appears at marker D" and the corresponding Er $4d_{5/2}$ core level drops to 167.5 eV (i.e. the main Er $4d_{5/2}$ peak becomes dominant). It is interesting at this point to make a

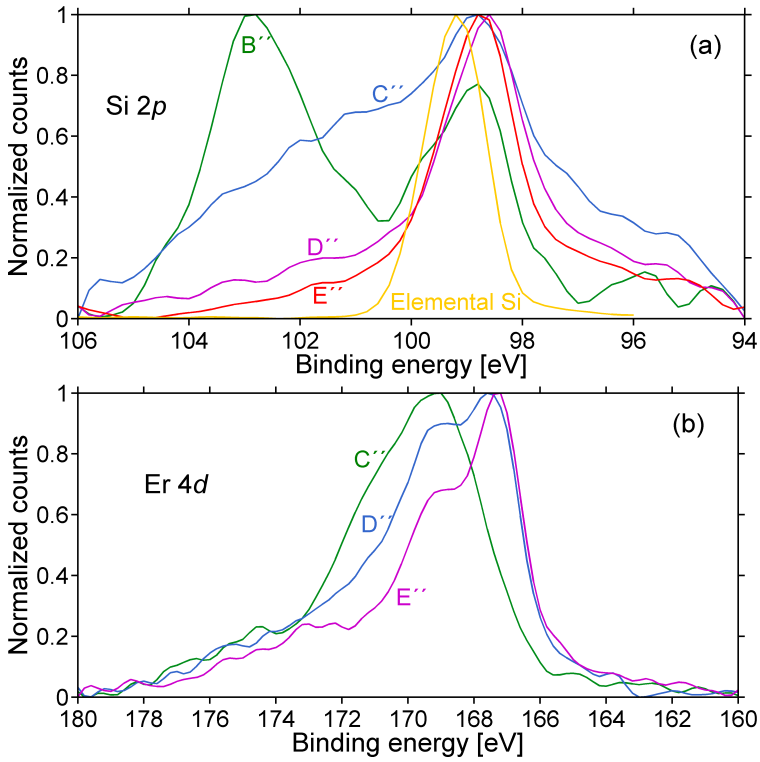

Figure 3.31: Normalized (a) Si 2*p* and (b) Er 4*d* core level spectra after background subtraction for the Ti(15 nm)/Er(25 nm)/Si(100) stack annealed at 600 °C for 2 min with a 2 min pre-RTA purge.

comparison with a-Er/Si. In both Er silicide types, the Er $4d_{5/2}$ signals are very similar and the Er $4d_{5/2}$ BE is fixed to 167.3 eV (Figs. 3.25 and 3.28 versus Fig. 3.32). On the other side, the Er/Si intensity ratio is approximately constant for $ErSi_{2-x}$, contrary to a-Er/Si (Figs. 3.23 and 3.27 versus Fig. 3.30). Another substantial difference is the evolution of the Si 2*p* core level before the detection of the Si substrate (between D" and E"): it is constant (98.7 eV) for $ErSi_{2-x}$ while it raises rapidly for a-Er/Si (E-F versus F'-H'). This difference can be simply explained by the fact that $ErSi_{2-x}$ has a fixed stoechiometry whereas a-Er/Si is characterized by a variable composition.

Finally, the Si substrate is reached in F". It is worth noting that a strong Er signal is still observed at this position due to the knock-on of Er atoms into the Si substrate, as already observed for the two other samples. Once again, at the vicinity with the interface to Si, the

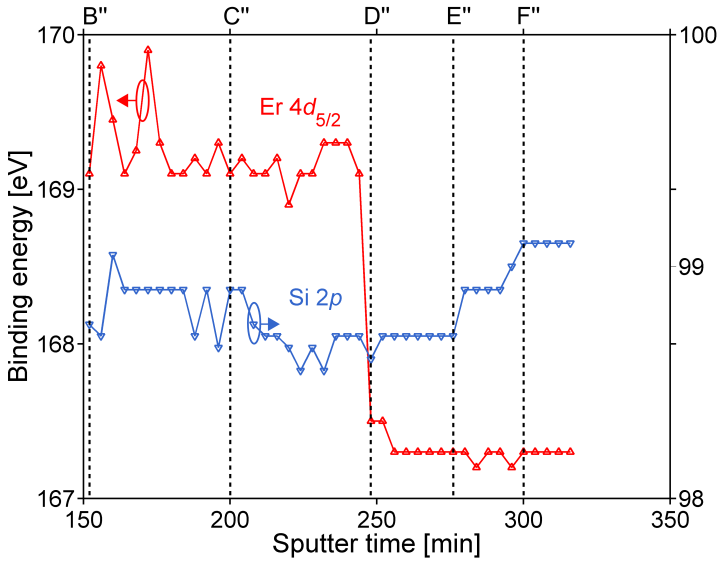

Figure 3.32: Er $4d_{5/2}$ and Si $2s$ BEs for the Ti(15 nm)/Er(25 nm)/Si(100) stack annealed at 600 °C for 2 min with a 2 min pre-RTA purge, from marker B".

silicidation reaction is predominant (D"-F"), as testified by the extraction of a low SBH of 0.3 eV, even if a large oxygen amount diffuses through the Ti cap and oxidizes the top of the $ErSi_{2-x}$ layer (B"-D").

Sample with a 50 nm thick Ti cap annealed with a pre-RTA purge of 2 min In Fig. 3.33, we show the intensity depth profile for the last part of the capping layer only and the $ErSi_{2-x}$ film. The part of the cap in immediate contact with the $ErSi_{2-x}$ film is composed of metallic Ti (from A*) while the top of the cap is as before a mixture of Ti dioxide and suboxides. TEM micrographs in Figs. 3.34(a) and 3.34(b) illustrate the drastic transformation of the Ti cap subjected to RTA at 600 °C. Before annealing (Fig. 3.34(a)), the Ti layer is 50 nm thick and covered by a thin TiO_2 layer (as pointed out for sample 1). After heating, the cap gets considerably thicker (∼90 nm) and is divided into two distinct layers: on the top, TiO_2, and very weakly oxidized Ti at the bottom.

The important result to pinpoint is that we observe no formation of Er oxide due to oxygen diffusion through the Ti cap (Er $4d_{5/2}$ BE = 167.3 eV throughout the $ErSi_{2-x}$ film). This is also confirmed by the examination of the O $1s$ signal which is extinguished after label B*.

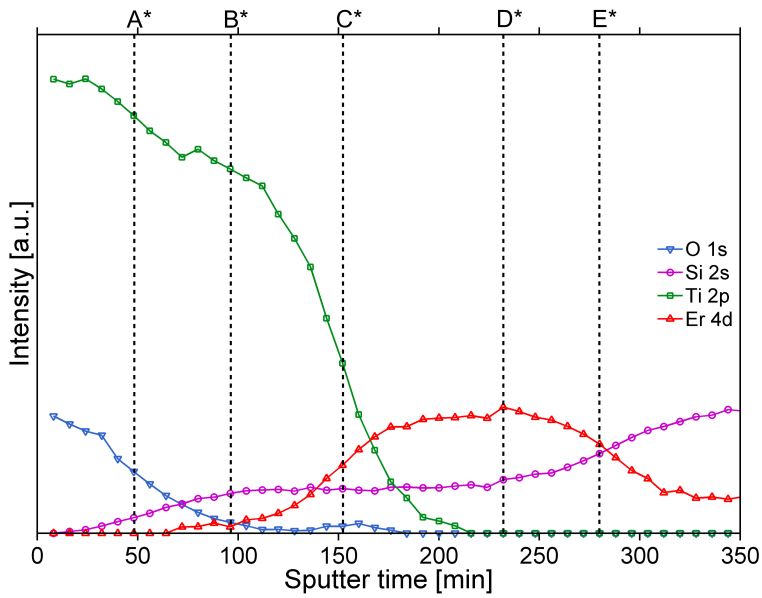

Figure 3.33: XPS intensity depth profile of the Ti(50 nm)/Er(25 nm)/Si(100) stack annealed at 600 °C for 2 min with a 2 min pre-RTA purge. Particular positions along the profile are marked by labels A* to E*.

Still, there is a slight oxygen pile-up between Ti and $ErSi_{2-x}$ (around C*). Most probably, it does not originate from oxygen diffusion but is rather a trace of the pile-up as noted for sample 1. The characteristic doublet of $ErSi_{2-x}$ is observed starting from position C*, is visible and well-defined up to position E*. Over the interval between markers C* and D*, the Si 2*s* BE is centered on ∼149.9 eV. Beyond position D*, the Si 2*s* BE begins to shift towards the BE of elemental Si. The Si substrate is thus probed from that position and is reached in position E* where the Si 2*s* BE matches that of elemental Si (150.5 eV). $ErSi_{2-x}$ is thus present between C* and E*.

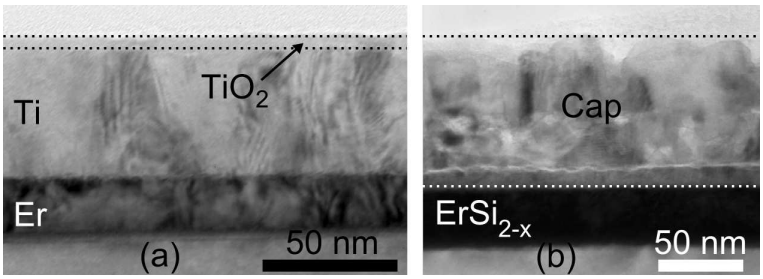

Figure 3.34: TEM micrographs of the Ti(50 nm)/Er(25 nm)/Si(100) stack annealed at 600 °C for 2 min with a 2 min pre-RTA purge.

Sample with a 10 nm thick Ti cap annealed with a pre-RTA purge of 10 min Comparing intensity profiles of Figs. 3.30 and 3.35, it is clearly observed that the Ti oxidation is considerably reduced for a significantly longer purge of 10 min (even for a slightly thinner cap). The corresponding Ti $2p_{3/2}$ BEs are typical of slightly oxidized Ti at the top of the capping layer (454.7 eV) and of elemental Ti deeper into the layer (453.9 eV). In addition, the cap exhibits no volumetric expansion as shown in Fig. 3.35, contrary to samples 3 and 4: the cap thickness is proportional to a sputtering time of 50 min before and after annealing (comparing Figs. 3.23 and 3.35) while the corresponding ST is 150 min for sample 3 (Fig. 3.30). Despite the weak oxidation of the cap, the top of the $ErSi_{2-x}$ layer is still oxidized. As already suggested here above, it is plausible to think that, during the silicidation, a small amount of residual oxygen diffuses into the Ti cap and that Er pumps that oxygen away from the cap, thereby reducing the Ti layer. BEs related to pure $ErSi_{2-x}$ (167.4 eV) are recorded from position A**. In the silicided layer, the Si 2*s* BE is roughly constant (150±0.1 eV) and is characteristic of $ErSi_{2-x}$. From position B**, the Si 2*s* BE starts to shift, meaning that the Si substrate is close. The substrate is reached at marker C** and the interface is located around that position. Table 3.4 summarizes the BEs determined in this work.

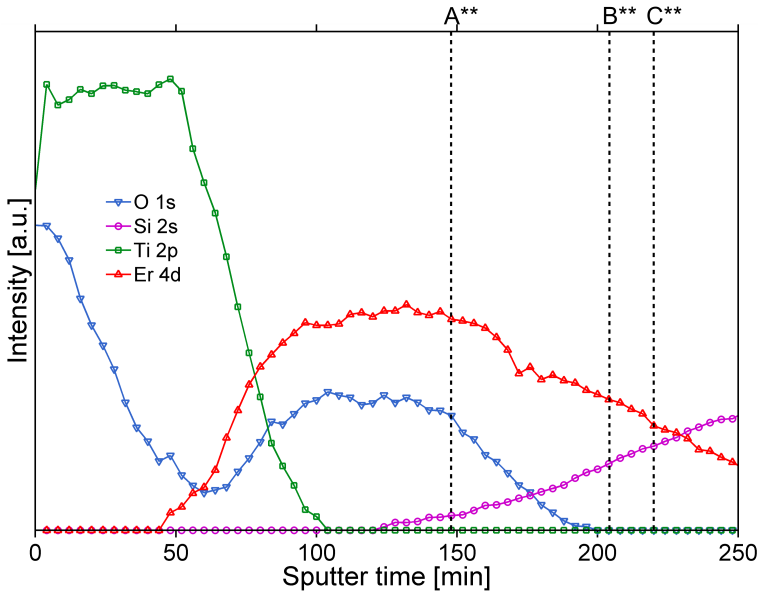

Figure 3.35: XPS intensity depth profile of the Ti(10 nm)/Er(25 nm)/Si(100) stack annealed at 600 °C for 2 min with a 10 min pre-RTA purge. Particular positions along the profile are marked by labels A** to C**.

Peak	Compound	BE [eV]
Er $4d_{5/2}$	Er	167.1
	Er/Si	167.3
	$ErSi_{2-x}$	167.3
	Er oxide	169.1-169.5
O $1s$	Er oxide	531
Si $2s$	Si	150.5
	Er/Si	149.6
	$ErSi_{2-x}$	150.1
Si $2p$	Si	99.1
	Er/Si	98.3
	$ErSi_{2-x}$	98.7

Table 3.4: XPS BEs relevant to Er $4d_{5/2}$, O $1s$, and Si $2p/2s$ core levels from the present work.

3.4.2.1.6 Summary In this section, we carefully examined the XPS depth profile of several samples processed under various conditions. With-

out annealing or for annealing at a low temperature of 300 °C, it was observed that the Er-Si alloy was amorphous and that the silicide/Si interface was not contaminated by oxygen, even though the oxygen penetration was strong at 300 °C. With a thin Ti cap of 15 nm, the annealing at 600 °C resulted in a heavy contamination of the Er silicide surface (probably Er silicate formation). On the other side, the Er silicide film just in contact to Si was preserved, as further testified by a low SBH of 0.3 eV. A much reduced oxygen contamination was obtained if the annealing purge before RTA was prolonged. Moreover, with a much thicker Ti cap of 50 nm, the Er silicide film turned out to be completely free of oxygen. The main conclusion to be drawn from this analysis is that, even though Er silicide could be heavily oxidized, the quality of its contact with Si, represented by the SBH, was always conserved at the optimal annealing temperature (600 °C).

3.4.2.2 Complementary investigations

To study DS with the face-to-face method for SBH extraction, it is not possible to use a mechanical mask anymore, for practical purposes. It is so necessary to use lithography to pattern the diodes with the constraint to maintain a low doping concentration in the Si series resistance R_{Si}, a highly doped region making the SBH extraction impracticable. From that consideration, two solutions emerge.

3.4.2.2.1 Sample preparation The first possibility is to use a mask which will simultaneously define the diodes and protect R_{Si} during the implantation to keep the original dopant concentration to its low level to make the SBH extraction possible. In section 3.3, we have already presented such a method based on HSQ and e-beam lithography. However, this is not convenient for producing a large number of Si wafers. A SiO_2 mask combined to photolithography appears as the simplest solution in that case. Since Er is known to be highly reactive, possibly with SiO_2, we have to check that no conductive path is formed in parallel with R_{Si} at the surface of the SiO_2 layer. The designed optical mask comprises four identical parts allowing to cleave the three-inch wafer in four quadrants (see Fig. 3.36(a)) and to study the variation of one given process parameter (annealing temperature, annealing time, gas of the ambience, etc.). As can be seen in Fig. 3.36(b) showing one quadrant, bare square areas (1×1 and 1.5×1.5 cm^{-2}) are dedicated to physical analysis (XTEM, SIMS, XRD, XPS, etc.). The schematic of Schottky diodes is shown in Fig. 3.36(c). Other structures like four-contact and Hall bars (see Fig. 3.36(d)) are also present for further characterization.

The process is the following: standard cleaning in SPM, oxidation (thick enough to allow for a long HF dip, in case the SiO_2 layer becomes conductive after implantation), photolithography, buffer HF (BHF), etching of SiO_2 in the holes, photoresist removal in SPM, superficial oxide removal in 2% HF (long enough to reach hydrophoby), immediate insertion in the evaporation chamber, evaporation in HV of Er and Ti, silicide growth by RTA, Ti stripping in a mixture composed of NH_4OH+H_2O_2+H_2O (1:1:5) at 70 °C for 5 min (RCA clean). The stripping of the unreacted Er is performed in pure H_2SO_4 at room temperature.

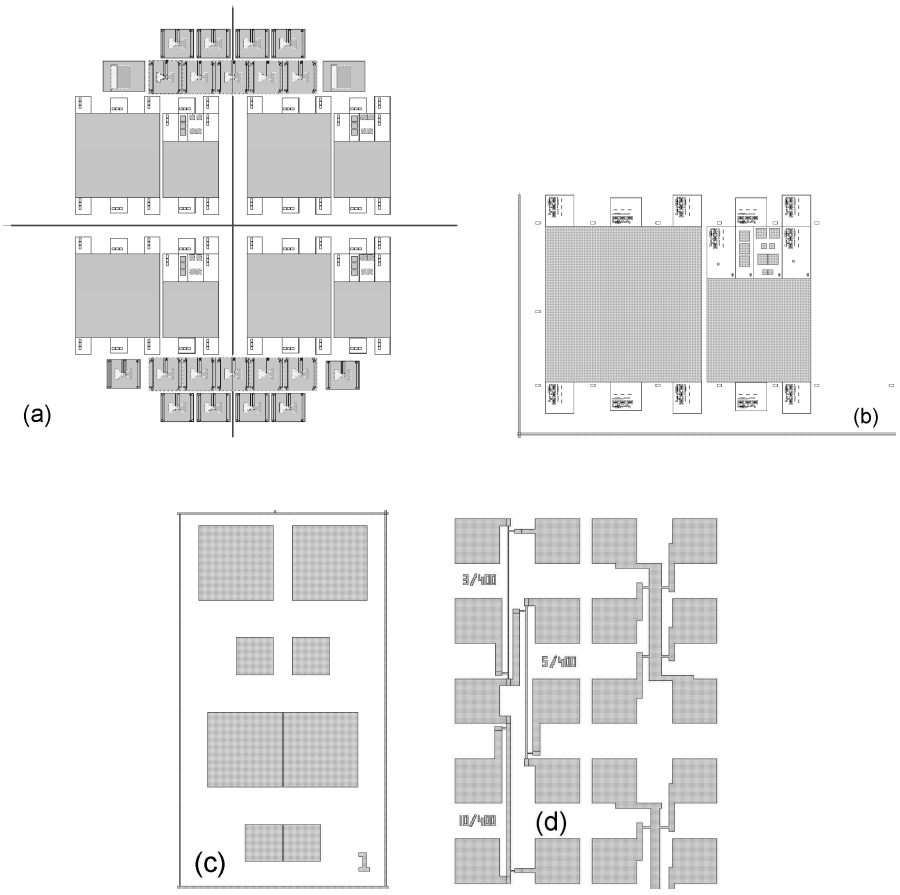

Figure 3.36: Layout of the optical mask designed for silicide characterization: (a) global mask, (b) a quarter of the gobal mask with many test structures, (c) layout of the face-to-face Schottky diodes, and (d) layout of the four-contact resistances and Hall bars.

The second alternative is to form face-to-face Schottky diodes from an already formed $ErSi_{2-x}$ film. We have realized such samples to double-cross the SBH extraction from face-to face diodes formed with the SiO_2 mask (in case there is a short circuit over SiO_2). The related process is quite simple. After stripping the Ti and Er layers, a photolithography is performed with a grid-shaped mask. Then $ErSi_{2-x}$ can be etched in the trenches with either BHF or 2% HF in a few seconds. We could even, if necessary, etch some Si in the trenches with the RCA clean or tetramethylammonium hydroxide since $ErSi_{2-x}$ is absolutely not etched by these chemicals. This is interesting in case the Si gap is implanted since it is then possible to etch Si over the few tens of nanometers where the dopants are concentrated.

In the previous section 3.4.2.1, we have shown that the top of the $ErSi_{2-x}$ silicide film is not contaminated by oxygen for a Ti capping of 50 nm. For that reason, we fix the Ti thickness to that value. The more relevant parameter to test is the annealing temperature. It is varied from 400 to 700 °C with a step of 100 °C.

3.4.2.2.2 Structural analysis After silicidation, the capping layer must be removed selectively with $ErSi_{2-x}$. The formation of $ErSi_{2-x}$ and the efficiency of that stripping is verified by XRD and XTEM. For all annealing temperatures, we identify a strong peak at 27.2°, corresponding to the (100) peak of $ErSi_{2-x}$ (see Fig. 3.37). It is interesting to observe that crystalline $ErSi_{2-x}$ is already formed at such a low temperature as 400 °C. Before stripping, we can also see some peaks related to Ti phases. After stripping, the only visible peak is the $ErSi_{2-x}$(100) one, illustrating the efficiency of the stripping.

The XTEM inspection in Fig. 3.38 reveals that Ti-Si phases are formed for both temperatures and confirms that the capping layer is completely removed, Ti-Si compounds in contact with the $ErSi_{2-x}$ film as well as unreacted or slightly oxidized Ti at the top. The formation of Ti-Si phases is not surprising since Si diffuses towards Er during the formation of $ErSi_{2-x}$ and can diffuse higher in the stack to react with Ti. It is also observed that Er and Ti do not intermix since there is a clear separation between the two layers. After stripping, the 600 °C sample presents some superficial roughness, contrary to the 700 °C sample.

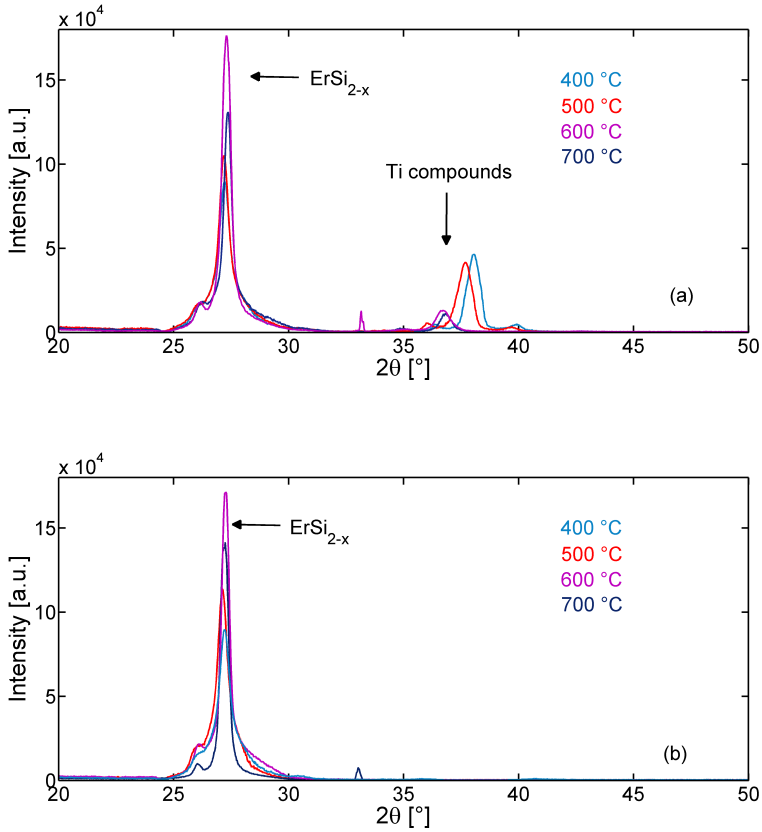

Figure 3.37: XRD spectra for capped $ErSi_{2-x}$ grown by RTA between 400 and 700 °C (a) before and (b) after cap stripping.

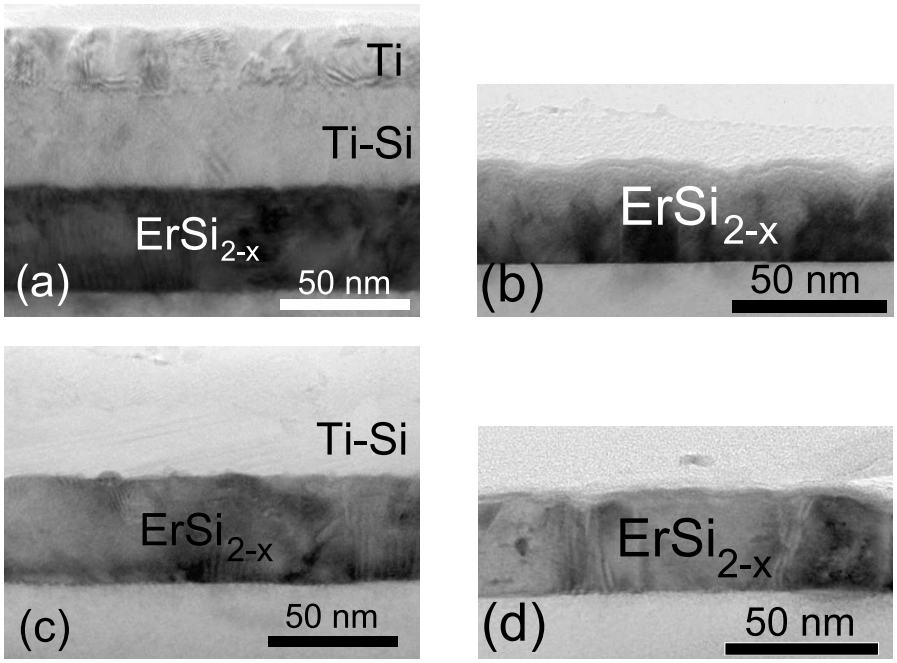

Figure 3.38: TEM pictures for capped $ErSi_{2-x}$ grown by RTA at 600 (a) before and (b) after cap stripping, and at 700 °C (c) before and (d) after cap stripping, respectively.

3.4.2.2.3 Schottky barrier height extraction We also extract the SBH for all annealing temperatures (after stripping of course). The applied bias ranges from 0.1 to 1 V with a step of 0.15 V. The samples are measured from 150 up to 290 K with a step of 20 K. For each annealing temperature, the SBH is measured for four different face-to-face Schottky diodes of different geometries (see Fig. 3.36(c)). The variation of the SBH across the four diodes is found to be very small. Figure 3.39 shows that the extracted SBH is slightly decreasing with the annealing temperature, from 0.315 (at 400 °C) to 0.295 eV (at 700 °C). Once again, it is worth noting the low SBH already attained at 400 °C. As featured in Fig. 3.40, the Arrhenius plots for respective annealings at 400 (fit: solid blue curve, experiment: black circle markers) and 700 °C (fit: solid red curve, experiment: black cross markers) exhibit the expected behavior, testifying to the absence of any short circuit over R_{Si}. Moreover, no difference is observed between the SBH extracted from both types of face-to-face Schottky diodes. A second annealing after capping and Er stripping proves not to cause any degradation of the SBH, a slight improvement is even noted. Finally, the stability over time of $ErSi_{2-x}$ kept in ambient air for approximately one year is established by reproducible electrical characteristics.

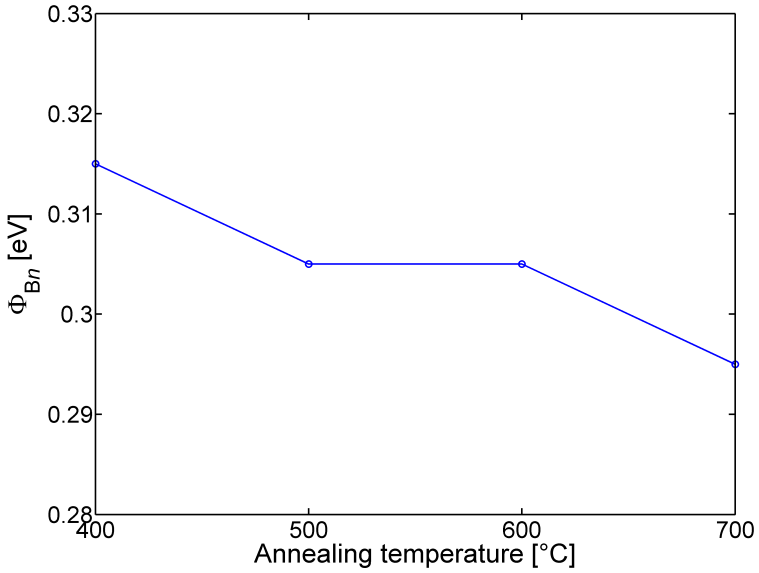

Figure 3.39: SBH of $ErSi_{2-x}$ grown by RTA on n-Si versus the annealing temperature.

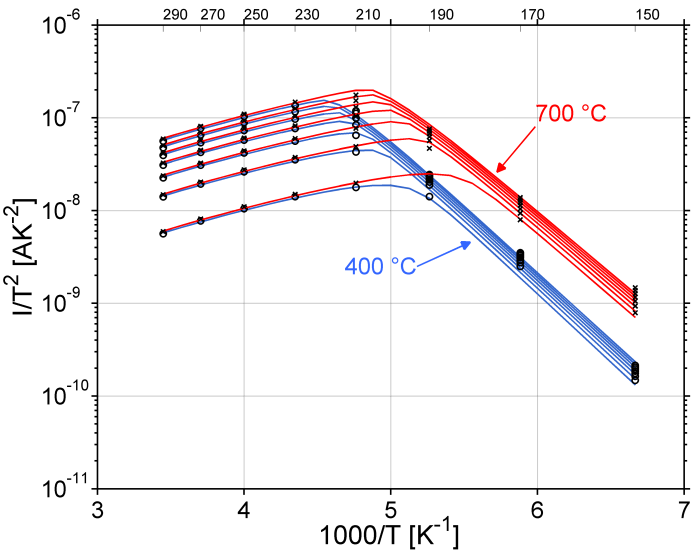

Figure 3.40: Arrhenius plots corresponding to $ErSi_{2-x}$ films grown by RTA on *n*-Si at 400 (fit: solid blue curve, experiment: black circle markers) and 700 °C (fit: solid red curve, experiment: black cross markers), respectively.

3.5 Summary

The third chapter was dedicated to the fabrication and characterization of Er silicide to *n*-Si contacts in various evaporation and growth conditions. At first, the state of the art concerning RE silicides was exhaustively reviewed. The important informations extracted from the literature were that (i) RE silicides are very sensitive to oxygen contamination, (ii) the occurrence of a small oxygen concentration at the MS interface deteriorates their electrical properties, (iii) they are prone to the creation of structural defects of crystallographic nature, and (iv) they present the lowest SBH to electrons (0.28 eV). Next, the investigation of a reference sample deposited and grown in UHV conditions was reported. The formation of crystalline Er silicide was unambiguously identified by XRD for annealing beyond 500 °C. SEM inspection of the film surface highlighted the formation of micrometer-sized pyramidal defects and XPS confirmed that the $ErSi_{2-x}$ layer was not contaminated by oxygen, consistent with a low extracted SBH of 0.295 eV. Thereafter, we assessed the growth of Er silicide with a protective Ti cap (10 nm thick), to alleviate the process constraints inherent to growth in UHV conditions. For evaporation in UHV and *ex situ* annealing, the forma-

tion of crystalline Er silicide was verified for a thermal budget greater than 400 °C. The SBH exhibited a drop upon increasing the annealing temperature (from 300 to 450 °C), a stable value value of 0.28 eV at moderate annealing temperatures (450-500 °C), and a slight augmentation for higher temperatures (600 °C). The SBH drop was attributed to a progressive transformation of amorphous Er silicide into crystalline Er silicide. On the other hand, no clear explanation was found for the slight SBH augmentation but XPS analyses suggested that it could be related to an enhanced oxygen diffusion into the silicide due to high temperature anneal. To further reduce the process complexity, evaporation in HV conditions, still with a Ti cap, was studied. The chemical changes in various types of Ti/Er stacks were scrutinized before and after thermal treatment. It was found that the presence of residual oxygen into the annealing atmosphere resulted in heavily oxidized Er silicide films, irrespective of the annealing temperature (300 or 600 °C). However, the part of the Er silicide film in intimate contact with the Si bulk was invariably free of oxygen, as testified by XPS depth profiling and SBH extraction (0.3 eV), indicating that, even if Er is highly sensitive to oxygen contamination, the formation of its silicide is quite robust. Finally, by depositing a Ti cap of 50 nm over Er, we produced crystalline Er silicide without oxygen contamination and with a low SBH of about 0.3 eV over a large window of formation temperature (400-700 °C).

Chapter 4

Schottky barrier height modulation in Er silicide contacts

The following chapter is devoted to SBH modulation beyond Fermi level pinning. Two principal methods exist to tune the SBH at silicide/Si interfaces: passivation and segregation. The state of the art regarding these two techniques is presented first. Results about the implementation of DS to $ErSi_{2-x}$/n-Si contacts are next exposed.

4.1 Introduction

The passivation technique consists in introducing an extremely thin layer (dielectric, S, Se, etc.) to partially or completely suppress Si interface states and consequently depin the Fermi level. But that method, though elegant, is difficult to implement in MOSFET technology due to reproduciblily issues.

DS, or more generally "impurity segregation", appears as the most promising technique for SBH tuning for CMOS applications. DS consists in piling-up dopant atoms at the silicide-Si interface during the silicide formation. Due to limited dopant solubility in silicides, the dopants are naturally pushed towards the silicide-Si interface. During the process, the impurities are supposed to be activated. As presented before, the current flowing through a Schottky contact is the sum of two contributions: the TE and the FE. When enough dopants are accumulated and activated at the silicide-Si interface, an electric dipole is created, which affects the band bending right at the interface (remember Fig. 1.11(b)). That dipole thins the barrier and promotes the carrier injection by tun-

neling, the TE componant remaining unchanged. In consequence, the SBH is in reality not lowered (or barely) but rather thinned, resulting in an overall lower "effective SBH" (noted Φ_B^{eff}). The effective SBH is no more a SBH properly speaking but it is rather an empirical parameter reflecting how much DS improves tunneling injection.

The DS technique can be declined into three distinct schemes: implant before silicidation (IBS), implant (in)to metal (ITM) and implant (in)to silicide (ITS). The three DS flavors are pictured in Fig. 4.1. As indicated by its denomination, IBS involves the implantation of dopants into the Si substrate, followed by metal deposition, and annealing. The ITM technique consists in implanting dopants in the metal layer and performing the drive-in anneal just after. With the third scheme, the silicide is formed through a first annealing, the dopants implanted into the silicide layer, and segregated towards the Si interface by a second annealing. For all the schemes, it is important to precisely calculate the implantation energy so as to keep the dopant concentration in the Si substrate to a low level (preferably unchanged). Otherwise, we do not perform real DS but we rather form a shallow junction. It is worth noting that the IBS technique is also denominated as "silicidation-induced" DS (SIDS) while ITS is also called "silicide as diffusion source" (SADS).

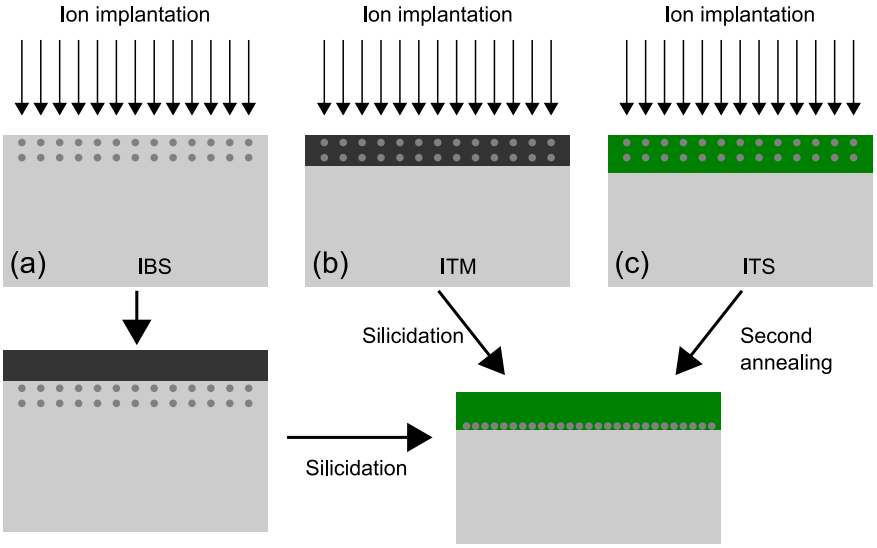

Figure 4.1: The three DS flavors: (a) IBS with implantation, metal deposition, and annealing, (b) ITM IBS with metal deposition, implantation, and annealing, and (c) ITS with implantation into pre-formed silicide followed by annealing.

4.2 State of the art

4.2.1 Passivation

Dangling bonds and strained bonds (see Fig. 4.2(a)) at the surface of a semiconductor create electronic gap states, as seen in chapter 1 section 1.3.2.2. When a metallic layer is deposited on the semiconductor, these surface states (now rather interface states) pin the Fermi level and render the SBH weakly dependent on the metal work function. To restore the Schottky-Mott relationship and, so, to be able to better modulate the SBH, the semiconductor surface states should be "cured" (see Fig. 4.2(b)).

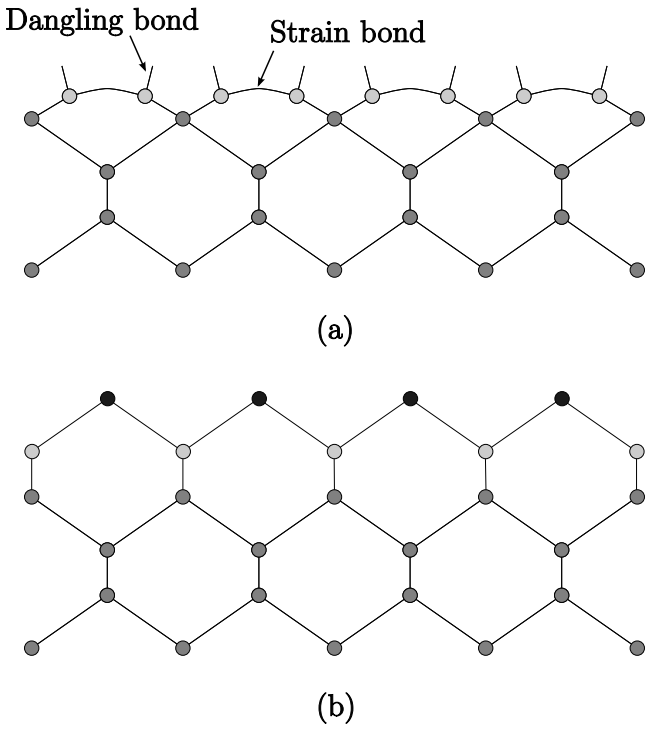

Figure 4.2: Illustration of the VM principle: the Si surface (a) before and (b) after passivation.

Kaxiras [142] introduced the concept of "valence-mending" (VM) to eliminate dangling bonds at the semiconductor surface. In the case of Si(001), S and Se can be used as VM adsorbates. Lacharme *et al.* [143] showed experimentally that surface states at the Si(001) surface can be efficiently removed upon exposure by a S flux at room temperature. Tao

et al. [144] demonstrated ohmic characteristics for a contact between Mg and Si(001). A Se monolayer deposited by molecular beam epitaxy significantly reduced surface states by terminating the dangling bonds and relaxing the strain bonds. In next papers [145–147], the same group applied the method to Al, Cr, and Ti. For Al and Cr [145], they obtained low SBHs, in fair agreement with ideal values given by the Schottky-Mott relationship. For Ti [146, 147], they even claimed observing a negative SBH. This surprising result was further debated in [148, 149].

Another passivation technique involving the interposition of ultrathin insulator layers at the metal/Si interface was proposed by Connelly *et al.* [15]. The optimal thickness of that layer is the result of a trade-off: it must (1) be thick enough to efficiently prevent the penetration of metallic wave functions into Si and to provide a low-defect interface, and, in turn, (2) be sufficiently thin not to yield a substantial tunneling resistance hindering carrier transport. Electrical measurements of Er/SiN_x (SiN_x thickness: 1-2 monolayers) stacks over n- and p-Si matched by simulations gave effective Φ_{Bn}^{eff} and Φ_{Bp}^{eff} of 0.15 eV and 45 meV, respectively. That junction technology was evaluated through the fabrication of metallic S/D MOSFETs based on $Yb/SiN_x/Si$ [15, 16] and $Mg/SiN_x/Si$ [16] stacks. Both types of MOSFETS showed a significant drive current increase (about $\times 20$) compared to a control device without SiN_x, the effect being much more pronounced for Yb. Recently, Coss *et al.* [150] studied the SBH modulation induced by the interfacial dipole between SiO_2 and high-κ dielectrics (LaO_x and AlO_x). The dielectric stack was sandwiched between TaN and n- or p-Si. The tuning proved to be more efficient on p-Si, leading to SBHs of $\sim$0.2 eV for AlO_x and $\sim$1 eV for LaO_x.

4.2.2 Impurity segregation

The main experimental parameters stemming from the publications considered here are regrouped into Table B.1 in appendix B.

The mechanism of DS was first proposed in 1981 by Thornton [151]. The interest in DS has been revived recently, in 2004, by Kinoshita *et al.* [17], to improve the performance of SBMOSFETs by reducing the effective silicide/Si SBH. Their study is the first implementation of the DS technique to modulate the SBH at the source/drain of SBMOSFETs. The transistor, fabricated with $CoSi_2$ S/D, showed a $>$20 % on-current improvement ($\sim$1.3 mA/μm) and better immunity to short-channel effects compared to conventional MOSFETs [17, 152].

For the S/NiSi pair with IBS, Zhao *et al.* [153–155] demonstrated the gradual decrease of the SBH with the increase of the concentration of segregated S at the MS interface. For the highest concentration, Φ_{Bn}

is dramatically reduced from 0.65 to 0.07 eV. The authors argue that the SBH reduction is too strong to attribute to VM. It is suggested that the SBH tuning could rather be the combination of two effects: (1) the work function modification of NiSi due to new chemical bonds with S at the interface and (2) the formation of an interfacial dipole due to the presence of S. The same authors also investigated the redistribution of As and B implanted into Si(100) after Ni silicidation [154] and proved efficient barrier reduction to ∼0.15 eV in both cases. Segregation with S, As, and B was also implemented in the fabrication of SBMOSFETs which exhibit significantly improved performance comparatively to impurity-free SBMOSFETs (higher and lower on- and off-currents, respectively). A very similar investigation to [153] with the same impurity/metal pair over *n*-type Ge(100) substrates has demonstrated the same progressive SBH decrease down to 0.15 eV [156].

In a very interesting theoretical paper, Yamauchi *et al.* [157] shed light on the physical mechanism responsible for the SBH modulation by DS. Based on first-principles calculations, they examined the impact on the SBH of B atoms at substitutional positions at the interface between NiSi and Si. For a dopant-free interface, they revealed the presence of interface states which pin the FL. The energy difference between the CNL of the interface states and the FL gave rise to a dipole. With B doping, the case where a B atom is substituted to a Si atom on the Si side was energetically more favorable. As a consequence, the FL was unpinned, could shift closer the valence band edge and the SBH is drastically reduced. On the other hand, the presence of B on the NiSi side created an opposite dipole which compensates the other one and no SBH tuning was obtained. These theoretical developments were tested experimentally in a following paper [158].

Instead of implanting ions, Wong *et al.* [159] proposed to successively deposit a thin layer of dopant atoms (Sb) and next Ni over *n*-type Si(100). After annealing, Ni was completely converted into NiSi and Sb piled-up at the MS interface, resulting in a very low Φ_{Bn}^{eff} of 0.074 eV. In another paper [160], the same group reports the impact of a high temperature pre-silicidation activation for S and Se implanted in *n*-type Si(100) with the IBS scheme. The conclusion of the study is quite different for each implanted element. In the case of S, a very low Φ_{Bn}^{eff} of ∼0.12 eV was extracted without pre-silicidation anneal while it dramatically increased if the pre-activation anneal was performed because of possible S outdiffusion from Si. On the contrary, for Se, the pre-activation anneal was beneficial since it even resulted in a reduction of Φ_{Bn}^{eff} (from ∼0.25 to ∼0.12 eV). In a sequel paper, Wong *et al.* [161] pursued their study of SBH tuning with Se implantation in *n*-Si(100) substrates for NiSi and

PtSi. Very low Φ_{Bn}^{eff} were obtained for both NiSi (0.083 eV) and PtSi (0.12 eV). Such a strong SBH modulation was attributed to Fermi level pinning very close to the conduction band edge (instead of Fermi level depinning with Se as a VM adsorbates).

Zhang *et al.* and Qiu *et al.* investigated SADS [162, 163] and SIDS [163] for NiSi and PtSi with conventional dopants, to get very low Φ_{Bn}^{eff} (with As and P) and very low Φ_{Bp}^{eff} (with B and In). The SBH was indirectly extracted on wafers of the other doping type for both polarities. It was shown that it is possible to obtain both Φ_{Bn}^{eff} and Φ_{Bp}^{eff} greater than 1 eV, with the appropriate process conditions, regardless of the original PtSi or NiSi SBH.

Larrieu *et al.* [23] evaluated the effect of B segregation on the SBH of PtSi for both ITM and ITS flavors. The ITS scheme provided the lowest effective SBH ($\Phi_{Bp}^{eff} < 0.082$ eV), while ITM resulted in a minor reduction only ($\Phi_{Bp}^{eff} = 0.13$ eV versus 0.145 eV for non-segregated PtSi). This difference was in correlation with the B concentration at the MS interface which was 75% smaller in the ITM case, indicating a possible B outdiffusion during the silicidation. The integration of the ITS method into the fabrication process of SBMOSFETs lead to improved on-current (∼50 % increase), better immunity against short-channel effects, and state-of-the-art high frequency performance (cut-off frequency of 180 GHz).

For the DS to work properly, the implanted dopants must be activated during segregation. To verify the importance of pre-activation for an efficient SBH tuning, Urban *et al.* [164] compared the SBH of NiSi formed by SIDS over activated and non-activated n-Si(100) substrates implanted with As for various doses. The authors found that (1) the SBH modulation was already very efficient for diodes with non-activated dopants since the minimal Φ_{Bn}^{eff} amounted to 0.13 eV and (2) dopant pre-activation lead to a even lower Φ_{Bn}^{eff} of ∼0.09 eV. The technique was successfully applied to the fabrication of SBMOSFETs which showed performance comparable to conventional MOSFETs (on-current of 400 μA/μm and on-current over off-current ratio of 10^9).

Breil *et al.* [165] investigated IBS with PtSi associated to either B or As dopants. The authors studied the impact of pre-activation on the SBH modulation for both types of dopants. In the case of As, the impact of the pre-activation was shown to be negligible (Φ_{Bn}^{eff} ∼0.13 eV) while it was very important for B at low annealing temperatures (decrease of Φ_{Bn} from 0.2 down to 0.055 eV). For B, they also evidenced that plasma doping is a suitable tool to achieve very low effective Φ_{Bp}^{eff} (∼0.08 eV).

Sinha *et al.* [166] reported the NiSi/p-Si SBH tuning with the implan-

tation and segregation of Al. They observed (1) a progressive drop of the SBH with the Al concentration increase and (2) for a given implanted dose, a higher concentration for a thinner NiSi film. Under the optimal conditions (thin NiSi film and high Al concentration), they achieved a very low Φ_{Bp}^{eff} of ∼0.12 eV.

S segregation for the reduction of the PtSi/*n*-Si SBH was investigated in [167]. The authors observed the same behavior as stated previously for NiSi [153], namely the progressive decrease of the SBH with the S implanted dose. A minimal Φ_{Bp}^{eff} of 0.12 eV was reached for the highest dose. Surface passivation and dipole formation (image charge lowering) were precluded as explanatory mechanisms and point rather to work function modification or enhanced tunneling because of traps close to the interface.

The effect of the co-implantation of C and either B or As on the NiSi/Si SBH was assessed by Luo *et al.*. Impurity segregation was performed by IBS and ITS for C and As/B, respectively. For B, the effective SBH was already low enough without C incorporation, which in turn did not result in SBH degradations ($\Phi_{Bn}^{eff} > 0.9$ eV). In contrast, the C+As interplay provided a substantial increase of Φ_{Bp} above 1 eV (against 0.8 eV without C addition) due to an increased As concentration at the interface.

Simulations showed that the SBH reduction by impurity intralayer is all the more efficient that the impurity is electronegative [168]. This fact motivated Loh *et al.* [169] to study the impact of Cl, a strongly electronegative element, on the NiSi/Si SBH. Φ_{Bn}^{eff} was shown to drop linearly with the implanted Cl dose down to 0.08 eV. The authors disclaimed defects generated in the DZ and the doping effect of Cl as the reason for the SBH adjustment and ascribed it rather to interface traps.

For the first time, Larrieu *et al.* [26] explored DS implemented to RE silicides (Er and Yb). With a low thermal budget (500 °C) and an implanted dose amounting to 10^{15} cm^{-2}, both IBS and ITS flavors lead to very low Φ_{Bn}^{eff} (below 0.1 eV) both for $ErSi_{2-x}$ and $YbSi_{2-y}$. The IBS technique coupled to $YbSi_{2-y}$ included into the process flow of SBMOSFETs yielded transistors featuring a spectacular amelioration of the drive current (×10 increase, 252 μA/μm).

Alptekin *et al.* [170] dealt with the SBH lowering induced by DS in the specific case of In associated to NiSi over *p*-Si(100). They observed a linear decrease of Φ_{Bp}^{eff} as a function of the In dose. At best, the SBH amounted to 0.16 eV. As previously [167], they ascribed the SBH tuning to the occurrence of interface states which have, if charged, the effect to concomitantly lower the SB by image force (minor effect), promoting TE injection, and, to thin the SB, promoting tunneling injection (main

effect).

DS allows for solving the main problem associated to the SBMOSFET architecture namely too high SBHs. But, in turn, paradoxically, the use of dopants reintroduces an old issue of nanoscale conventional MOSFETs which is one of the very sources of the interest for SBMOSFETs i.e. the abruptness of the S/D junctions. Feste *et al.* [171] investigated the conditions to obtain very steep segregated doping profiles with highest interfacial dopant concentrations, varying process parameters like the implantation energy, the implantation dose, and the silicide film thickness. The best results were obtained by the combination of low implantation energies and thin silicide films.

Koh *et al.* [172] pursued the previous study [166] of Al segregation in NiSi implementing for the first time "pulsed laser anneal" to contact technology. They focused on scaling down the NiSi thickness and the Al implantation energy. With that technique, they achieved a very low Φ_{Bp}^{eff} of 0.104 eV, with the advantage of low thermal budget provided by pulsed laser anneal.

4.3 Dopant segregation applied to Er silicide

For RE silicides, ITM is only applicable with a capping layer since the vacuum must be broken between the evaporation and the implantation. In effect, it is not acceptable to leave the RE layer exposed to air. IBS and ITS investigations, on the contrary, do not require a capping layer. We use two different t_{Ti} (10 and 50 nm) for a fixed Er thickness t_{Er} (25 nm). Arsenic is chosen as dopant species for implantation doses of 5×10^{14} and 10^{15} cm^{-2}, respectively. For each t_{Ti}, we determine the optimal implantation energy E_I (for a fixed dose) by TRIM [173] under two antagonist constraints: maximizing the dose implanted in the metal and silicon while minimizing the dopant concentration at the interface. Figure 4.3 depicts a typical implantation profile as simulated by TRIM for $t_{Ti} = 10$ nm, $t_{Er} = 25$ nm, a dose of 10^{15} cm^{-2}, and $E_I = 25$ keV. We suppose an Er:Si consumption ratio equal to 1 (the Er:Si consumption ratio is in fact higher than 1 [109] but it is a safety measure). So, for a 25 nm thick Er film, the "future" silicide/Si interface is assumed to be located 25 nm below the Si surface. Of course, the thicker the capping layer, the lesser the dose into the Er layer. We also consider a possible variation of the t_{Er} and t_{Ti}. Table 4.1 shows the interfacial doping concentration and the percentage of the total dose really implanted into the Er and Si layers, for various Ti thicknesses (around 10 nm) and E_I. For the 50 nm thick capping layer, an E_I of

55 keV is chosen and an E_I of 25 keV for the 10 nm thick one. Another advantage of that technique, compared to the others two, is that low or very low implantation energies are not necessary and conventional implantation facilities can be used (at least for As).

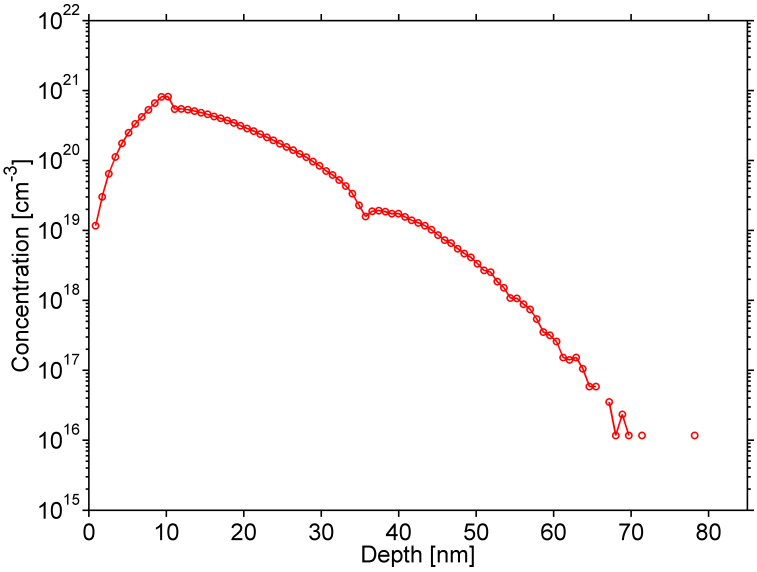

Figure 4.3: As concentration profile simulated by TRIM for $t_{Ti} = 10$ nm, $t_{Er} = 25$ nm, a dose of 10^{15} cm^{-2}, and $E_I = 25$ keV.

t_{Ti} [nm]	t_{Er} [nm]	E_I [keV]	% of total dose in Ti	% of total dose in Er + Si	Concentration at the interface [cm^{-3}]
15	30	25	49	51	$< 5 \times 10^{15}$
10	30	25	30	70	$< 10^{16}$
10	25	25	25	75	$< 10^{17}$
10	25	30	21	79	$< 10^{18}$

Table 4.1: Summary of the percentage of the total As dose implanted in Ti and Er + Si, and upper bound for the interfacial As concentration.

The process is identical to the one described in previous chapters, except for the additional implantation step after the evaporation of the Ti/Er stack. For the 10 nm thick cap, two wafers are processed and evaporated together. For each wafer, four annealing temperatures are taken into account: 400, 500, 600, and 700 °C. Φ_{Bn}^{eff} is extracted for each temperature. The results from the $t_{Ti} = 50$ nm samples are not

exposed here. The effect of SBH modulation is limited because most of the implanted dose is located into the thick Ti capping layer.

Figure 4.4 shows the Arrhenius plots corresponding to the 5×10^{14} cm^{-2} dose for all considered annealing temperatures and for a reference sample without implantation (with $\Phi_{Bn} = 0.3$ eV). For clarity and read-

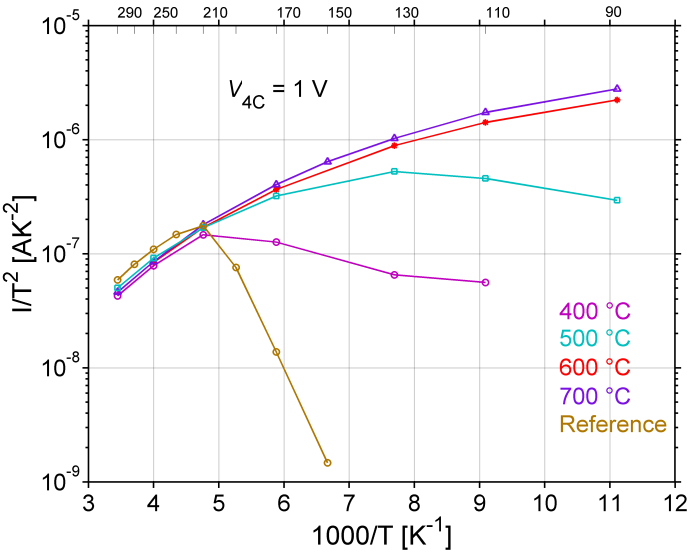

Figure 4.4: Arrhenius plots for the 5×10^{14} cm^{-2} dose for all considered annealing temperatures and for a reference sample without implantation. The curves are displayed for $V_{4C} = 1$ V.

ability, we have only plotted the curves corresponding to $V_{4C} = 1$ V. It can be seen that there is a clear effect for all annealing temperatures, even at 400 °C. The transition temperature decreases progressively with the 400 and 500 °C annealing temperatures, and is no more visible for 600 and 700 °C (at least above 90 K). This reflects a progressive decrease of Φ_{Bn}^{eff}. The effective SBHs are determined to amount to ∼0.25 and ∼0.18 eV at 400 and 500 °C, respectively. If the transition between the ohmic and Schottky regimes cannot be observed, it is only possible to provide an upper bound for the effective SBH. At 600 and 700 °C, the upper bound for Φ_{Bn}^{eff} is determined to be ∼0.13 eV. Nevertheless, it is possible to slightly refine the annalysis by noting that, for a fixed voltage (here $V_{4C} = 1$ V), the current level is higher at 700 °C, probably indicating that the corresponding Φ_{Bn}^{eff} is lower (even though it is not deductible from the fit of the Arrhenius plot). In addition, Fig. 4.5 illustrates that the I-V characteristics are ohmic at 90 K for the 600 and

700 °C samples.

For the 10^{15} cm^{-2} dose, Φ_{Bn}^{eff} is found to be at most 0.12 eV for the 500-700 °C annealing temperature range. The corresponding experimental Arrhenius plots and the fit are revealed in Fig. 4.6. The V_{4C} bias ranges from 0.1 up to 1 V with a step of 0.15 V. Once again, we can observe that the current level at 90 K is higher for a greater annealing temperature.

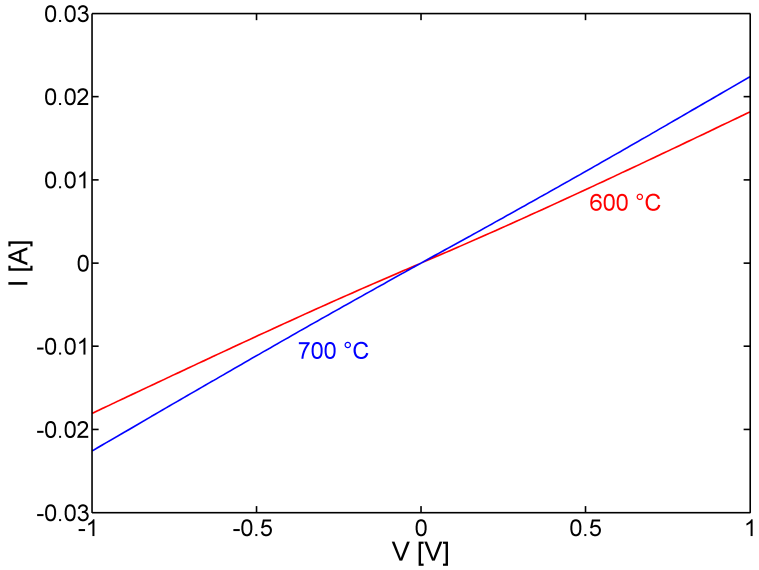

Figure 4.5: I-V characteristics at 90 K for samples annealed at 600 and 700 °C for the 5×10^{14} cm^{-2} dose.

SIMS depth profiling is performed for each dose for the annealing temperatures of 400 and 600 °C to scrutinize the dopant redistribution after annealing. Figures 4.7(a)-4.7(c) display the SIMS depth profiles corresponding to various process conditions. We do not observe a typical segregation peak at the MS interface, even though the impact of dopants on the electrical characteristics is huge. The growing signal intensity at the MS interface is consistent with the decrease of Φ_{Bn}^{eff}. For comparison, unimplanted samples are also sputtered and the As dose is found to be below the detection threshold. The results are consistent with the expected trend, that is a higher interfacial concentration is correlated to a higher annealing temperature or a higher implantation dose.

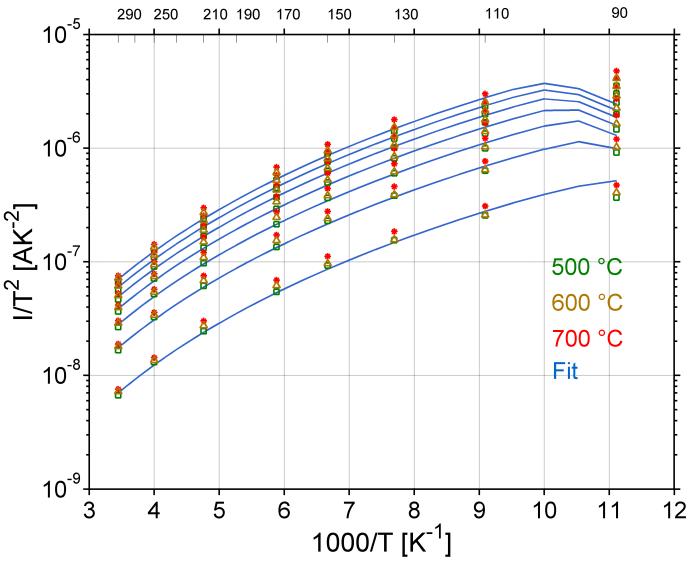

Figure 4.6: Arrhenius plots for the 10^{15} cm^{-2} dose for the 500-700 °C annealing temperature range and the corresponding fit. The V_{4C} bias ranges from 0.1 up to 1 V with a step of 0.15 V.

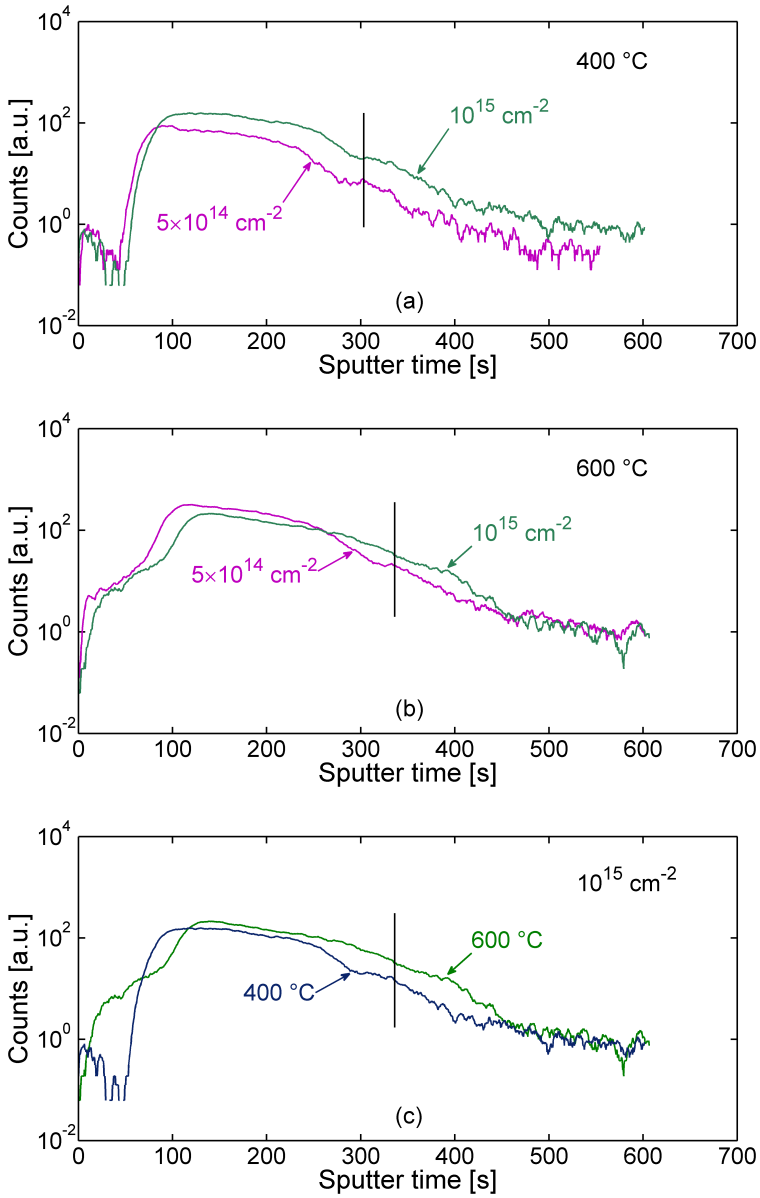

Figure 4.7: SIMS analyses for (a) the 400 °C samples implanted at 5×10^{14} and 10^{15} cm^{-2}, (b) the 600 °C samples implanted at 5×10^{14} and 10^{15} cm^{-2}, and the 400 and 600 °C samples implanted at 10^{15} cm^{-2}. The approximate localization of the MS interface is visualized by a vertical solid black line.

4.4 Low temperature behavior

As observed previously in Fig. 4.4, especially for the 400 and 500 °C samples, after the transition between the ohmic and Schottky regimes, the drop of the Arrhenius plot slope with decreasing T is far from exponential. At low temperature, it appears that there is an excess current compared with the current magnitude predicted by the TFE+BL model. Even if it was not mentioned before in chapter 3, we have also noticed a similar effect during the study of non-segregated silicide/Si contacts at low temperature. In the case of segregated silicide/Si contacts, it turns out that the low temperature deviations from the TFE+BL model (at least, in the considered measurement temperature range, above 77 K) are better evidenced for samples with a weak or moderate effect of DS. We believe that the current in excess might be ascribed to the same physical mechanism in both cases.

To elucidate that low temperature effect, we have considered $ErSi_{2-x}$/n-Si and PtSi/p-Si contacts. For $ErSi_{2-x}$, both segregated and non-segregated face-to-face Schottky diodes are investigated for long Si gaps ($L_{Si} \gg 1$ μm, with L_{Si} the length of the Si gap). For PtSi, both long and short ($L_{Si} \ll 1$ μm) non-segregated two-contact devices are taken into account.

We only take into consideration $ErSi_{2-x}$/n-Si contacts implanted at low doses, exhibiting no or moderate SBH tuning. More interesting, a dramatic disagreement appears at low temperature between the experimental data and the TFE+BL model. This is illustrated in Fig. 4.8(a) displaying the experimental Arrhenius plots for three different kinds of $ErSi_{2-x}$/n-Si contact pairs: (i) non-segregated ($\Phi_{Bn} \approx 0.3$ eV, blue markers, sample 1), (ii) segregated but without SBH tuning ($\Phi_{Bn}^{eff} \approx 0.3$ eV, green markers, sample 2), and (iii) segregated with a moderate SBH reduction ($\Phi_{Bn}^{eff} \approx 0.2$ eV), brown markers, sample 3). The voltage is swept between 0.1 and 1 V with a step of 0.15 V. The corresponding modeled curves are also displayed in plain lines of the same color. A typical Arrhenius plot features two distinct regions marked by a transition temperature: the ohmic region where I is limited by the Si series resistance R_{Si} (positive slope) and the Schottky region where I is limited by the Schottky contacts (negative slope). The temperature at which the transition occurs is indicative of the SBH. The TFE+BL model predicts an exponential drop of I upon decreasing temperature in the Schottky regime, as seen for sample 1. We can see that the fit is excellent for sample 1 at all temperatures while the model is not valid below the transition temperature (230 K) for sample 2. The effect is even stronger for sample 3, below 150 K. The current do decrease below 150 K and the

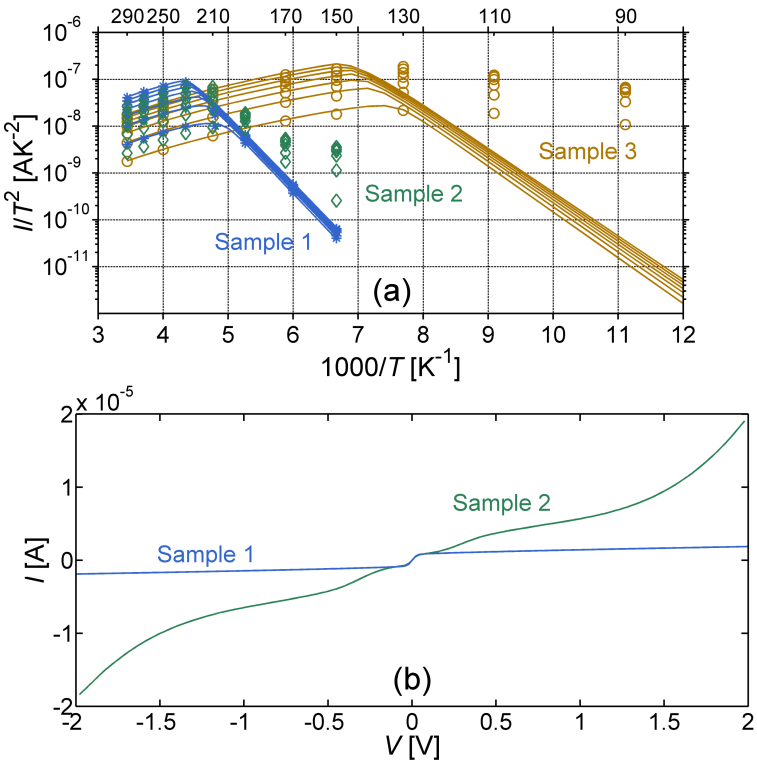

Figure 4.8: (a) Experimental (markers) and modeled (solid curves) Arrhenius plots for $ErSi_{2-x}$ two-contact structures: samples 1, 2, and 3. The fit in the Schottky region is the same for samples 1 and 2. (b) Corresponding I-V characteristics measured at $T = 150$ K for samples 1 and 2.

ohmic-to-Schottky transition occurs but the drop is far from exponential. In Fig. 4.8(b), the disparity is even better highlighted comparing the I-V characteristics at 150 K of samples 1 and 2, respectively. Even though there is no apparent SBH tuning for sample 2, as testified by Fig. 4.8(a), the current injection is visibly somehow influenced by the dopant implantation. In addition, Figs. 4.9(a) and 4.9(b) illustrate that deviations can also be observed at low temperatures ($\leq$ 110 K) for non-segregated PtSi/p-Si devices with a short L_{Si} (250 nm) as opposed to long L_{Si} (25 μm).

In order to explain why I in segregated or short devices increases with V at low temperature, instead of saturating, we perform 2D self-consistent non-equilibrium Green's function (NEGF) simulations. We use a coupled mode space approach assuming transport in the first sub-

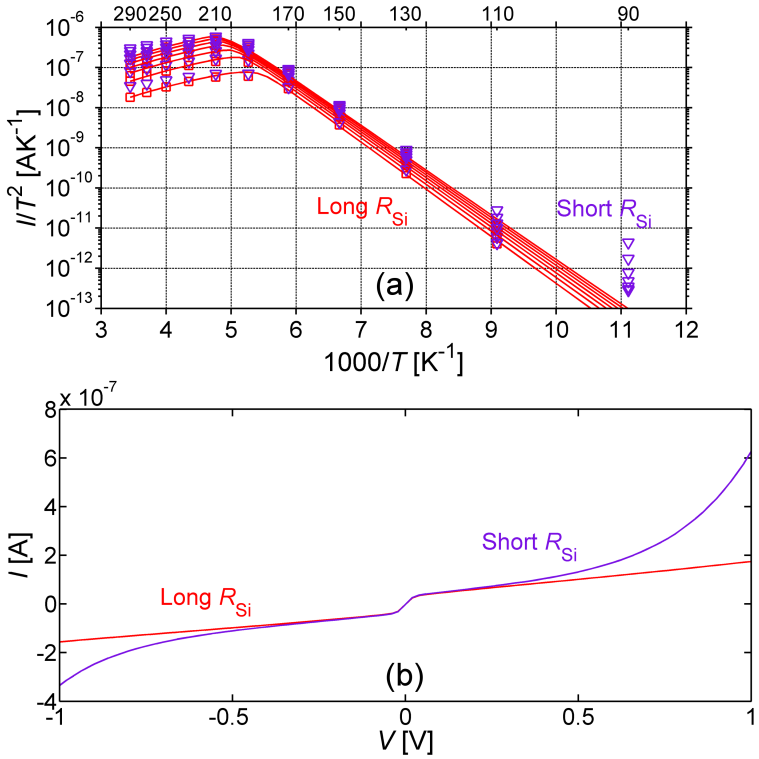

Figure 4.9: (a) Experimental (markers) and modeled (solid curves) Arrhenius plots for PtSi two-contact structures with long and short R_{Si}. (b) Corresponding I-V characteristics measured at $T = 110$ K.

band only, an effective mass Hamiltonian, and ballistic transport approximation [174]. The SB is described as a contact potential [175]. For the DS case, the segregated region in Si is assumed uniformly doped with a concentration $N_{\mathrm{DS}} = 10^{19}$ cm^{-3} with a length $L_{\mathrm{DS}} = 3$ nm [176].

The current spectrum $J(E)$ in a Schottky contact is the result of a competition between occupation of electrons in the metal, mainly a Fermi-Dirac distribution $f_{\mathrm{FD}}(E,T)$ (with E the carrier energy above the Fermi level and T the absolute temperature), and transmission probability of an electron through the barrier $\tau(E)$: $J(E) \approx f_{\mathrm{FD}}(E,T) \times \tau(E)$. The first decreases exponentially above the metal Fermi level for increasing E with a factor depending on the inverse of T: $f_{\mathrm{FD}}(E,T) \propto \exp(-E/kT)$. On the other hand, $\tau(E)$ increases exponentially with a thinner energy-dependent barrier width $d(E)$ ($\tau(E) \propto \exp(-d(E))$) and becomes equal to 1 for $d(E) = 0$ (i.e. above the SB). Moreover, it is weakly dependent on T. In turn, $d(E)$ decreases with E at a rate that

gets steeper with the donor doping N_D: $\partial d/\partial E \propto -N_D$. In consequence, $J(E)$ is lowered in energy with decreasing T, passing from TE over the SB at high T to FE through the SB at low T. In the temperature range considered here, transport essentially occurs via FE.

In Fig. 4.10, the energy band profile (E_C) versus the transport direction x of a short (L_{Si} = 100 nm) segregated $ErSi_{2-x}/n$-Si device at T = 150 K is shown for increasing V. The excess of current at higher V pictured in Fig. 4.8(b) can be linked to the much steeper band profile in the segregated region (inset to Fig. 4.10) compared with the long non-segregated device, owing to a higher doping at the interface. In that case, the profile grows steeper with V, $d(E)$ decreases concomitantly, causing in turn an increase of $\tau(E)$ and I. This variation of the profile slope is not accounted for in the TFE+BL model which supposes a fixed parabolic potential. As can be seen in Fig. 4.11, the corresponding I-V

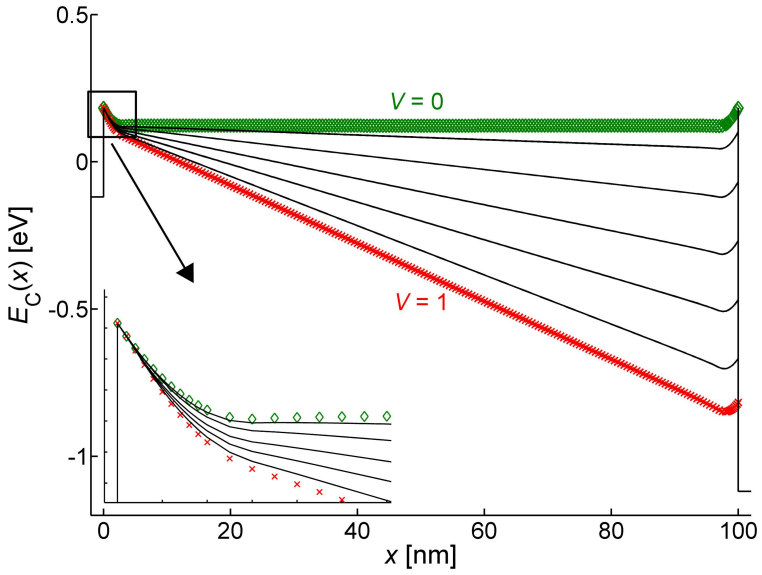

Figure 4.10: Energy band profile of a short segregated $ErSi_{2-x}/n$-Si device at T = 150 K (L_{Si} = 100 nm) given by 2D self-consistent NEGF simulations.

curve renders very well, at least qualitatively, the behavior observed experimentally. The effect is the same for a long device (as featured in Fig. 4.8(a)) since it is only due to the interfacial energy band profile. In addition, as the non-saturation effect of I with V is correlated to the doping profile in the DS area, it could be used to electrically determine important parameters like N_{DS} and L_{DS}, as a substitution or a complement to

physical characterization methods.

In the case of a short non-segregated device, a similar non-saturation effect can also be observed at sufficiently low T, as experimentally shown in Fig. 4.9(b). The reason is that the rate of variation with V of the energy band profile increases compared to a long device because its slope is related to V/L_{Si}. In consequence, similar to the segregated device, for a given T, a V increment causes the band profile to grow more abruptly. Therefore the portion of $J(E)$ under the SB is significantly enhanced (see Fig. 4.12), which leads to an excess of current. In a long non-segregated device, however, the profile variation upon V is negligible. The current spectrum is mostly determined by T, and I mostly saturates with V as expected from the TFE+BL model.

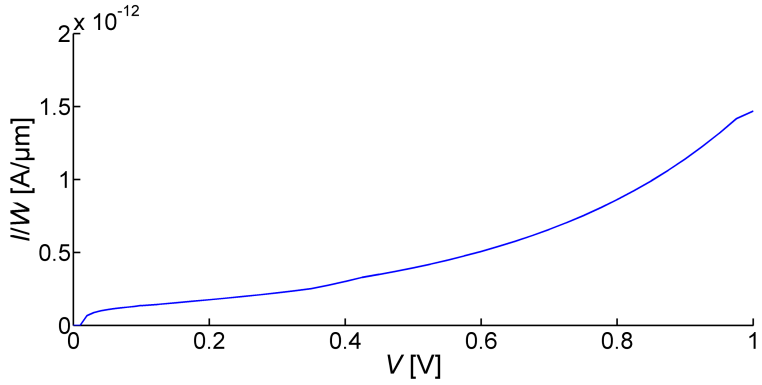

Figure 4.11: 2D self-consistent NEGF simulations of I-V characteristics at $T = 150$ K for a short segregated $ErSi_{2-x}/n$-Si device with $L_{\mathrm{Si}} = 100$ nm, $N_{\mathrm{DS}} = 10^{19}$ cm^{-3}, and $L_{\mathrm{DS}} = 3$ nm.

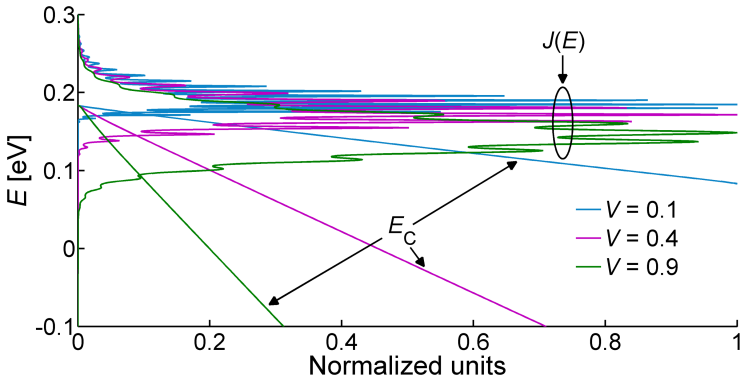

Figure 4.12: 2D self-consistent NEGF simulations of normalized $J(E)$ (rotated by 90°) versus E and E_C versus x/L_{Si} for various V at $T = 150$ K for a short non-segregated $ErSi_{2-x}/n$-Si device. The current spectrum is normalized with respect to its maximum.

4.5 Summary

In this last chapter, the results obtained in chapter 3 were exploited to apply DS to Er silicide contacts over n-Si to further decrease the SBH and create ohmic contacts. In the first section, we gave a detailed state of the art of the recent developments on the realization of ohmic contacts over Si substrates. In the following part, we unveiled the results of DS implementation to Er silicide with the ITM scheme. For a dose of 5×10^{14} cm^{-2}, a progressive decrease of the effective SBH with the annealing temperature was observed, dropping to less than 0.13 eV after anneal at 600 and 700 °C. With implantation at a higher dose of 10^{15} cm^{-2}, the upper bound for the effective SBH was found to amount to 0.12 eV over a large range of annealing temperatures, between 500 and 700 °C. From SIMS depth profiling, it turned out that the SBH diminution was correlated to a higher interfacial dopant concentration, due to either an increase of the implanted dose or to a greater annealing temperature. Finally, through the medium of quantum simulations, we proposed an explanation for the low temperature deviations of I-V characteristics of two-contact silicide/Si structures with respect to the TFE+BL, invoking a dependence of the SB profile on the applied voltage.

Conclusions and perspectives

The present thesis covered many aspects of the study of a particular material, Er silicide. The compound was formed in various environments and conditions, and, remarkably, presented very similar characteristics, electrical as well as structural, even though Er silicide is a material difficult to fabricate compared with other silicides due to oxidation issues. Many physical characterization tools like SEM, TEM, XPS, XRD, and SIMS have been utilized to get a picture as complete as possible. In addition, the structural characterization was systematically coupled to electrical measurements in order to establish mutual correlations. The contraints on the silicide growth were progressively relaxed, starting from UHV deposition and *in situ* growth until HV deposition and growth *ex situ* in a controlled atmosphere. Finally, the expertise acquired from the previous studies was applied to the successful implementation of dopant-segregated Er silicide contacts on low doping n-Si exhibiting excellent ohmic characteristic.

Before developing the core of the present work, chapter 1 was intended as an exposure of the theoretical background of MS contacts. From the very beginning of MS contact studies, large discrepancies were revealed between the theoretical predictions of Schottky and Mott and a host of experimental results. These departures from the Schottky-Mott theory found expression in Fermi level pinning, i.e. a weak dependence of the SBH on the metal work function regardless of the underlying physical mechanism. The main preoccupation of the MS contact theory consists in providing a physical foundation to Fermi level pinning, essentially invoking the presence of gap states or more recently the intrinsic physico-chemical properties of the MS interface. Fermi level pinning also involves that most MS contacts are rectifying. In the last part of chapter 1, we presented two approaches to obtain ohmic contacts.

Chapter 2 dealt with the modeling of the current transport through Schottky diodes. The main outcomes of the conduction models were exploited to present the principal methods for SBH extraction. A new method of SBH determination, extensively used in the present work,

particularly appropriate to (very) low SBH determination was finally exposed. In a second part, chapter 2 also briefly detailed the working principle of the considered physical characterization techniques and the experimental setup for SBH extraction.

The very core of the present thesis is contained in chapters 3 and 4, dedicated to Er silicide growth and characterization, and implementation of DS to $ErSi_{2-x}$/*n*-Si contacts, respectively. To yield reference films, Er silicide was first grown in UHV conditions to limit oxygen contamination. The resulting compound was found to present a low SBH to electrons in very good agreement with the state of the art (0.28 eV). The small-scale morphology of the film proved to be very smooth even though large-size pyramidal defects were observed. The next step of the investigation implied the addition of a Ti capping layer over the Er film, the deposition still taking place in UHV conditions. The formation of Er silicide was considered over a large range of annealing temperatures. Below the threshold of crystalline Er silicide growth, Er silicide in close contact with the Si interface was amorphous, even at room temperature. Besides, we showed that the SBH of Er silicide contacts to low doping *n*-Si exhibits a strong variation with the annealing temperature, dropping substantially with silicide crystallization. In the absence of interfacial contamination by oxygen, it turned out that this dependence originated from the progressive transformation of the Er silicide film under thermal annealing, from an amorphous to a crystalline state, leading to the formation of crystalline $ErSi_{2-x}$. Beyond the threshold for $ErSi_{2-x}$ formation, the grown films exhibited a flat and smooth interface. Even though the top of the $ErSi_{2-x}$ layer was contaminated by oxygen due to the limited impermeability of the thin Ti capping layer, the interface with Si was apparently preserved. The SBH showed a slight increase with the growth temperature that could be correlated to a tiny (undetected) oxygen contamination of the interface and/or roughness. A further step towards less stringent process conditions was to perform the evaporation in HV conditions. The emphasis was put on the study of the competition between oxidation and silicidation of the Er film under various process conditions. A solution involving a thicker Ti capping layer resulted in non-contaminated films. Notably, regardless of the evaporation and growth conditions, the SBH of $ErSi_{2-x}$/*n*-Si contacts systematically amounted to $\sim$0.3 eV for the optimal growth temperature, in excellent agreement with the state of the art.

Even though we have been able to produce Er silicide films with good morphological and electrical properties in not too strict conditions, the SBH of these films on *n*-Si was not sufficiently low for SBMOSFET applications. To go below the limit of 0.3 eV, the DS technique with the

ITM scheme was implemented. Dopant redistribution at the Si/silicide interface was highlighted and correlated to a SBH modulation. The SBH tuning was all the more strong that the temperature of growth of $ErSi_{2-x}$ and/or the implanted dose was high. At best, with a moderate thermal budget, the objective of an effective SBH of about 0.1 eV was reached. It was also observed that the low temperature electrical behavior of two-contact silicide/Si structures diverged from the one expected from the TFE+BL model. By means of quantum simulations, these deviations were ascribed to the modulation of the SB profile by the applied bias.

As a conclusion, we can affirm that this thesis paves the way to potential integration of $ErSi_{2-x}$ in the process of SBMOSFETs. Many supplementary studies could complement the achieved work: (1) investigation of the other two DS schemes, IBS and ITM, (2) use of other doping species or impurities, (3) exploration of other implantation techniques like plasma doping or δ-doping, (4) DS study with acceptor dopants like B for very low SBHs to holes, with the perspective of CMOS integration with a single silicide, (5) impact of the impurity implantation on the physical properties of $ErSi_{2-x}$ (morphology, temperature of formation, alloying, etc.), influence on the formation of structural defects, etc. In addition, we think that the methodology employed throughout the work could be applied to the complete exploration of other silicides or other materials.

In more general terms, interesting future work relying on the present experience would be to study the silicidation of Si nanostructures, for instance Si nanowires. As already evoked in the introduction of this thesis, the formation of ohmic contacts is a key element to provide a reliable interface between the nano- and the macro-world. Based on such building-blocks, interesting fundamental properties of Si nanowires, like their piezoresistance, magnetoresistance, thermoelectric power etc., could be studied. Si nanowires also have potential applications in spintronics, nanoFETs, highly sensitive biosensors, quantum computing with spin qubits in quantum dots etc.

Appendix A

Derivation of the current expression in the Crowell and Rideout model

Let us first calculate an analytical expression for $\tau(E)$ for $E < E_{\mathrm{BB}}$. Considering the parabolic potential of equation (1.3), the electron potential energy can be expressed as:

$$\frac{q^2 N_{\mathrm{D}}(x')^2}{2\epsilon_{\mathrm{SC}}}.$$

With the following definitions:

$$E = \frac{q^2 N_{\mathrm{D}} x^2}{2\epsilon_{\mathrm{SC}}},$$
$$E_{\mathrm{BB}} = \frac{q^2 N_{\mathrm{D}} w^2}{2\epsilon_{\mathrm{SC}}},$$

$\tau(E)$ can be written as:

$$\exp\Big[\frac{-4\pi}{h}\int_x^w \Big(2m^*(\frac{q^2 N_{\mathrm{D}}(x')^2}{2\epsilon_{\mathrm{SC}}} - E)\Big)^{1/2}\Big]\mathrm{d}x'.$$

The integral can be rewritten in a more concise manner as (with $A^2 = \frac{2\epsilon_{\mathrm{SC}}E}{q^2 N_{\mathrm{D}}}$ and $B = \sqrt{\frac{m^* q^2 N_{\mathrm{D}}}{\epsilon_{\mathrm{SC}}}}$):

$$B\int_x^w \Big(\sqrt{(x')^2 - A^2}\Big)\mathrm{d}x'.$$

The primitive of the function $\sqrt{(x')^2 - A^2}$ can be calculated analytically:

$$F(x') = \frac{1}{2}x'\sqrt{(x')^2 - A^2} - \frac{A^2}{2}\ln\Big(x' + \sqrt{(x')^2 - A^2}\Big) + \mathrm{cte}.$$

Let us evaluate the definite integral $F(w) - F(x)$:

$$\begin{aligned} F(w) &= \frac{1}{2} w\sqrt{w^2 - A^2} - \frac{A^2}{2} \ln\Big(w + \sqrt{w^2 - A^2}\Big) \\ &= \frac{1}{2} w^2 \sqrt{1 - \frac{A^2}{w^2}} - \frac{A^2}{2} \ln\Big(w + w\sqrt{1 - \frac{A^2}{w^2}}\Big) \\ &= \frac{1}{2} w^2 \Big\{ \sqrt{1 - \frac{A^2}{w^2}} - \frac{A^2}{w^2} \ln\Big(w(1 + \sqrt{1 - \frac{A^2}{w^2}})\Big)\Big\} \\ &= \frac{1}{2} w^2 \Big\{ \sqrt{1 - \alpha} - \alpha \ln\Big(w(1 + \sqrt{1 - \alpha})\Big)\Big\}. \end{aligned}$$

Since $x^2 = A^2$:

$$\begin{aligned} F(x) &= -\frac{A^2}{2} \ln(x) \\ &= -\frac{1}{2} \alpha w^2 \ln(w\sqrt{\alpha}). \end{aligned}$$

So, finally:

$$\begin{aligned} \tau(E) &= \exp\Big[-\frac{4\pi}{h}(F(w) - F(x))\Big] \\ &= \exp\Big[-\frac{4\pi}{h}\frac{1}{2} w^2 \Big\{ \sqrt{1 - \alpha} - \alpha \ln\Big(w(1 + \sqrt{1 - \alpha})\Big) \\ &+ \alpha \ln(w\sqrt{\alpha})\Big\}\Big] \\ &= \exp\Big[-\frac{E_{\mathrm{BB}}}{E_{00}} \Big\{ \sqrt{1 - \alpha} - \alpha \ln\Big(\frac{1 + \sqrt{1 - \alpha}}{\sqrt{\alpha}}\Big)\Big\}\Big] \\ &= \exp\Big[-\frac{E_{\mathrm{BB}}}{E_{00}} y(\alpha)\Big]. \end{aligned}$$

Substituting the final expression for $\tau(E)$ in equation (2.3), we find:

$$\begin{aligned} J_{\mathrm{F}} = \frac{A^* T}{k} \int_0^{E_{\mathrm{BB}}} f_{\mathrm{SC}}(E) \exp\Big[-\frac{E_{\mathrm{BB}}}{E_{00}} y(\alpha)\Big] \mathrm{d}E \\ + \frac{A^* T}{k} \int_{E_{\mathrm{BB}}}^{+\infty} f_{\mathrm{SC}}(E) \mathrm{d}E. \end{aligned}$$

With f_{SC} given by equation (2.4), J_{F} becomes:

$$
\begin{aligned}
J_{\mathrm{F}} &= \frac{A^{*}T}{k}\int_{0}^{E_{\mathrm{BB}}}\exp(\frac{-qV_{\mathrm{N}}-E}{kT})\exp\Big[-\frac{E_{\mathrm{BB}}}{E_{00}}y(\alpha)\Big]\mathrm{d}E \\
&+ \frac{A^{*}T}{k}\int_{E_{\mathrm{BB}}}^{+\infty}\exp(\frac{-qV_{\mathrm{N}}-E}{kT})\mathrm{d}E \\
&= A^{*}T^{2}\exp(-\frac{qV_{\mathrm{N}}}{kT})\frac{1}{kT}\Big[\int_{0}^{E_{\mathrm{BB}}}\exp(-\frac{E}{kT})\exp\Big[-\frac{E_{\mathrm{BB}}}{E_{00}}y(\alpha)\Big]\mathrm{d}E \\
&+ \int_{E_{\mathrm{BB}}}^{+\infty}\exp(-\frac{E}{kT})\mathrm{d}E\Big].
\end{aligned}
$$

With the previous definition of J_{m} (equation (2.5)) and a change of variable ($E \rightarrow \alpha$), we have:

$$
\begin{aligned}
\frac{J_{\mathrm{F}}}{J_{\mathrm{m}}} &= \frac{1}{kT}\Big(\int_{0}^{1}\exp(-\frac{\alpha E_{\mathrm{BB}}}{kT})\exp\Big[-\frac{E_{\mathrm{BB}}}{E_{00}}y(\alpha)\Big]E_{\mathrm{BB}}\mathrm{d}\alpha \\
&+ \int_{1}^{+\infty}\exp(-\frac{\alpha E_{\mathrm{BB}}}{kT})E_{\mathrm{BB}}\mathrm{d}\alpha\Big) \\
&= \frac{E_{\mathrm{BB}}}{kT}\Big(\int_{0}^{1}\exp\Big[-\frac{E_{\mathrm{BB}}}{kT}(\alpha+\frac{kT}{E_{00}}y(\alpha))\Big]\mathrm{d}\alpha \\
&+ \int_{1}^{+\infty}\exp(-\frac{E_{\mathrm{BB}}}{kT}\alpha)\mathrm{d}\alpha\Big).
\end{aligned}
$$

Appendix B

Summary of references about dopant segregation

Reference	Technique	Scheme	Metal	Substrate	Impurity	Dose (cm^{-2})	Energy (keV)	SBH min /max (eV)	Extraction method
[17]	II	IBS	Co	n-Si(100)	As	10^{15}	1		
[152]	II	IBS	Co	n-Si(100)	As	10^{15}	1		
[153]	II	IBS	Ni	n,p-Si(100)	S	10^{13} to 2×10^{14}	15	0.07	IVT
[154]	II	IBS	Ni	n,p-Si(100)	S	10^{13} to 2×10^{14}	15	0.07	IVT
	II				As	5×10^{13} to 10^{15}	5	0.14	IVT
	II				B	5×10^{13} to 10^{15}	5	NM	IVT
[156]	II	IBS	Ni	n,p-Ge(100)	S	5×10^{13} to 10^{15}	10	0.15	IVT
[157]	II	ITS	Ni	p-Si(100)	B	NM	10	0.4	NM
[158]	II	IBS,ITS	Ni	n,p-Si(100)	As,B,Mg	NM	NM	?	IVT
[155]	II	IBS	Ni	n-Si(100)	S	10^{14} and 5×10^{14}	50	NA	NA
[162]	II	SADS	Ni	n-Si(100)	B	10^{15}	4.5	0.96	CV
	II	SADS	Ni	n-Si(100)	In	10^{15}	25	0.76	CV
	II		Ni	p-Si(100)	As	10^{15}	25	0.85	
	II		Ni	p-Si(100)	P	10^{15}	10	0.9	
	II		Pt	n-Si(100)	B	10^{15}	4.5	1	
	II		Pt	n-Si(100)	In	10^{15}	25	1.05	
	II		Pt	p-Si(100)	As	10^{15}	25	0.96	
	II		Pt	p-Si(100)	P	10^{15}	10	0.92	

Reference	Technique	Scheme	Metal	Substrate	Impurity	Dose (cm^{-2})	Energy (keV)	SBH min /max (eV)	Extraction method
[159]	ID	NA	Ni	n-Si(100)	Sb	NA	NA	0.074	IVT
[23]	II	ITM	Pt	p-Si(100)	BF_2	10^{15}	20	0.13	IVT2
	II	ITS	Pt	p-Si(100)	BF_2	10^{15}	20	$<$0.082	IVT2
[160]	II	IBS	Ni	n-Si(100)	S	2×10^{14}	15	$\sim$0.13	IVT
	II		Ni	n-Si(100)	Se	2×10^{14}	15	$\sim$0.12	IVT
[163]	II	SADS							
	II	SIDS	Ni	n-Si(100)	B	10^{15}	1	1.01	CV
	II		Ni	p-Si(100)	As	10^{15}	7	1.05	
	II		Pt	n-Si(100)	B	10^{15}	1	1.01	
	II		Pt	p-Si(100)	As	10^{15}	7	1.05	
[164]	II	IBS	Ni	n-Si(100)	As	5×10^{13} to 10^{15}	5	$\sim$0.1	IVT
[165]	II	IBS	Pt	p-Si(100)	As	10^{15}	1	0.15	IVT2
	II				BF_2	10^{15}	1	0.055	IVT2
	PLAD				BF_3	10^{15} and 5×10^{15}	NA	0.08	IVT2
[166]	II	IBS	Ni	p-Si(100)	Al	10^{13} to 2×10^{14}	10	0.12	IVT
[161]	II	IBS	Ni	n-Si(100)	Se	10^{13} to 2×10^{14}	10	0.083	IVT
			Pt	n-Si(100)	Se	10^{13} to 2×10^{14}	10	0.12	IVT

Reference	Technique	Scheme	Metal	Substrate	Impurity	Dose (cm^{-2})	Energy (keV)	SBH min /max (eV)	Extraction method
[167]	II	IBS	Pt	*n*-Si(100)	S	10^{13} to $\times 10^{14}$	5	0.12	IV
[177]	II	IBS	Ni	*p*-Si(100)	(1) C	10^{15} and 5×10^{15}	5		CV
					(2) As	10^{15}	5	0.98	
	II	IBS	Ni	*n*-Si(100)	(1) C	10^{15} and 5×10^{15}	5		
					(2) B	10^{15}	5	1.02	
[169]	II	IBS	Ni	*n*-Si(100)	Cl	10^{13} to 10^{15}	3 to 10	0.08	IVT
				p-Si(100)				0.54	IVT
[26]	II	IBS	Er,Yb	*n*-Si(100)	As	3×10^{13} and 10^{15}	1	<0.1	IVT2
	II	ITS		*n*-Si(100)	As	10^{15}	20	<0.08	IVT2
[170]	II	IBS	Ni	*p*-Si(100)	In	10^{13} to 10^{14}	10	0.16	IV
[171]	II	IBS	Ni	*n*-Si	As	5×10^{13} to $\times 10^{15}$	1 to 10	0.12	IVT
[172]	II	IBS	Ni	*p*-Si(100)	Al	5×10^{13} to 10^{16}	1.5	0.104	IVT

Table B.1: Experimental parameters gathered from publications related to DS.

Bibliography

[1] Semiconductor Industry Association. *International Technology Roadmap for Semiconductors*, 2003.

[2] J. M. Larson and J. P. Snyder. Overview and status of metal S/D Schottky-barrier MOSFET technology. *IEEE Transactions on Electron Devices*, 53:1048–1058, 2006.

[3] J. Kedzierski, P. Xuan, E. H. Anderson, J. Bokor, T.-J. King, and C. Hu. Complemetary silicide source/drain thin-body MOSFETs for the 20 nm gate length regime. In *IEEE International Electron Device Meeting Technical Digest*, pages 57–60, 2000.

[4] E. Dubois and G. Larrieu. Measurement of low Schottky barrier heights applied to metallic source/drain metal-oxide-semiconductor field effect transistors. *Journal of Applied Physics*, 96:729–737, 2004.

[5] G. Larrieu and E. Dubois. Schottky-barrier source/drain MOSFETs on ultrathin SOI body with a tungsten metallic midgap gate. *IEEE Electron Device Letters*, 25:801–803, 2004.

[6] M. Fritze, C. L. Chen, S. Calawa, D. Yost, B. Wheeler, P. Wyatt, C. L. Keast, J. Snyder, and J. Larson. High-speed Schottky-barrier pMOSFET with $f_T = 280$ GHz. *IEEE Electron Device Letters*, 25: 220–222, 2004.

[7] G. Larrieu and E. Dubois. Integration of PtSi-based Schottky-barrier p-MOSFETs with a midgap tungsten gate. *IEEE Transactions on Electron Devices*, 52:2720, 2005.

[8] M. Jang, J. Oh, S. Maeng, W. Cho, S. Lee, K. Kang, and K. Park. Characteristics of erbium-silicided n-type Schottky barrier tunnel transistors. *Applied Physics Letters*, 83:2611–2613, 2003.

[9] M. Jang, S. Lee, and K. Park. Erbium silicided n-type Schottky barrier tunnel transistors for nanometer regime applications. *IEEE Transactions on Nanotechnology*, 2:205–209, 2003.

[10] S. Zhu, H. Y. Yu, J. D. Chen, S. J. Whang, J. H. Chen, C. Shen, C. Zhu, S. J. Lee, M. F. Li, D. S. H. Chan, W. J. Yoo, A. Du, C. H. Tung, J. Singh, A. Chin, and D. L. Kwong. Low temperature MOSFET technology with Schottky barrier source/drain, high-K gate dielectric and metal gate electrode. *Solid-State Electronics*, 48:1987–1992, 2004.

[11] S. Zhu, J. Chen, M.-F. Li, S. J. Lee, J. Singh, C. X. Zhu, A. Du, C. H. Tung, A. Chin, and D. L. Kwong. N-type Schottky barrier source/drain MOSFET using ytterbium silicide. *IEEE Electron Device Letters*, 25:565–567, 2004.

[12] E. J. Tan, K.-L. Pey, N. Singh, G.-Q. Lo, D. Z. Chi, Y. K. Chin, K. M. Hoe, G. Cui, and P. S. Lee. Demonstration of Schottky barrier NMOS transistors with erbium silicided source/drain and silicon nanowire channel. *IEEE Electron Device Letters*, 29:1167–1170, 2008.

[13] D. Connelly, C. Faulkner, and D. E. Grupp. Performance advantage of Schottky source/drain in ultrathin-body silicon-on-insulator and dual-gate CMOS. *IEEE Transactions on Electron Devices*, 50:1340–1345, 2003.

[14] D. Connelly, C. Faulkner, and D. E. Grupp. Optimizing Schottky S/D offset for 25-nm dual-gate CMOS performance. *IEEE Electron Device Letters*, 24:411–413, 2003.

[15] D. Connelly, C. Faulkner, D. E. Grupp, and J. S. Harris. A new route to zero-barrier metal source/drain MOSFETs. *IEEE Transactions on Nanotechnology*, 3:98–104, 2004.

[16] D. Connelly, C. Faulkner, P. A. Clifton, and D. E. Grupp. Fermi-level depinning for low-barrier Schottky source/drain transistors. *Applied Physics Letters*, 88:012105, 2006.

[17] A. Kinoshita, Y. Tsuchiya, A. Yagishita, K. Uchida, and J. Koga. Solution for high-performance Schottky-source/drain MOSFETs: Schottky barrier height engineering with dopant segregation technique. In *Symposium on VLSI Technology*, pages 168–169, 2004.

[18] B.-Y. Tsui and C.-P. Lin. A Novel 25-nm modified Schottky-barrier finFET with high performance. *IEEE Electron Device Letters*, 25: 430–432, 2004.

[19] J. Knoch, M. Zhang, Q. T. Zhao, St. Lenk, S. Mantl, and J. Appenzeller. Effective Schottky barrier lowering in silicon-on-insulator Schottky-barrier metal-oxide-semiconductor field-effect transistors using dopant segregation. *Applied Physics Letters*, 87:263505, 2005.

[20] H.-S. Wong, A. T.-Y. Koh, H.-C. Chin, L. Chan, G. Samudra, and Y.-C. Yeo. Source and drain series resistance reduction for N-channel transistors using solid antimony (Sb) segregation (SSbS) during silicidation. *IEEE Electron Device Letters*, 29:756–758, 2008.

[21] H.-S. Wong, L. Chan, G. Samudra, and Y.-C. Yeo. Selenium segregation for lowering the contact resistance in ultrathin-body MOSFETs with fully metallized source/drain. *IEEE Electron Device Letters*, 30:1087–1089, 2009.

[22] M. Sinha, E. F. Chor, and Y.-C. Yeo. Nickel-silicide contact technology with dual near-band-edge barrier heights and integration in CMOS finFETs with single mask. *IEEE Electron Device Letters*, 31:918–920, 2010.

[23] G. Larrieu, E. Dubois, R. Valentin, N. Breil, F. Danneville, G. Dambrine, and J.-P. Raskin J.-C. Pesant. Low temperature implementation of dopant-segregated band-edge metallic S/D junctions in thin-body SOI *p*-MOSFETs. In *IEEE International Electron Device Meeting Technical Digest*, pages 147–150, 2007.

[24] Z. Zhang, Z. Qiu, P.-E. Hellström, G. Malm, J. Olsson, J. Lu, M. Östling, and S.-L. Zhang. SB-MOSFETs in UTB-SOI featuring PtSi source/drain with dopant segregation. *IEEE Electron Device Letters*, 29:125–127, 2008.

[25] V. Gudmundsson, P.-E. Hellström, J. Luo, J. Lu, S.-L. Zhang, and M. Östling. Fully depleted UTB and trigate N-channel MOSFETs featuring low-temperature PtSi Schottky-barrier contacts with dopant segregation. *IEEE Electron Device Letters*, 30:541–543, 2009.

[26] G. Larrieu, D. A. Yarekha, E. Dubois, N. Breil, and O. Faynot. Arsenic-segregated rare-earth silicide junctions: reduction of

Schottky barrier and integration in metallic n-MOSFETs on SOI. *IEEE Electron Device Letters*, 30:1266–1268, 2009.

[27] F. Braun. Uber die Stromleitung durch schwefelmetalic. *Annalen der Physik and Chemie*, 153:556–563, 1874.

[28] W. Schottky. Zur Halbleitertheorie der Sperrschicht- und Spitzengleichrichter. *Zeitschrift für Physik*, 113:367–414, 1939.

[29] N. F. Mott. The theory of crystal rectifiers. *Proceedings of the Royal Society of London*, 171(944):27–38, 1939.

[30] N. F. Mott. Note on the contact between a metal and an insulator or semi-conductor. *Mathematical Proceedings of the Cambridge Philosophical Society*, 34:568–572, 1938.

[31] W. Schottky. Abweichungen vom ohmschen gesetz in halbleitern. *Physikalische Zeitschrift*, 41:570–573, 1940.

[32] J. Bardeen. Surface states and rectification at a metal semiconductor contact. *Physical Review*, 71:717–727, 1947.

[33] A. M. Cowley and S. M. Sze. Surface states and barrier height of metal-semiconductor systems. *Journal of Applied Physics*, 36: 3212–3220, 1965.

[34] V. Heine. Theory of surface states. *Physical Review*, 138:A1689–A1696, 1965.

[35] S. G. Louie and M. L. Cohen. Electronic structure of a metal-semiconductor interface. *Physical Review B*, 13:2461–2469, 1976.

[36] C. Tejedor, F. Flores, and E. Louis. The metal-semiconductor interface: Si (111) and zincblende (110) junctions. *Journal of Physics C: Solid State Physics*, 10:2163–2177, 1977.

[37] J. Tersoff. Schottky barrier heights and the continuum of gap states. *Physical Review Letters*, 52:465–468, 1984.

[38] W. E. Spicer, P. W. Chye, P. R. Skeath, C. Y. Su, and I. Lindau. New and unified model for Schottky barrier and III-V insulator interface states formation. *Journal of Vacuum Science and Technology B*, 16:1422–1433, 1979.

[39] H. Hasegawa and H. Ohno. Unified disorder induced gap state model for insulator-semiconductor and metal-semiconductor interfaces. *Journal of Vacuum Science and Technology B*, 4:1130–1138, 1986.

[40] W. Mönch. Barrier heights of real Schottky contacts explained by metal-induced gap states and lateral inhomogeneities. *Journal of Vacuum Science and Technology B*, 17:1867–1876, 1999.

[41] R. T. Tung. Chemical bonding and Fermi level pinning at metal-semiconductor interfaces. *Physical Review Letters*, 84:6078–6081, 2000.

[42] S. M. Sze and K. K. Ng. *Physics of semiconductor devices*. Wiley, third edition, 2007.

[43] M. S. Tyagi. *Introduction to semiconductor materials and devices*. Wiley, second edition, 1991.

[44] J.-P. Colinge and C. A. Colinge. *Physics of semiconductor devices*. Kluwer, 2002.

[45] D. K. Schröder. *Semiconductor material and device characterization*. Wiley, 1990.

[46] H. Mathieu. *Physique des semiconducteurs et des composants électroniques*. Masson, quatrième edition, 1998.

[47] W. Mönch. *Electronic properties of semiconductor interfaces*. Wiley, second edition, 2004.

[48] W. A. Harrison. *Electronic structure and the properties of solids: the physics of the chemical bond*. Dover, 1989.

[49] W. Schottky. Vereinfachte und erweiterte Theorie der Randschicht-gleichrichter. *Zeitschrift für Physik*, 118:539–592, 1941.

[50] R. T. Tung. Recent advances in Schottky barrier concepts. *Materials Science and Engineering R*, 35:1–138, 2001.

[51] C. M. Osburn and K. R. Bellur. Low parasitic resistance contacts for scaled ULSI devices. *Thin Solid Films*, 332:428–436, 1998.

[52] F. A. Padovani and R. Stratton. Field and thermionic-field emission in Schottky barriers. *Solid-State Electronics*, 9:695–707, 1966.

[53] H. H. Berger. Models for contacts to planar devices. *Solid-State Electronics*, 15:145–158, 1972.

[54] H. A. Bethe. Theory of the boundary layer of crystal rectifier. *MIT Radiation Laboratory Report*, 43:12–23, 1942.

[55] C. R. Crowell and V. L. Rideout. Normalized thermionic-field emission in metal-semiconductor (Schottky) barriers. *Solid-State Electronics*, 12:89–105, 1969.

[56] R. H. Fowler. The analysis of photoelectric sensitivity curves for clean metals at various temperatures. *Physical Review*, 38:45–56, 1931.

[57] W. Massa. *Crystal structure determination*. Springer, second edition, 2004.

[58] S. Hüfner. *Photoelectron spectroscopy - principles and applications*. Springer, third edition, 2003.

[59] B. Fultz and J. M. Howe. *Transmission electron microscopy and diffractometry of materials*. Springer, third edition, 2008.

[60] J. Y. Duboz, P. A. Badoz, F. Arnaud d'Avitaya, and J. A. Chroboczek. Electronic transport properties of epitaxial erbium silicide/silicon heterostructures. *Applied Physics Letters*, 55:84–86, 1989.

[61] M. H. Unewisse and J. W. V. Storey. Conduction mechanisms in erbium silicide Schottky diodes. *Journal of Applied Physics*, 73: 3873–3879, 1993.

[62] J. A. Knapp and S. T. Picraux. Epitaxial growth of rare-earth silicides on (111) Si. *Applied Physics Letters*, 48:466–468, 1986.

[63] J. E. Baglin, F. M. d'Heurle, and C. S. Petersson. The formation of silicides from thin films of some rare-earth metals. *Applied Physics Letters*, 36:594–596, 1980.

[64] R. D. Thompson, B. Y. Tsaur, and K. N. Tu. Contact reaction between Si and rare earth metals. *Applied Physics Letters*, 68: 535–537, 1981.

[65] P. Muret, T. A. Nguyen Tan, N. Frangis, and J. Van Landuyt. Unpinning of the Fermi level at erbium silicide/silicon interfaces. *Physical Review B*, 56:9286–9289, 1997.

[66] W. C. Tsai, K. S. Chi, and L. J. Chen. Growth of pinhole-free epitaxial Yb and Er silicide thin films on atomically clean (111)Si. *Journal of Applied Physics*, 96:5353–5356, 2004.

[67] E. J. Tan, M. L. Kon, K. L. Pey, P. S. Lee, Y. W. Zhang, W. D. Wang, and D. Z. Chi. Effects of Si(001) surface amorphization on $ErSi_2$ thin film. *Thin Solid Films*, 504:157–160, 2006.

[68] C. S. Wu, S. S. Lau, T. F. Kuech, and B. X. Liu. Surface morphology and electronic properties of $ErSi_2$. *Thin Solid Films*, 104: 175–182, 1983.

[69] G. H. Shen, J. C. Chen, C. H. Luo, S. L. Cheng, and L. J. Chen. The growth of pinhole-free epitaxial $DySi_{2-x}$ films on atomically clean Si(111). *Journal of Applied Physics*, 84:3630–3635, 1998.

[70] B. Y. Tsaur and L. S. Hung. Ion-beam-induced modification of silicide formation in rare-earth metals: Er-Si and Tb-Si systems. *Applied Physics Letters*, 37:922–924, 1980.

[71] Y.-L. Jiang, Q. Xie, C. Detavernier, R. L. Van Meirhaeghe, G.-P. Ru, X.-P. Qu, and B.-Z. Li. Growth of pinhole-free ytterbium silicide film by solid-state reaction on Si(001) with a thin amorphous Si interlayer. *Journal of Applied Physics*, 102:033508, 2007.

[72] K. N. Tu, R. D. Thompson, and B. Y. Tsaur. Low Schottky barrier of rare-earth silicide on *n*-Si. *Applied Physics Letters*, 38:626–628, 1981.

[73] R. D. Thompson, K. N. Tu, and G. Ottaviani. Phase transformations of alloys on a reactive substrate: Interaction of binary alloys of transition and rare-earth metals with silicon. *Journal of Applied Physics*, 58:705–710, 1985.

[74] H. Norde, J. de Sousa Pires, F. d'Heurle, F. Pesavento, S. Petersson, and P. A. Tove. The Schottky-barrier height of the contacts between some rare-earth metals (and silicides) and *p*-type silicon. *Applied Physics Letters*, 38:865–867, 1981.

[75] S. S. Lau, C. S. Pai, C. S. Wu, T. F. Kuech, and B. X. Liu. Surface morphology of erbium silicide. *Applied Physics Letters*, 41:77–80, 1982.

[76] J. E. E. Baglin, F. M. d'Heurle, and C. S. Petersson. Diffusion marker experiments with rare-earth silicides and germanides: Relative mobilities of the two atom species. *Journal of Applied Physics*, 52:2841–2846, 1981.

[77] J. A. Knapp, S. T. Picraux, C. S. Wu, and S. S. Lau. Erbium silicide formation using a line-source electron beam. *Applied Physics Letters*, 44:747–749, 1984.

[78] J. A. Knapp, S. T. Picraux, C. S. Wu, and S. S. Lau. Kinetics and morphology of erbium silicide formation. *Journal of Applied Physics*, 58:3747–3757, 1985.

[79] M. A. Taubenblatt, D. Thomson, and C. R. Helms. Interface effects in titanium and hafnium Schottky barriers on silicon. *Applied Physics Letters*, 44:895–897, 1984.

[80] C. S. Wu, D. M. Scott, and S. S. Lau. The effect of an interfacial oxide layer on the Schottky barrier height of Er-Si contact. *Journal of Applied Physics*, 58:1330–1334, 1985.

[81] C. S. Wu, A. Ghaemmaghami, and S. S. Lau. Effect of the presence of Ge in Er compound on the barrier height formation of Er-Si contacts. *Journal of Applied Physics*, 58:1601–1605, 1985.

[82] J. A. Knapp and S. T. Picraux. Epitaxial formation of rare earth silicides by rapid annealing. In *Materials Research Society Symposium Proceedings*, volume 54, pages 261–266, 1986.

[83] M. Gurvitch, A. F. J. Levi, R. T. Tung, and S. Nakahara. Epitaxial yttrium silicide on (111) silicon by vacuum annealing. *Applied Physics Letters*, 51:311–313, 1987.

[84] M. P. Siegal, F. H. Kaatz, W. R. Graham, J. J. Santiago, and J. Van der Spiegel. Formation of epitaxial yttrium silicide on (111) silicon. *Journal of Applied Physics*, 66:2999–3006, 1989.

[85] M. P. Siegal, W. R. Graham, and J. J. Santiago-Aviles. Growth of pinhole-free epitaxial yttrium silicide on Si(111). *Journal of Applied Physics*, 68:574–580, 1990.

[86] T. L. Lee and L. J. Chen. Formation of amorphous interlayers in ultrahigh vacuum deposited yttrium thin films on (111)Si. *Journal of Applied Physics*, 73:5280–5282, 1993.

[87] L. J. Chen. Solid state amorphization in metal/Si systems. *Materials Science and Engineering R*, 29:115–152, 2000.

[88] F. Arnaud d'Avitaya, A. Perio, J.-C. Oberlin, Y. Campidelli, and J. A. Chroboczek. Fabrication and structure of epitaxial Er silicide films on (111) Si. *Applied Physics Letters*, 54:2198–2200, 1989.

[89] I. Sagnes, G. Vincent, and P. A. Badoz. Transport and near-infrared optical properties of $ErSi_2$ thin films. *Journal of Applied Physics*, 72:4295–4299, 1992.

[90] P. L. Janega, J. McCaffrey, and D. Landheer. Extremely low resistivity erbium ohmic contacts to *n*-type silicon. *Applied Physics Letters*, 55:1415–1417, 1989.

[91] P. Muret, T. T. A. Nguyen, N. Frangis, G. Van Tendeloo, and J. Van Landuyt. Photoelectric and electrical responses of several erbium silicide/silicon interfaces. *Applied Surface Science*, 102: 173–177, 1996.

[92] M. G. Grimaldi, X. Yan, G. Scerra, S. Ravesi, and C. Spinella. Influence of oxygen on the formation of epitaxial erbium silicide film on <111>Si. *Applied Physics Letters*, 67:974–976, 1995.

[93] G. Kaltsas, A. Travlos, N. Salamouras, A. G. Nassiopoulos, P. Revva, and A. Traverse. Erbium silicide films on (100) silicon, grown in high vacuum. Fabrication and properties. *Thin Solid Films*, 275:87–90, 1996.

[94] G. Kaltsas, A. Travlos, A. G. Nassiopoulos, N. Frangis, and J. Van Landuyt. High crystalline quality erbium silicide films on (100) silicon, grown in high vacuum. *Applied Surface Science*, 102:151–155, 1996.

[95] N. Frangis, J. Van Landuyt, G. Kaltsas, A. Travlos, and A. G. Nassiopoulos. Growth of erbium-silicide films on (100) silicon as characterised by electron microscopy and diffraction. *Journal of Crystal Growth*, 172:175–182, 1997.

[96] A. Travlos, N. Salamouras, and E. Flouda. Epitaxial erbium silicide films on (100) silicon: growth, structure and electrical properties. *Applied Surface Science*, 120:355–364, 1997.

[97] D. Tsamakis, M. Vlachos, A. Travlos, and N. Salamouras. Electrical properties of crystalline Er and Dy silicide layers. *Thin Solid Films*, 418:211–214, 2002.

[98] C. H. Luo and L. J. Chen. Growth kinetics of amorphous interlayers and formation of crystalline silicide phases in ultrahigh vacuum deposited polycrystalline Er and Tb thin films on (001)Si. *Journal of Applied Physics*, 82:3808–3814, 1997.

[99] J. C. Chen, G. H. Shen, and L. J. Chen. Growth kinetics of amorphous interlayers by solid-state diffusion in ultrahigh vacuum deposited polycrystalline Gd thin films on (001)Si. *Journal of Applied Physics*, 84:6083, 1998.

[100] A. Travlos, N. Salamouras, and N. Boukos. Growth of rare earth silicides on silicon. *Journal of Physics and Chemistry of Solids*, 64: 87–93, 2003.

[101] E. J. Tan, M. Bouville, D.g Z. Chi, and K. L. Pey. Pyramidal structural defects in erbium silicide thin films. *Applied Physics Letters*, 88:021908, 2006.

[102] E. J. Tan, K. L. Pey, D. Z. Chi, P. S. Lee, and L. J. Tang. Improved electrical performance of erbium silicide Schottky diodes formed by pre-RTA amorphization of Si. *IEEE Electron Device Letters*, 27: 93–95, 2006.

[103] Y.-L. Jiang, Q. Xie, C. Detavernier, R. L. Van Meirhaeghe, G.-P. Ru, X.-P. Qu, B.-Z. Li, A. Huang, and P. K. Chu. Oxidation suppression in ytterbium silicidation by Ti/TiN bicapping layer. *Journal of Vacuum Science and Technology A*, 25:285–289, 2007.

[104] W. Huang, G. P. Ru, Y. L. Jiang, X. P. Qu, B. Z. Li, R. Liu, and F. Lu. Erbium silicide formation and its contact properties on Si(100). *Journal of Vacuum Science and Technology B*, 26:164–263, 2008.

[105] W. Huang, G. P. Ru, Y. L. Jiang, X. P. Qu, B. Z. Li, and R. Liu. Improvement of Er-silicide formation on Si(100) by W capping. *Thin Solid Films*, 516:4252–4257, 2008.

[106] M. Jun, M. Jang, Y. Kim, C. Choi, T. Kim, S. Oh, and S. Lee. Analysis of temperature-dependent barrier heights in erbium-silicided Schottky diodes. *Journal of Vacuum Science and Technology B*, 26:137–140, 2008.

[107] M. Jun, Y. Kim, C. Choi, T. Kim, S. Oh, and M. Jang. Schottky barrier heights of n/p-type erbium-silicided Schottky diodes. *Microelectronic Engineering*, 85:1395–1398, 2008.

[108] M. Q. Huda and K. Sakamoto. Use of $ErSi_2$ in source/drain contacts of ultra-thin SOI MOSFETs. *Materials Science and Engineering B*, 89:378–381, 2002.

[109] Y. Kim, M. Jang, J. Shin, and S. Lee. Analysis of the erbium silicide growth mechanism on SOI for n-type SB-MOSFETs. *Journal of Korean Physical Society*, 45:1322–1326, 2004.

[110] S. L. Liew, B. Balakrisnan, S. Y. Chow, M. Y. Lai, W. D. Wang, K. Y. Lee, C. S. Ho, T. Osipowicz, and D. Z. Chi. Growth of high quality Er-Ge films on Ge(001) substrates by suppressing oxygen contamination during germanidation annealing. *Thin Solid Films*, 504:81–85, 2006.

[111] Q. F. Daphne Yiew, Y. Setiawan, P. S. Lee, and D. Z. Chi. Erbium silicidation on SiGe for advanced MOS application. *Thin Solid Films*, 504:91–94, 2006.

[112] N. Reckinger, X. Tang, V. Bayot, D. A. Yarekha, E. Dubois, S. Godey, X. Wallart, G. Larrieu, A. Łaszcz, J. Ratajczak, P. J. Jacques, , and J.-P. Raskin. Low Schottky barrier height for $ErSi_{2-x}$/n-Si contacts formed with a Ti cap. *Journal of Applied Physics*, 104:103523, 2008.

[113] N. Reckinger, X. Tang, V. Bayot, D. A. Yarekha, E. Dubois, S. Godey, X. W., G. Larrieu, A. Łaszcz, J. Ratajczak, P. J. Jacques, and J.-P. Raskin. Schottky barrier lowering with the formation of crystalline Er silicide on n-Si upon thermal annealing. *Applied Physics Letters*, 94:191913, 2009.

[114] C. H. Luo and L. J. Chen. Interfacial reactions of ultrahigh vacuum deposited Er-Si multilayer thin films. *Applied Surface Science*, 113/114:556–561, 1997.

[115] X. Tang, J. Katcki, E. Dubois, N. Reckinger, J. Ratajczak, G. Larrieu, P. Loumaye, O. Nisole, and V. Bayot. Very low Schottky barrier to n-type silicon with PtEr-stack silicide. *Solid-State Electronics*, 47:2105–2111, 2003.

[116] F. P. Netzer and J. A. D. Mathew. Surfaces of rare-earth metals. *Reports on Progress in Physics*, 49:621–681, 1986.

[117] X. Queralt, C. Ferrater, F. Sanchez, R. Aguiar, J. Palau, and M. Varela. Erbium oxide thin films on Si(100) obtained by laser ablation and electron beam evaporation. *Applied Surface Science*, 86:95–98, 1995.

[118] A. A. Dakhel. DC conduction properties of oxidised erbium films deposited on Si(100) substrates. *Journal of Alloys and Compounds*, 396:74–78, 2005.

[119] P. Wetzel, L. Haderbache, C. Pirri, J. C. Peruchetti, D. Bolmont, and G. Gewinner. Room-temperature growth of Er films on Si(111): a photoelectron spectroscopy investigation. *Physical Review B*, 43:6620–6626, 1991.

[120] D. B. B. Lollman, T. A. Nguyen Tan, and J.-Y. Veuillen. A photoemission study of the interdiffusion of Si in Er films deposited on Si(111)(7×7) at room temperature. *Surface Science*, 269/270: 959–963, 1992.

[121] L. J. Chen, W. Lur, J. F. Chen, T. L. Lee, and J. M. Liang. Silicide formation by rapid thermal processing. In *Materials Research Society Symposium Proceedings*, volume 342, pages 99–110, 1994.

[122] P. Osiceanu. An XPS study on ion beam induced oxidation of titanium silicide. *Applied Surface Science*, 253:381–384, 2006.

[123] C. G. H. Walker, S. A. Morton, N. M. D. Brown, and J. A. D. Mathew. High-resolution Al Kα and high-photon energy Cr Kβ-excited x-ray photoelectron spectroscopy of titanium nitride. *Journal of Electron Spectroscopy and Related Phenomena*, 95:211–223, 1998.

[124] V. V. Atuchin, V. G. Kesler, N. V. Pervukhina, and Z. Zhang. Ti 2p and O 1s core levels and chemical bonding in titanium-bearing oxides. *Journal of Electron Spectroscopy and Related Phenomena*, 152:18–24, 2006.

[125] S. Kennou, S. Ladas, M. G. Grimaldi, T. A. Nguyen Tan, and J. Y. Veuillen. Oxidation of thin erbium and erbium silicide overlayers in contact with silicon oxide films thermally grown on silicon. *Applied Surface Science*, 102:142–146, 1996.

[126] S. Vandré, T. Kalka, C. Preinesberger, and M. Dähne-Prietsch. Flatband conditions observed for lanthanide-silicide monolayers on n-type Si(111). *Physical Review Letters*, 82:1927–1930, 1999.

[127] Shubha Gokhale, Shailaja Mahamuni, S. V. Deshmukh, V. J. Rao, A. S. Nigavekar, and S. K. Kulkarni. Photoemission and x-ray diffraction study of the Er/Si(111) interface. *Surface Science*, 237: 127–134, 1990.

[128] N. Guerfi, T. A. Nguyen Tan, J.-Y. Veuillen, and D. B. Lollman. Oxidation of thin $ErSi_{1.7}$ overlayers on Si(111). *Applied Surface Science*, 56/58:501–506, 1992.

[129] Y. Uwamino, Y. Ishizuka, and H. Yamatera. X-ray photoelectron spectroscopy of rare-earth compounds. *Journal of Electron Spectroscopy and Related Phenomena*, 34:67–68, 1984.

[130] G. T. K. Swami, F. E. Stageberg, and A. M. Goldman. XPS characterization of erbium sesquioxide and erbium hydroxide. *Journal of Vacuum Science and Technology A*, 2:767–770, 1984.

[131] C. D. Wagner, W. M. Riggs, L. E. Davis, and J. F. Moulder. *Handbook of x-ray photoelectron spectroscopy.* Perkin-Elmer Corporation, 1979.

[132] G. Larrieu, E. Dubois, X. Wallart, and X. Baie. Formation of platinum-based silicide contacts: Kinetics, stoichiometry and current drive capabilities. *Journal of Applied Physics*, 94:7801–7810, 2003.

[133] B. Demri, M. Hage-Ali, M. Moritz, J. L. Kahn, and D. Muster. X-ray photoemission study of the calcium/titanium dioxide interface. *Applied Surface Science*, 108:245–249, 1997.

[134] P. R. Moses, L. M. Wier, J. C. Lennox, H. O. Finklea, J. R. Lenhard, and R. W. Murray. X-ray photoelectron spectroscopy of alkylaminesilanes bound to metal oxide electrodes. *Analytical Chemistry*, 50:576–585, 1978.

[135] T. Ogama. A new method to detect energy-band bending using x-ray photoemission spectroscopy. *Journal of Applied Physics*, 64: 753–757, 1988.

[136] M. Anpo, H. Nakaya, S. Kodama, Y. Kubokawa, K. Domen, and T. Onishi. Photocatalysis over binary metal oxides. Enhancement of the photocatalytic activity of titanium dioxide in titanium-silicon oxides. *Journal of Physical Chemistry*, 90:1633–1636, 1986.

[137] S. Badrinarayanan, S. Sinha, and A. B. Mandale. XPS studies of nitrogen ion implanted zirconium and titanium. *Journal of Electron Spectroscopy and Related Phenomena*, 49:303–309, 1989.

[138] D. Gonbeau, C. Guimon, G. Pfister-Guillouzo, A. Levasseur, G. Meunier, and R. Dormoy. XPS study of thin films of titanium oxysulfides. *Surface Science*, 254:81–89, 1991.

[139] J. Y. Veuillen, T. A. Nguyen Tan, D. B. B. Lollman, N. Guerfi, and R. Cinti. Electronic properties of epitaxial erbium silicide. *Surface Science*, 251/252:432–436, 1991.

[140] G. J. Campisi, A. J. Bevolo, and F. A. Schmidt. The Schottky barrier height and Auger studies of yttrium and yttrium silicide on silicon. *Journal of Applied Physics*, 52:6647–6670, 1981.

[141] David R. Lide, editor. *CRC handbook of chemistry and physics*. CRC Press, 79th edition edition, 1998.

[142] E. Kaxiras. Semiconductor-surface restoration by valence-mending adsorbates: Application to Si(100):S and Si(100):Se. *Physical Review B*, 43:6824–6827, 1991.

[143] J. P. Lacharme, N. Benazzi, and C. A. Sébenne. Compositional and electronic properties of Si(001)2×1 upon diatomic sulfur interaction. *Surface Science*, 433-435:415–419, 1999.

[144] M. Tao, D. Udeshi, N. Basit, E. Maldonado, and W. P. Kirk. Removal of dangling bonds and surface states on silicon (001) with a monolayer of selenium. *Applied Physics Letters*, 82:1559–1561, 2003.

[145] M. Tao, D. Udeshi, S. Agarwal, N. Basit, E. Maldonado, and W. P. Kirk. Low Schottky barriers on n-type silicon (001). *Applied Physics Letters*, 83:2593–2595, 2003.

[146] M. Tao, D. Udeshi, S. Agarwal, E. Maldonado, and W. P. Kirk. Negative Schottky barrier between titanium and n-type Si(001) for low-resistance ohmic contacts. *Solid-State Electronics*, 48:335–338, 2004.

[147] D. Udeshi, E. Maldonaldo, Y. Xu, M. Tao, and W. P. Kirk. Thermal stability of ohmic contacts between Ti and Se-passivated n-type Si(001). *Journal of Applied Physics*, 95:4219–4222, 2004.

[148] J. Osvald. Comment on "Negative Schottky barrier between titanium and n-type Si(001) for low-resistance ohmic contacts". *Solid-State Electronics*, 48:2347–2349, 2004.

[149] M. Tao and J. Zhu. Response to "Comment on Negative Schottky barrier between titanium and n-type Si(001) for low-resistance ohmic contacts" [Solid State Electron. 2004;48:335-8]. *Solid-State Electronics*, 48:2351–2352, 2004.

[150] B. E. Coss, W.-Y. Loh, R. M. Wallace, J. Kim, P. Majhi, and R. Jammy. Near band edge Schottky barrier height modulation using high-κ dielectric dipole tuning mechanism. *Applied Physics Letters*, 95:222105, 2009.

[151] R. L. Thornton. Schottky-barrier elevation by ion implantation and implant segregation. *Electronics Letters*, 17:485–486, 1981.

[152] A. Kinoshita, C. Tanaka, K. Uchida, and J. Koga. High-performance 50-nm-gate-length Schottky-source/drain MOSFETs with dopant-segregation junctions. In *Symposium on VLSI Technology*, pages 158–159, 2005.

[153] Q. T. Zhao, U. Breuer, E. Rije, St. Lenk, and S. Mantl. Tuning of NiSi/Si Schottky barrier heights by sulfur segregation during Ni silicidation. *Applied Physics Letters*, 86:062108, 2005.

[154] Q. T. Zhao, M. Zhang, J. Knoch, and S. Mantl. Tuning of Schottky barrier heights by silicidation induced impurity segregation. In *International Workshop on Junction Technology*, pages 147–152, 2006.

[155] Q. T. Zhao, U. Breuer, St. Lenk, and S. Mantl. Segregation of ion implanted sulfur in Si(100) after annealing and nickel silicidation. *Journal of Applied Physics*, 102:023522, 2007.

[156] K. Ikeda, Y. Yamashita, N. Sugiyama, N. Taoka, and S. Takagi. Modulation of NiGe/Ge Schottky barrier height by sulfur segregation during Ni germanidation. *Applied Physics Letters*, 88:152115, 2006.

[157] T. Yamauchi, A. Kinoshita, Y. Tsuchiya, J. Koga, and K. Kato. 1 nm NiSi/Si junction design based on first-principles calculation for ultimately low contact resistance. In *IEEE International Electron Device Meeting Technical Digest*, pages 1–4, 2006.

[158] T. Yamauchi, Y. Nishi, Y. Tsuchiya, A. Kinoshita J. Koga, and K. Kato. Novel doping technology for a 1 nm NiSi/Si junction with dipoles comforting Schottky (DCS) barrier. In *IEEE International Electron Device Meeting Technical Digest*, pages 963–966, 2007.

[159] H.-S. Wong, L. Chan, G. Samudra, and Y.-C. Yeo. Sub-0.1-eV effective Schottky-barrier height for NiSi on n-type Si (100) using antimony segregation. *IEEE Electron Device Letters*, 28:703–705, 2007.

[160] H.-S. Wong, L. Chan, G. Samudra, and Y.-C. Yeo. Effective Schottky barrier height reduction using sulfur or selenium at the NiSi/n-Si (100) interface for low resistance contacts. *IEEE Electron Device Letters*, 28:1102–1104, 2007.

[161] H.-S. Wong, L. Chan, G. Samudra, and Y.-C. Yeo. Low Schottky barrier height for silicides on n-type Si(100) by interfacial selenium segregation during silicidation. *Applied Physics Letters*, 93:072103, 2008.

[162] Z. Zhang, Z. Qiu, R. Liu, M. Östling, and S.-L. Zhang. Schottky-barrier height tuning by means of ion implantation into preformed silicide films followed by drive-in anneal. *IEEE Electron Device Letters*, 28:565–568, 2007.

[163] Z. Qiu, Z. Zhang, M. Östling, and S.-L. Zhang. A comparative study of two different schemes to dopant segregation at NiSi/Si and PtSi/Si interfaces for Schottky barrier height lowering. *IEEE Transactions on Electron Devices*, 55:396–403, 2008.

[164] C. Urban, Q.-T. Zhao, C. Sandow, M. Müller, U. Breuer, and S. Mantl. Schottky barrier height modulation by arsenic dopant segregation. In *International Conference on Ultimate Integration of Silicon*, pages 151–154, 2008.

[165] N. Breil, A. Halimaoui, E. Dubois, E. Lampin, G. Larrieu, L. Godet, G. Papasouliotis, and T. Skotnicki. Investigation of platinum silicide Schottky barrier height modulation using a dopant segregation approach. In *Materials Research Society Symposium Proceedings*, 2008.

[166] M. Sinha, E. F. Chor, and Y.-C. Yeo. Tuning the Schottky barrier height of nickel silicide on p-silicon by aluminum segregation. *Applied Physics Letters*, 92:222114, 2008.

[167] E. Alptekin, M. C. Ozturk, and V. Misra. Tuning of the platinum silicide Schottky barrier height on n-type silicon by sulfur segregation. *IEEE Electron Device Letters*, 30:331–333, 2009.

[168] R. Saiz-Pardo, R. Pérez, F. J. Garcia-Vidal, R. Whittle, and F. Flores. Systematic theoretical studies of the Schottky barrier control by passivating atomic intralayers. *Surface Science*, 426:26–37, 1999.

[169] W.-Y. Loh, H. Etienne, B. Coss, I. Ok, D. Turnbaugh, Y. Spiegel, F. Torregrosa, J. Banti, L. Roux, P.-Y. Hung, J. Oh, B. Sassman, K. Radar, P. Majhi, H.-H. Tseng, and R. Jammy. Effective modulation of Ni silicide Schottky barrier height using chlorine ion implantation and segregation. *IEEE Electron Device Letters*, 30: 1140–1142, 2009.

[170] E. Alptekin and M. C. Ozturk. Tuning of the nickel silicide Schottky barrier height on *p*-type silicon by indium implantation. *IEEE Electron Device Letters*, 30:1272–1274, 2009.

[171] S. F. Feste, J. Knoch, D. Buca, Q. T. Zhao, U. Breur, and S. Mantl. Formation of steep, low Schottky-barrier contacts by dopant segregation during nickel silicidation. *Journal of Applied Physics*, 107: 044510, 2010.

[172] S.-M. Koh, C.-M. Ng, P. Liu, Z.-Q. Mo, X. Wang, H. Zheng, Z.-Y. Zhao, N. Variam, T. Henry, Yu. Erokhin, G. S. Samudra, and Y.-C. Yeo. Schottky barrier height modulation with aluminum segregation and pulsed laser anneal: a route for contact resistance reduction. In *International Workshop on Junction Technology*, pages 1–4, 2010.

[173] J. F. Ziegler, M. D. Ziegler, and J. P. Biersack. The stopping and range of ions in matter. www.srim.org, 2008.

[174] A. Afzalian, N. D. Akhavan, C.-W. Lee, R. Yan, I. Ferain, P. Razavi, and J.-P. Colinge. A new F(ast)-CMS NEGF algorithm for efficient 3D simulations of switching characteristics enhancement in constricted tunnel barrier silicon nanowire MuGFETs. *Journal of Computational Electronics*, 8:287, 2009.

[175] J. Guo and M. S. Lundstrom. A computational study of thin-body, double-gate, Schottky barrier MOSFETs. *IEEE Transactions on Electron Devices*, 49:1897, 2002.

[176] A. Afzalian and D. Flandre. Breaching the kT/q limit with dopant segregated Schottky barrier resonant tunneling MOSFETs: a computationnal study. In *Proceedings of the European Solid-State Device Research Conference*, pages 1–4, 2010.

[177] J. Luo, Z.-J. Qiu, D. W. Zhang, P.-E. Hellström, M. Östling, and S.-L. Zhang. Effects of carbon on Schottky barrier heights of NiSi modified by dopant segregation. *IEEE Electron Device Letters*, 30: 608–610, 2009.